Wideband Direction of Arrival Estimation Techniques for a Class of Arbitrary Array Geometries

Mahmud Reza Dehghani

A Thesis
in
The Department
of
Electrical and Computer Engineering

Presented in Partial Fulfillment of the Requirements
for the Degree of Master of Applied Science (Electrical Engineering) at
Concordia University
Montreal, Quebec, Canada

March 2005

Library and
Archives Canada

Published Heritage
Branch

395 Wellington Street
Ottawa ON K1A 0N4
Canada

Bibliothèque et
Archives Canada

Direction du
Patrimoine de l'édition

395, rue Wellington
Ottawa ON K1A 0N4
Canada

Your file Votre référence
ISBN: 0-494-04365-2
Our file Notre référence
ISBN: 0-494-04365-2

NOTICE:
The author has granted a non-exclusive license allowing Library and Archives Canada to reproduce, publish, archive, preserve, conserve, communicate to the public by telecommunication or on the Internet, loan, distribute and sell theses worldwide, for commercial or non-commercial purposes, in microform, paper, electronic and/or any other formats.

The author retains copyright ownership and moral rights in this thesis. Neither the thesis nor substantial extracts from it may be printed or otherwise reproduced without the author's permission.

AVIS:
L'auteur a accordé une licence non exclusive permettant à la Bibliothèque et Archives Canada de reproduire, publier, archiver, sauvegarder, conserver, transmettre au public par télécommunication ou par l'Internet, prêter, distribuer et vendre des thèses partout dans le monde, à des fins commerciales ou autres, sur support microforme, papier, électronique et/ou autres formats.

L'auteur conserve la propriété du droit d'auteur et des droits moraux qui protège cette thèse. Ni la thèse ni des extraits substantiels de celle-ci ne doivent être imprimés ou autrement reproduits sans son autorisation.

In compliance with the Canadian Privacy Act some supporting forms may have been removed from this thesis.

While these forms may be included in the document page count, their removal does not represent any loss of content from the thesis.

Conformément à la loi canadienne sur la protection de la vie privée, quelques formulaires secondaires ont été enlevés de cette thèse.

Bien que ces formulaires aient inclus dans la pagination, il n'y aura aucun contenu manquant.

Canada

ABSTRACT

Wideband Direction of Arrival Estimation Techniques
for a Class of Arbitrary Array Geometries

Mahmud Reza Dehghani

Array signal processing is an established field with a number of available advanced powerful technologies for detecting and locating signals that arrive at a set of sensors in the presence of noise. The focus of this thesis is on development of direction of arrival (DOA) estimation techniques for both narrowband and wideband signal sources. For narrowband signals, the multiple signal classification (MUSIC) and weighted subspace fitting (WSF) algorithms based on subspace decomposition techniques are considered. These subspace methods are subsequently extended to the more challenging and interesting wideband signals by incorporating advanced algorithms such as incoherent signal subspace method (ISM) and coherent signal subspace method (CSM). Extension of the WSF algorithm to a framework based on CSM is also investigated.

To simplify the analysis and theoretical derivation of DOA estimation algorithms, the elements of a sensor array are often arranged in very regular structured geometries such as linear, circular and rectangular arrays. However, many useful array processing techniques that are developed in the literature for these geometries have not been extended to other important class of array geometries. This thesis focuses on extension and generalization of some commonly popular array processing techniques to specific array geometries designated as diagonal, triangular and squared cross shaped arrays. Performance comparisons for both narrowband and wideband techniques using these geometries are carried out. Based on extensive simulation results, it was determined that both node topology and the aperture length play key roles in the performance capabilities of the proposed techniques. Parameters and factors affecting the performance of both the narrowband and wideband techniques are investigated in some details. The performance capabilities of the MUSIC and WSF DOA estimators for the narrowband and wideband cases are evaluated and compared and it is observed that the WSF algorithm as compared to the MUSIC algorithm produced an excellent performance in most of the situations considered in this thesis.

Dedicated to my beloved wife Neda

ACKNOWLEDGEMENTS

I would like to express my sincere thanks and gratitude to Dr. Khashayar Khorasani, my thesis supervisor for his keen intellect, guidance, patience, professional advice and invaluable criticism throughout the study.

Sincere thanks are also extended to the other distinguished members of my thesis committee Dr. Rajamohan Ganesan, Dr. M. Reza Soleymani and Dr. Wei-Ping Zhu who contributed their time, knowledge and expertise. I express my gratefulness to Ms. Diane Moffat, Graduate Program Assistant of ECE Department, for all the administrative and secretarial help she extended to me. Also I wish to express my sincere thanks to Mr. Javad Mohammadpour Velni for the discussions he had with me relating to my work.

The members of my family have always been the strongest support in my life. My biggest debt of gratitude goes to my mother for her generous love which played an instrumental role in completing this project and my late father whose remembrance is always established. Special thanks should also be given to my brothers and sister, whose moral support always gave the confidence boost I needed. A heartfelt gratefulness is extended to my parents in law, brother and sisters in law whose long-distance enthusiasm was truly the wind beneath my wings. You always remain in my heart.

My deepest gratitude goes to my dear wife Neda for her help, encouragement and love, whenever I needed the most. Without her support this study would not have been successfully completed.

Finally, to all those whose names have unintentionally been left out, I wish to express my apologies and thanks. Above all, my thanks to the Almighty for making all these possible.

Table of Contents

List of Tables

List of Figures

Chapter 1

Introduction

1.1 Preamble

Array signal processing, a mature and specialized branch of signal processing, has a wide range of different applications such as radar, sonar, communications, geophysical and astrophysical exploration, biomedical signal processing and acoustics. However, the objectives are often the same i.e., the extraction of desired parameters from noisy observations. In other words, array signal processing focuses on extracting as much data as possible from a noisy environment using an array of sensors. These sensors are located at different spatial points in space to measure a propagating electromagnetic, acoustic, or seismic signal. In fact, an array of sensors is used for sampling the received signals in a space-time field by extracting their spatial and temporal characteristics. From a statistical point of view, a source can be categorized as having either a deterministic or a random signal. By a deterministic source we mean a known signal with some unknown parameters such as amplitude and delay. Some applications such as radar, active sonar, and communications where the transmitted signal is known to the receiver are the examples of deterministic sources. In many applications, the received signal is unknown or is affected through the transmission environment whose impulse response is either unknown or it changes with time and space so that the signal is random. In the case of random signals, the probability distribution function (PDF) provides the information used in extracting the desired parameters.

The goals of array signal processing may be categorized as field characterization, source tracking and signal enhancement. Source tracking is used to track the instantaneous positions of the soruces as they move in space. Signal enhancement involves improving the signal to noise ratio (SNR) at the array output beyond that of a single sensor. This can be performed by steering a beam towards the direction of source and/or inserting nulls in the beampattern in the direction of noise and interference. A conventional method of beam steering is to place delay elements at the output of the sensors and compute a weighted sum of the delayed outputs. With a proper selection of the delays, the signals arriving from a specific direction will appear with the same phase at the output of the delay elements. This is termed beamforming. If a source is located in the direction of the beam, the signal power at the array output can be increased by the square magnitude of the number of sensors. For an uncorrelated intersensor noise, the noise power at the beamformer output increases linearly with the number of sensors. Thus, the SNR can be increased by using a conventional beamformer. Estimation of the spatial properties of the sources (their velocity, range, azimuth, elevation, direction of movement and so on) is performed by field characterization. The first step to characterize the field is to determine the number of emitting sources. This step is called detection. The detection is followed by an estimation step which involves the estimation of the signal location in space. If the sources are located in the far field of the array sensors, the arriving wavefronts are planar and only azimuth and elevation need to be estimated. In addition, if it is assumed that the sources and the sensors are in the same plane then the direction of arrival (DOA) is the only spatial parameter of the sources to be obtained. In this thesis we will focus on estimation of DOA.

Array processing techniques can be used for both active and passive situations. In the case of active sensing such as in radar and sonar applications, a known signal of finite duration is generated and which is then propagated through the space and will be reflected by some target back to the source origin. The transmitted signal is usually modified in amplitude and phase by the target characteristics, which could be changing with time and the target position in space. In the passive case the signals received at the array are generated by the target, such as propeller or engine noise from submarines.

The original application of the array processing technology was primarily motivated by the military's need during World War II to locate enemy aircraft and ships using radar and sonar [1]. The techniques developed during that time were proved successfully. After the war, the success of array processing for radar and sonar led researchers to develop new and improved algorithms to study other applications such as medical imaging, image processing, and structural monitoring in seismology. We now consider some application areas in which the sensor arrays play an important role. These areas are [2]:

Radar

Radar is the area in which antenna arrays were first used. Most radar systems are active, and the antenna array is used for both transmission and reception of signals. Radar systems have application in both military and non-military situations. The ballistic missile detection problem is a military application while the air traffic control system is an example of non-military application.

Radio Astronomy

Antenna arrays are also used in the radio astronomy area where unlike radar systems, radio astronomy systems are passive and are used to detect celestial objects and estimate their characteristics. These systems usually employ arrays with very long baselines, extending from tens of kilometers to thousands of kilometers. Some of the aspects that should be considered in radio astronomy are the rotation of the earth during the signal processing period, different propagation characteristics at different array elements and synchronization over long distances.

Sonar

Sonar systems can be active or passive. The theory of active sonars has much in common with radars. The main difference between sonar and radar is that the sonar deals with acoustic energy into the water while the radar systems deals with electromagnetic energy in the atmosphere. Passive sonars listen to incoming acoustic energy from a target and use it to estimate the desired parameters. In addition, signals from a target can undergo reflection, creating multiple returns that are delayed and amplitude weighted replicas of the direct signal to the array. The main application in sonar systems is the detection and tracking of submarines.

Communications

Antenna arrays are widely used in communication systems. The communication signals may arrive at the receiving array as a single plane wave or multiple plane waves due to the multipath phenomenon. Moreover, the receiver noise, the interference and jamming signals may include communication signals. Several satellite systems use phased arrays in either the earth terminal or space segment in tracking and data relay satellite. Wireless cellular systems also use different types of multiple access techniques such as time division multiple access (TDMA), code division multiple access (CDMA) and global system for mobile communications (GSM).

Direction Finding

Sensor arrays are also used to solve the direction finding problem. The main goal here is to locate the source of the received signal. Direction of arrival (DOA) estimation is central to the sensor array processing problem, and much of the recent work in array processing has focused on methods for high resolution DOA estimation.

Seismology

There exists two main fields of seismology in which array processing have an important role. The first area of seismology is the detection and estimation of underground nuclear explosions. Indeed, in seismology, the layers of the earth are examined by sending sound signals into the earth. The sound is reflected from different layers that can be used to detect the underground nuclear explosions. The second field is the exploration seismology that is one of the most important applications of the array processing at the present time. The goal of the exploration seismology is to construct an image of the subsurface in which the structure and physical properties can be specified and described.

Tomography

Tomography is the cross-sectional imaging of objects from transmitted or reflected data. The object is first illuminated from a number of different directions and the data are then collected at a receiving array. The cross-sectional image may then be reconstructed from this data. Medical diagnosis and treatment are examples of successful applications of tomography.

The theory of array signal processing can be applied to both narrowband and wideband signals. The signal is said to be narrowband if the ratio of the highest frequency to the lowest frequency is usually very close to unity. In other word, for narrowband signals the amplitude and phase of the source signal vary slowly relative to the propagation time across the array. Narrowband signals have a well-defined nominal wavelength, and time delay can be estimated by a simple phase shift. An array of antennas monitoring the air traffic around an airport is a good example of narrowband situation. Each airplane sends a narrowband signal that is received by the antenna array. Location of the airplanes can then be estimated by using narrowband array processing techniques. Another example of narrowband array processing may be found in communication systems. A moving transmitter in mobile communications emits narrowband signals. The receiver consists of an array of antennas. The array receives the original signal from the source and its reflections from the other surrounding objects. Once the location of the source is estimated, the antenna array can steer a beam towards the direction of the source to reduce the effects of the reflected signals.

On the other hand, for wideband signals the frequency bandwidth is relatively large compared to the center frequency. For instance, the movement of cars, trucks, wheeled vehicles and personnel can generate wideband signals since the ratio of highest to lowest frequency is relatively quite large. For wideband signals, there is no specific characteristic wavelength and the time delays must be obtained by utilizing Fourier transform or by interpolation of the signals. An example of wideband array processing is passive sonar systems. A passive sonar may be composed of a number of hydrophones that listen to the underwater sound. A ship is located within the detection range of the passive sonar through the sound of the propeller caused by the ship. The propeller sound in this case is a wideband source.

An important issue in array processing problem is the array geometry, i.e., the configuration and the physical locations of the sensors. In fact, the total length of the array and the array spacing determine how the array geometry affects the signal processing problem. Uniform linear arrays, uniform circular arrays, rectangular arrays and triangular arrays are among the most common array geometries. In general, the spatial arrangement of the array sensors is arbitrary and the methods that are proposed in this thesis will be applicable to general array geometries. An extension of array processing techniques to the cross shaped array geometry will be considered in this thesis to demonstrate and illustrate the effects of using various types of array geometries.

1.2 Contributions

While the majority of research efforts in array signal processing have so far been devoted to uniform linear arrays (ULA), some attempts have also been made to other array geometries such as uniform circular arrays (UCA), uniform rectangular arrays and others. There are distinct advantages for these extension attempts. For example, the most obvious advantage of using the UCAs in comparison to ULAs is the UCAs ability to provide a full azimuth coverage, which is the result of their two-dimensional array structure. Furthermore, when called for, UCAs can provide a 180° coverage in elevation and while one UCA is able to provide the full azimuth coverage, at least three separate ULAs are required for the same task in which each ULA array covers a 120° sector. Therefore, the use of UCAs can lead to a reduction in hardware requirements. In comparison to other array geometries, ULAs also suffer from decreasing effective array aperture as the look direction changes while for other configurations with a reasonable number of sensors the effective array aperture is almost constant over any look direction in the azimuth. Despite these advantages, many useful array processing techniques that were derived for ULAs have not been extended to other array geometries. This thesis focuses on extension of a number of most commonly used array processing techniques to other array geometries such as cross shaped array configuration.

Toward these end, in this thesis we have investigated a number of specific array geometries and have made the following contributions:

- Extension of the narrowband ULA array processing techniques to diagonal, triangular and square cross shaped array geometries.
- Extension of the wideband ULA array processing techniques to diagonal, triangular and square cross shaped array geometries.
- Development of the weighted subspace fitting (WSF) algorithm as opposed to the multiple signal classification (MUSIC) method in wideband coherent signal subspace (CSM) technique for improving the performance of DOA estimation technique for wideband sources through reduction of the bias and the resolution SNR threshold.
- Comparative study of the performance capabilities of various geometries as applied to both narrowband and wideband DOA estimation problem.

1.3 Thesis Outline

The thesis is divided into six chapters. The present chapter is intended as a general introduction to the knowledge required to appreciate the subsequent chapters and to help put the work conducted here in perspective. In Chapter 2, the fundamentals of narrowband and wideband array signal processing techniques are provided. For narrowband signals, a number of methods such as multiple signal classification (MUSIC) [3] and weighted subspace fitting (WSF) [4] based on subspace decomposition techniques are considered. These subspace methods are subsequently extended to the more challenging wideband algorithms such as incoherent signal subspace method (ISM) [5] and coherent signal subspace method (CSM) [6]. Chapter 3 devotes to the introduction of an array geometry that consists of several nodes in which each node is a 5-element half-wavelength spaced cross shaped subarray. This array geometry can be configured in the form of linear, diagonal, triangular and square cross shaped arrays. Numerical examples and simulation results for both narrowband and wideband techniques using MUSIC and CSM algorithms using these array geometries are presented. In Chapter 4, the numerical examples and computer simulations using WSF and CSM algorithms for both narrowband and wideband signals are presented. Specifically the use of WSF algorithm in place of the MUSIC method in the CSM as a wideband technique is developed in this chapter. Performance comparison of narrowband and wideband techniques in terms of achievable and specifications and requirements using the above mentioned algorithms are addressed in Chapter 5. Finally, the conclusions and future research directions are presented in Chapter 6.

Chapter 2

Narrowband and Wideband Methods for DOA Estimation

2.1 Introduction

Statistical techniques for array signal processing have a variety of applications such as radar, radio astronomy, communications, sonar, seismology, and direction finding. Interestingly, in most applications the objectives of the techniques are the same, namely, the extraction of desired parameters from the noisy observations measured by the sensors. Array signal processing focuses on signals transmitted by the propagating waves. An array of sensors spatially distributed at known locations is used to measure a propagating acoustic, seismic, or electromagnetic wavefield. One of the main goals of array signal processing is to use sensors outputs to characterize the field by detecting the number of sources and finding their locations. In certain applications, array processing techniques are used to track the instantaneous locations of the sources as they move in space. Array signal processing can be applied to both narrowband and wideband signals. A signal is said to be narrowband if the amplitude and phase of the source signal vary slowly relative to the propagation time across the array. In other words, for narrowband signals the ratio of the highest frequency to the lowest frequency is usually very close to unity. Narrowband signals have a well-defined nominal wavelength, and time delay can be estimated by a simple phase shift. On the other hand, for wideband signals the frequency bandwidth is relatively large compared to the center frequency. For instance, the movement of a car, truck, wheeled vehicle and a personnel can generate wideband signals since the ratio of the highest to the lowest frequency is quite large. For wideband signals, there is no characteristic wavelength and time delays must be obtained by Fourier transform or by interpolation of the signal.

In this chapter, the fundamentals of narrowband and wideband array signal processing are provided. For narrowband signals, certain commonly utilized methods based on subspace decomposition are considered. The multiple signal classification (MUSIC) [3] and the weighted subspace fitting (WSF) [4] algorithms both originate from the concept of signal and noise subspaces that are defined by the eigenvectors of the sample covariance matrix. The MUSIC algorithm calculates a spatial pseudo spectrum from the noise subspace, and determines the DOAs from the dominant peaks in the spectrum. In spite of the MUSIC ability for resolving not closely spaced sources, this method fails to locate coherent sources. To overcome this drawback, WSF method has been developed which has capability of resolving too closely spaced sources in the presence of coherent signals.

These subspace methods can also be extended to the more challenging wideband signals. In the so-called incoherent signal subspace method (ISM) [5], wideband signals are decomposed into a set of non-overlapping narrowband components, and then narrowband algorithms are applied to estimate the DOAs. The corresponding initial results are then averaged to yield the final DOA solution. The ISM algorithm cannot effectively process coherent signals, and it is difficult to synthesize wideband signals at low SNRs. An alternative to the ISM approach is the coherent signal subspace method (CSM) [6], where the covariance matrices are estimated at several frequency bins, aligned by proper transformation matrices, and finally averaged. In other words, CSM maps the signal subspaces of the narrowband components of the wideband signals onto a single signal subspace by focusing and then estimating the subspace spectrum at the focusing frequency. Compared to the ISM scheme, CSM algorithm significantly extends the detection and resolution thresholds, and also improves the bias and accuracy performance at low SNRs and is further able to cope with coherent sources in multipath scenarios [6]. An alternative focusing approach has also been developed in [7] and [8], but it suffers from the asymptotic bias of the peaks in the spatial spectrum. This bias increases with the bandwidth of the sources and the deviation of the focusing points from the true DOAs.

The organization of the present chapter is as follows. Section 2.2 introduces the narrowband techniques for DOA estimation. In section 2.2.1, the narrowband data model is presented followed by a brief exposition of the different array geometries and the introduction to the array manifold. Definitions for non-coherent, partially coherent and coherent sources are also included in this section. Section 2.2.2 introduces the subspace decomposition based methods for DOA estimation followed by description for the signal and noise subspaces. Section 2.2.3 presents the derivation of the MUSIC algorithm. In the next three subsections (2.2.4, 2.2.5 and 2.2.6), the WSF estimator is derived followed by brief exposition of associated optimization techniques and implementation issues of this algorithm.

Section 2.3 is devoted to the introduction to the wideband techniques for DOA estimation. Data model for wideband signals are derived in section 2.3.1. Section 3.4 will consider the coherent signal subspace method. The derivation for the diagonal focusing matrices and unitary focusing matrices are also addressed in this section. Finally, in section 2.3.3, the selection of the optimum focusing frequency for the CSM scheme will be considered.

2.2 DOA Estimation Techniques for Narrowband Signals

In the field of array signal processing, a variety of techniques are available for solving the detection and estimation problems for narrowband signals. Detection is a terminology used to characterize the procedure that determines the number of signals arriving at the array. Estimation is the process of estimating and determining the spatial parameters of the signals such as their DOAs (Direction of Arrivals). Methods that are used for detection and estimation may be categorized as beamforming and subspace decomposition techniques. The beamforming techniques have an easier implementation and are widely used in practice. The resolution of these methods is lower than the subspace decomposition methods. Classical beamforming techniques were the first attempts to localize signal sources using antenna arrays. By forming a weighted sum of the sensor outputs, signals from certain directions are coherently added while the noise and signals from the other directions are incoherently added . Beamforming techniques have been extensively studied in many books and literature, see for example [9]-[14].

In the presence of multiple closely spaced sources beamforming techniques cannot provide consistent parameter estimates because of the spectral leakage from the closely sources. The accuracy of the estimates is not constrained by the amount of data, but rather by the array geometry and sensor responses, which limit the resolution capabilities of these methods. Subspace decomposition based methods for estimating multiple not closely spaced sources are known from the literature that can be used to overcome the poor resolving power of the classical beamformer. Most of the subspace decomposition based methods decompose the observed covariance matrix into two orthogonal subspaces, commonly referred to as the signal and noise subspaces, and subsequently estimate the DOAs from one of these subspaces. These methods are known to have high resolution capabilities and generally are to yield accurate estimates.

One of the popular subspace decomposition techniques is the multiple signal classification (MUSIC) algorithm [3]. MUSIC was the first algorithm that showed the advantages of using a subspace approach. This algorithm calculates a spatial pseudo spectrum from the noise subspace, and determines the DOAs from the dominant peaks in the spectrum. The performance improvement of the MUSIC algorithm when compared to the classical beamformer is highly significant. Estimates of arbitrary accuracy can be achieved using this method if the size of data are sufficiently large and/or the SNR is adequately high, and the data model is sufficiently accurate. Therefore, MUSIC scheme can lead to statistically consistent estimates contrary to the classical beamformers. In spite of MUSIC's ability to resolve sources, this method fails to produce peaks associated with true DOAs subject to small samples and at low SNRs, specially, in the presence of closely spaced sources and coherent sources.

In the case of coherent sources, the orthogonal property of signal and noise subspaces is violated and the MUSIC algorithm fails to provide consistent estimates [15]. For these reasons, parametric subspace decomposition methods have been developed for their relatively excellent performance results yielding consistent estimates for coherent sources under certain conditions. An optimal parametric subspace based technique known as weighted subspace fitting (WSF) [4] is considered and analyzed in some details subsequently. As shown in the following sections the WSF algorithm has generally excellent performance capabilities in the presence of coherent sources.

2.2.1 Narrowband Data Model

In the general direction of arrival (DOA) estimation problem, the array under consideration is taken to have m identical sensors located at the coordinates

$$[x_l \quad y_l \quad z_l] \quad \text{for} \quad 1 \leq l \leq m \tag{2.2.1}$$

in a 3-dimensional space in which no restrictions are placed on the sensor geometry. However, throughout this thesis we will assume that the incident wavefield arises from a distant source, so that the incident signals have planar wave fronts. It is further assumed that the transmission of this so called far field wave is conducted in the x-y plane and also the array of sensors are in the same plane as the sources. Finally it is assumed that the noise samples are uncorrelated with the signals. These assumptions are arguably not restrictive and are made to simplify the formulation. The results that are derived bellow can easily be extended to other cases.

The incident wavefields induce signals on the sensors that are denoted by $\mathrm{x}_1(t)$, $\mathrm{x}_2(t)$, ..., $\mathrm{x}_m(t)$. The relationship among members of this signal set is found to provide the basis for solving the DOA estimation problem. These signals can be represented by the $m \times 1$ array output vector

$$\tilde{\mathrm{x}}(t) = [\mathrm{x}_1(t) \;\; \mathrm{x}_2(t) \;\; \ldots \;\; \mathrm{x}_m(t)]^T \tag{2.2.2}$$

where T denotes the transpose of a vector. The output vector provides a spatial sample of the wave field environment and the knowledge of its time behavior is to be used in estimating the number of signals and DOA. To obtain the general mathematical model, we first analyze the case of a single incident wave field and then this model is generalized to the case of multiple wave fields. For a single incident wave field in the noise free case the sensor signals are time-shifted versions of one another. That is, we have

$$\tilde{\mathrm{x}}(t) = [\tilde{\mathrm{s}}_1(t - \tau_1(\theta_1)) \;\; \tilde{\mathrm{s}}_1(t - \tau_2(\theta_1)) \;\; \ldots \;\; \tilde{\mathrm{s}}_1(t - \tau_m(\theta_1))]^T \tag{2.2.3}$$

where $\tilde{\mathrm{s}}_1(t)$ is the source signal, θ_1 is the azimuth angle and τ_l is the time delay associated with the *lth* sensor signal. The time delay is the time required for the signal to travel from the source to the sensor. Therefore, it is equal to the distances between the source and *lth* sensor divided by the velocity of wave propagation (i.e. c).

For far field wave this time delay is defined by

$$\tau_l(\theta_1) = \frac{1}{c}(x_l \cos\theta_1 + y_l \sin\theta_1) \;\; \text{for} \;\; 1 \leq l \leq m. \tag{2.2.4}$$

In order to estimate the DOA it is a standard practice in the literature to convert the output signal to the base band. This base band signal is obtained by first multiplying the output vector by $e^{j\omega_c t}$ and then by low pass filtering it (ω_c is the center frequency). In addition, if the amplitude and phase of the source signal vary slowly relative to the propagation time across the array, then the signal is said to be narrowband. In other words, for narrowband signals, the time delay can be approximated by a pure phase delay of the reference signal, and this phase delay depends only on the spacing between the sensors, the angle of arrival of the plane wave, and the frequency of the propagating wave.

Thus for the narrowband signal case the approximation $\mathrm{s}_1(t - \tau_l(\theta_1)) \approx \mathrm{s}_1(t)e^{-j\omega_c\tau_l(\theta_1)}$ is an accurate representation and therefore the output vector may be given by

$$\mathbf{x}(t) = [\mathrm{s}_1(t)e^{-j\omega_c\tau_1(\theta_1)} \quad \dots \quad \mathrm{s}_1(t)e^{-j\omega_c\tau_m(\theta_1)}]^T \tag{2.2.5}$$

or equivalently

$$\mathbf{x}(t) = \mathrm{s}_1(t)\mathbf{a}(\theta_1, \omega_c) \tag{2.2.6}$$

where

$$\mathbf{a}(\theta_1, \omega_c) = [e^{-j\omega_c\tau_1(\theta_1)} \quad \dots \quad e^{-j\omega_c\tau_m(\theta_1)}]^T \tag{2.2.7}$$

is defined as the steering vector of an array and $\mathrm{s}_1(t)$ is the response of the low pass filter to the source signal $\tilde{\mathrm{s}}_1(t)$. The steering vector of an array is also called the frequency response of the array for a given DOA. In general, for an array of m sensors, the steering vector is a column vector with m components represented by $\mathbf{a}(\theta, \omega)$, where θ and ω are the DOA and the processing frequency, respectively. The steering vector is a function of the array geometry. Figure 2.1 shows three different types of array geometries known as the uniform linear array (ULA), the uniform circular array (UCA) and the cross shaped array (CSA).

The methods that we will propose in this thesis are potentially applicable to general array geometry. However, the uniform linear array and the uniform circular array will be considered specifically in this chapter for studying different DOA estimation techniques. The extension of these methods to the cross shaped array geometry will be considered in the following chapter to demonstrate the advantages of utilizing this array geometry.

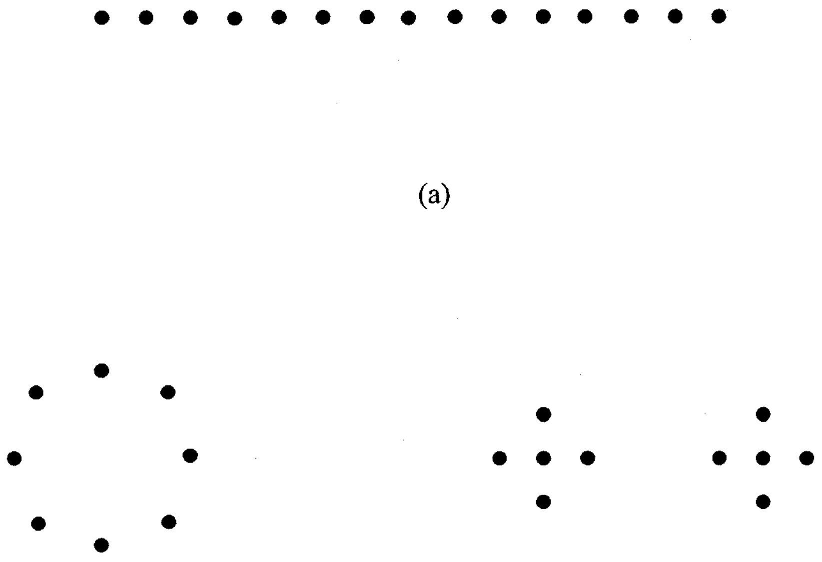

(a)

(b)

(c)

Figure 2.1: Three different types of array geometries (a) Uniform Linear Array, (b) Uniform Circular Array, and (c) Cross Shaped Array composed of two nodes

Figure 2.2 depicts a planar wave with DOA θ impinging on the ULA with m elements. If the phase reference point is taken as the origin of the coordinates, the received signal at point Δ is equal to

$$\mathrm{s}(t - \frac{\Delta \sin\theta}{c}) \tag{2.2.8}$$

therefore the steering vector of a uniform linear array with the phase reference taken at the first sensor is given by

$$\mathbf{a}(\theta) = [1 \quad e^{-j\omega_c \frac{\Delta \sin\theta}{c}} \quad \dots \quad e^{-j\omega_c \frac{(m-1)\Delta \sin\theta}{c}}]^T \tag{2.2.9}$$

where Δ is the distance between two consecutive sensors and c is the wave velocity. The steering vector of a uniform linear array can also be written as

$$\mathbf{a}(\theta) = [1 \quad e^{-j\frac{2\pi}{\lambda}\Delta \sin\theta} \quad \dots \quad e^{-j\frac{2\pi}{\lambda}(m-1)\Delta \sin\theta}]^T \tag{2.2.10}$$

where λ is the wavelength. Vectors with this special structure are commonly referred to

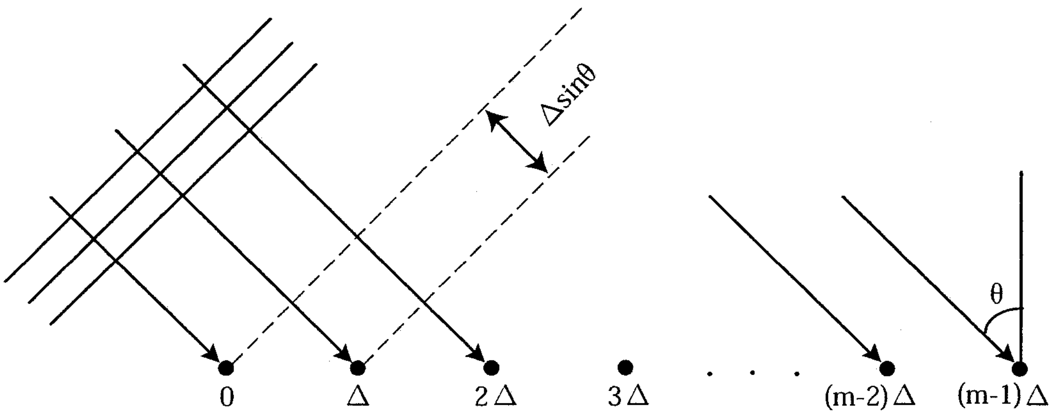

Figure 2.2: An ULA with m elements exposed to a planar wavefront with DOA θ

as the Vandermonde vectors.

We are now in a position to extend the model to the case of multiple incident wave fields. In this case, there are d wave fields incident on the array. The superposition principle indicates that the output vector would be a linear combination of the separate effects of the individual wave fields. Therefore, the data model in the presence of sensor noise, $\mathbf{n}(t)$, takes the form

$$\mathbf{x}(t) = \sum_{k=1}^{d} \mathrm{s}_k(t)\mathbf{a}(\theta_k) + \mathbf{n}(t) \tag{2.2.11}$$

where $\mathrm{s}_k(t)$ and θ_k are the source signal and the DOA of the kth incident wave field.

In the matrix form, the model is expressed as

$$\mathbf{x}(t) = \mathbf{A}(\theta)\mathbf{s}(t) + \mathbf{n}(t) \tag{2.2.12}$$

where $\mathbf{s}(t)$ is the $d \times 1$ source signal vector and $\mathbf{A}(\theta)$ is the $m \times d$ steering matrix whose columns are the steering vectors associated with the multiple incident sources, i.e.

$$\mathbf{A}(\theta) = [\mathbf{a}(\theta_1) \;\; \mathbf{a}(\theta_2) \;\; \ldots \;\; \mathbf{a}(\theta_d)]. \tag{2.2.13}$$

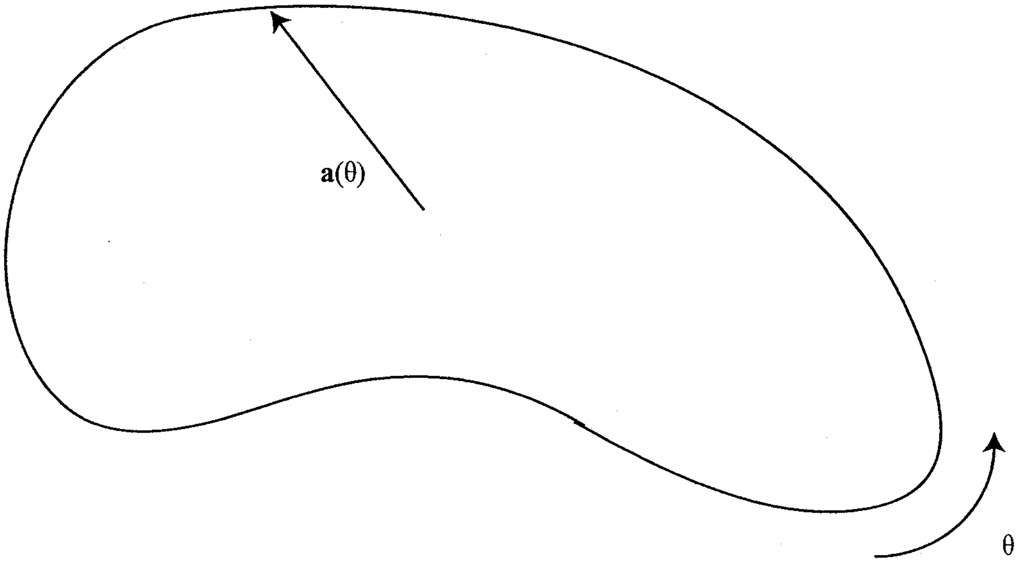

Figure 2.3: Array Manifold

It should be noted that the vector

$$\mathrm{a}(\theta_k) = [\mathrm{a}_1(\theta_k) \;\; \mathrm{a}_2(\theta_k) \;\; \ldots \;\; \mathrm{a}_m(\theta_k)]^T \text{ for } 1 \leq k \leq d \tag{2.2.14}$$

contains the sensor output to a single wave front from the direction θ_k. Thus the array manifold is defined as the set of all array steering vectors over the parameter range of interest i.e.

$$\mathcal{A} = \{\mathrm{a}(\theta_k) \mid \theta_k \in \Theta\} \tag{2.2.15}$$

In other words, as shown in Fig.2.3, the steering vector traces a one-dimensional space as the angle θ_k varies over the parameter range of interest [16].

Covariance Matrix

Let the array output $\mathbf{x}(t)$ be observed at N time instants, $\{t_1,\ t_2,\ \ldots,\ t_N\}$. Each vector observation is called a snapshot of the array output and the data matrix is the collection of the array snapshots

$$\mathbf{X}_N = [\mathbf{x}(t_1) \;\; \mathbf{x}(t_2) \;\; \ldots \;\; \mathbf{x}(t_N)] = \mathbf{A}(\theta)\mathbf{S}_N + \mathbf{N}_N \tag{2.2.16}$$

where the matrices $\mathbf{S}_N$ and $\mathbf{N}_N$ are defined analogously to $\mathbf{X}_N$. In order to detect the number of sources and estimate the associated DOAs, it is convenient to use the second order statistics of the array output. The following assumptions regarding the statistical properties of the data are further imposed. The signal, $\mathbf{s}(t)$, and the noise, $\mathbf{n}(t)$ are independent, zero mean, complex, Gaussian random processes with second order moments

$$\mathbf{S} = E\{\mathbf{s}(t)\mathbf{s}^H(t)\} = \lim_{N\to\infty} \frac{1}{N} \sum_{t=1}^{N} \mathbf{s}(t)\mathbf{s}^H(t) \tag{2.2.17}$$

$$\mathbf{R}_n = E\{\mathbf{n}(t)\mathbf{n}^H(t)\} = \sigma^2 \mathbf{I} \tag{2.2.18}$$

$$E\{\mathbf{s}(t)\mathbf{s}^T(t)\} = 0 \tag{2.2.19}$$

$$E\{\mathbf{n}(t)\mathbf{n}^T(t)\} = 0 \tag{2.2.20}$$

where H denotes complex conjugate transpose, $\mathbf{S}$ is the $d \times d$ unknown source covariance matrix, $\mathbf{R}_n$ is the $m \times m$ noise covariance matrix and $\mathbf{I}$ is the $m \times m$ identity matrix.

If the source covariance matrix $\mathbf{S}$ is diagonal and nonsingular, the multiple sources are said to be non-coherent. On the other hand, if this matrix is non-diagonal but singular then a subset of the sources are said to be coherent. Similarly, a non-diagonal and nonsingular source covariance matrix indicates that the multiple sources are partially coherent [17]. As seen from (2.2.18) the noise is assumed to be temporally white i.e. it has a flat spectrum over the frequency band of interest. It is further assumed that the noise is independent from sensor to sensor, i.e., spatially white (generalization to non-white noise is done by pre-whitening [18]). The noise power is assumed to be identical in all sensors, and its value, σ^2, is unknown. If the spatial whiteness condition is not met, the covariance matrix of the noise must be known, e.g. from measurements with no signals present.

Under the above assumptions, the array output is complex Gaussian with zero mean and the covariance matrix, $\mathbf{R}$, takes the following form

$$\begin{aligned}\mathbf{R} &= E\{\mathbf{x}(t)\mathbf{x}^H(t)\} \\ &= \lim_{N\to\infty}\frac{1}{N}\sum_{t=1}^{N}\mathbf{x}(t)\mathbf{x}^H(t) \\ &= \mathbf{A}(\theta)\mathbf{S}\mathbf{A}^H(\theta)+\sigma^2\mathbf{I} \qquad (2.2.21)\end{aligned}$$

It is assumed that the array manifold is known and any d steering vectors, $\mathbf{a}(\theta_k)$ for $k = 1, 2, \ldots, d$ with distinct θ_ks, are linearly independent, i.e. for any collection of d distinct $\theta_k \in \Theta$, the matrix $[\mathbf{a}(\theta_1)\ \ \mathbf{a}(\theta_2)\ \ \ldots\ \ \mathbf{a}(\theta_d)]$ has full rank. It is further assumed that the manifold vectors are continuously differentiable with respect to the parameters such as DOA θ. An array satisfying these assumptions is said to be unambiguous. Due to the Vandermonde structure of $\mathbf{a}(\theta)$ for ULA , it is clear that the ULA is unambiguous if the parameter set is $\Theta = (-\frac{\pi}{2}, \frac{\pi}{2})$.

With the above stated preliminaries, the sensor array problem is defined as the detection of the number of sources d and the associated DOAs estimation using the observations $\mathbf{X}_N$ and a model for the steering matrix $\mathbf{A}(\theta)$. In this thesis, multiple signal classification (MUSIC) [3] and weighted subspace fitting (WSF) [4] algorithms are used to estimate the DOAs where it is assumed that the number of sources is known.

2.2.2 Subspace Decomposition Based Methods

The subspace decomposition methods rely on the decomposition of the observed covariance matrix into two orthogonal spaces, referred to as the signal and noise subspaces. If the sources are non-coherent, then the source covariance matrix, $\mathbf{S}$, has full rank. However, in many applications signal sources may be coherent which results in rank deficiency of $\mathbf{S}$. Assume the source covariance matrix has rank d'. Therefore the covariance matrix $\mathbf{R}$ takes the form

$$\mathbf{R} = \mathbf{A}(\theta)\mathbf{S}\mathbf{A}^H(\theta) + \sigma^2\mathbf{I} \tag{2.2.22}$$

it is possible to show that any vector in the null space of the matrix $\mathbf{ASA}^H$ is an eigenvector of $\mathbf{R}$ corresponding to eigenvalue σ^2 [3],[19]. As mentioned before, to allow for unique DOA, the steering matrix, $\mathbf{A}(\theta)$, is assumed to be full rank. Thus, the matrix $\mathbf{ASA}^H$ has rank d' and σ^2 is the smallest eigenvalue of $\mathbf{R}$ with multiplicity $m - d'$.

Let $\lambda_1, \lambda_2, \ldots, \lambda_m$ be the eigenvalues of covariance matrix arranged in non-increasing order, and $\mathbf{e}_1, \mathbf{e}_2, \ldots, \mathbf{e}_m$ denote the associated eigenvectors. Then the spectral decomposition of the covariance matrix is given by

$$\mathbf{R} = \sum_{l=1}^{m} \lambda_l \mathbf{e}_l \mathbf{e}_l^H = \mathbf{E}_s\mathbf{\Lambda}_s\mathbf{E}_s^H + \mathbf{E}_n\mathbf{\Lambda}_n\mathbf{E}_n^H \tag{2.2.23}$$

where

$$\mathbf{\Lambda}_s = diag[\lambda_1, \lambda_2, \ldots, \lambda_{d'}] \tag{2.2.24}$$

$$\mathbf{\Lambda}_n = \sigma^2\mathbf{I} \tag{2.2.25}$$

$$\mathbf{E}_s = [\mathbf{e}_1 \;\; \mathbf{e}_2 \;\; \ldots \;\; \mathbf{e}_{d'}] \tag{2.2.26}$$

$$\mathbf{E}_n = [\mathbf{e}_{d'+1} \;\; \mathbf{e}_{d'+2} \;\; \ldots \;\; \mathbf{e}_m] \tag{2.2.27}$$

where $\mathbf{\Lambda}_s$ is a diagonal matrix that contains the largest eigenvalues of the covariance matrix and these so called signal eigenvalues are supposed to be distinct. The signal subspace is defined as the subspace spanned by the eigenvectors of the covariance matrix associated with these dominant eigenvalues. Thus, the range space of $\mathbf{E}_s$ is the signal subspace and the range space of $\mathbf{E}_n$, the orthogonal complement of the signal subspace, is defined as the noise subspace.

The orthogonality property implies that the d'-dimensional range space of $\mathbf{E}_s$ is contained in the d-dimensional range space of $\mathbf{A}(\theta)$ and if the source covariance matrix is full rank (non-coherent sources), then these subspaces are equal because in this case they have the same dimension i.e. $d' = d$. Therefore, based on these facts, the contribution of the signal to the covariance matrix is merely along the signal eigenvalues. A number of algorithms are available in the literature for solving the DOA estimation problem. However, for our purposes in this thesis, we only consider the multiple signal classification (MUSIC) [3] and the weighted subspace fitting (WSF) [4] which are the two most popular approaches.

2.2.3 Multiple Signal Classification (MUSIC) Method

One of the most popular techniques of the subspace decomposition is the multiple signal classification (MUSIC) [3] method. MUSIC was the first algorithm that showed the advantages of using a subspace based approach. The basic idea behind this algorithm is that the span of the steering matrix is the same as the span of the signal eigenvectors, $\mathbf{E}_s$, of the covariance matrix. In other words, by finding the intersections between array manifold and signal subspace, one may estimate the DOAs. In practice, the covariance matrix $\mathbf{R}$ is unknown and only the sample covariance matrix, $\hat{\mathbf{R}}$, can be estimated by averaging N independent snapshots, i.e.,

$$\hat{\mathbf{R}} = \frac{1}{N}\sum_{t=1}^{N}\mathbf{x}(t)\mathbf{x}^H(t) = \frac{1}{N}\mathbf{X}_N\mathbf{X}_N^H \tag{2.2.28}$$

and then $\hat{\mathbf{R}}$, is decomposed to separate estimated signal and noise subspaces according to

$$\hat{\mathbf{R}} = \hat{\mathbf{E}}_s\hat{\mathbf{\Lambda}}_s\hat{\mathbf{E}}_s^H + \hat{\mathbf{E}}_n\hat{\mathbf{\Lambda}}_n\hat{\mathbf{E}}_n^H \tag{2.2.29}$$

where $\hat{\mathbf{E}}_s$, is the estimated signal subspace matrix and $\hat{\mathbf{E}}_n$, is the estimated noise subspace matrix.

As mentioned before, it can be shown that the noise eigenvectors are orthogonal to the space spanned by the columns of the steering matrix [19]. So we have

$$\hat{\mathbf{E}}_n^H\mathbf{a}(\theta) = \mathbf{0}\ , \qquad \theta \in \{\theta_1, \theta_2, \ldots, \theta_d\} \tag{2.2.30}$$

Thus, if the Euclidean distance from $\mathbf{a}(\theta)$ to $\hat{\mathbf{E}}_n$ is

$$D^2 = \mathbf{a}(\theta)^H\hat{\mathbf{E}}_n\hat{\mathbf{E}}_n^H\mathbf{a}(\theta) \tag{2.2.31}$$

then, estimation of DOAs can be determined by finding peaks in $\frac{1}{D^2}$. In other words, the MUSIC algorithm uses the fact that the reciprocal of the distance between the estimated noise subspace and the true noise subspace results in sharp peaks in the vicinity of the DOAs. Using this property, the MUSIC spatial spectrum is given by

$$P_M(\theta) = \frac{1}{\mathbf{a}(\theta)^H\hat{\mathbf{E}}_n\hat{\mathbf{E}}_n^H\mathbf{a}(\theta)}. \tag{2.2.32}$$

The expression (2.2.32) shows that the MUSIC algorithm is asymptotically unbiased since $\hat{\mathbf{R}}$ is measured asymptotically. This results in asymptotic measurement of $\hat{\mathbf{E}}_n$. It should be noted that $\mathbf{a}(\theta)$ is independent of the observed data. In spite of the fact that MUSIC is a statistically consistent estimator in the presence of non-coherent sources, one generally requires a sufficiently large data set having high SNR. Furthermore, it has the ability to resolve not closely spaced sources, but as it will be shown in the numerical examples subsequently this method yields large estimation errors in the case of closely spaced sources, low SNR and coherent sources.

If the sources are coherent, the orthogonal property is generally invalid and the MUSIC algorithm is inefficient. To overcome this inefficiency, in the next section, the parametric subspace decomposition methods will be introduced. The so called subspace fitting methods (SSF) [16] have been developed for their relatively excellent performance capabilities to yield consistent estimates for the coherent sources. By choosing a proper weighting matrix an optimal parametric subspace based technique known as the weighted subspace fitting (WSF) methods [4] will be discussed in some more details.

2.2.4 Weighted Subspace Fitting (WSF) Method

As discussed in the previous section, the MUSIC algorithm generally suffers from a large finite sample bias in the presence of coherent sources resulting in resolution problems. This drawback is inherent due to the one-dimensional search of the parameter space. In order to reduce the sensitivity of the MUSIC estimator to cope with coherent sources, a few techniques such as multi-dimensional MUSIC (MD-MUSIC) [3], [20] and spatial smoothing [21] have been developed. The MD-MUSIC algorithm, however, leads one to a computationally expensive search process and the spatial smoothing method cannot cope with general array geometries. Thus these methods have not received much attention due to computational complexity and restrictions in the array structure.

This section attempts to introduce the weighted subspace method that has the capability to resolve the too closely spaced sources in the presence of coherent signals for general array geometries. This method fits the subspace spanned by $\mathbf{A}(\theta)$ to the measurements $\mathbf{X}_N$ in a least squares sense. In other words, the subspace fitting estimate selects $\mathbf{A}$ so that this subspace is as close to the data as possible. In the following the subspace fitting formulation of the sensor array problem is analyzed and the weighted subspace fitting technique is discussed.

It was shown earlier that the eigen-decomposition of the covariance matrix can be expressed as

$$\mathbf{R} = \mathbf{A}(\theta)\mathbf{S}\mathbf{A}^H(\theta) + \sigma^2\mathbf{I} = \mathbf{E}_s\mathbf{\Lambda}_s\mathbf{E}_s^H + \mathbf{E}_n\mathbf{\Lambda}_n\mathbf{E}_n^H \tag{2.2.33}$$

It is clear that $\mathbf{E}_n$ is orthogonal to $\mathbf{ASA}^H$, which implies that the matrices $\mathbf{A}$ and $\mathbf{E}_s$ span the same range space whenever $\mathbf{S}$ is full rank. In the case of coherent sources, $\mathbf{S}$ has rank deficiency and so the matrix $\mathbf{E}_s$ spans the d'-dimensional (with d' as the rank of $\mathbf{S}$) subspace of $\mathbf{A}(\theta)$. It can be shown that by substituting $\mathbf{I} = \mathbf{E}_s\mathbf{E}_s^H + \mathbf{E}_n\mathbf{E}_n^H$ in (2.2.33) we have

$$\mathbf{ASA}^H + \sigma^2\mathbf{E}_s\mathbf{E}_s^H = \mathbf{E}_s\mathbf{\Lambda}_s\mathbf{E}_s^H \tag{2.2.34}$$

multiplying the two sides by $\mathbf{E}_s$ yields

$$\mathbf{E}_s = \mathbf{A}(\theta)\mathbf{T} \tag{2.2.35}$$

where, $\mathbf{T}$ is the $d \times d'$ matrix of full rank and takes the form

$$\mathbf{T} = \mathbf{SA}^H\mathbf{E}_s(\mathbf{\Lambda}_s - \sigma^2\mathbf{I})^{-1} \tag{2.2.36}$$

In practice an estimate of $\mathbf{E}_s$ is available and there may be no exact solution for θ

such that

$$\hat{\mathbf{E}}_s = \mathbf{A}(\theta)\mathbf{T} \tag{2.2.37}$$

Therefore, an estimation criterion is utilized to find the best least squares fit of the two subspaces, or equivalently, minimizing the distance between $\hat{\mathbf{E}}_s$ and $\mathbf{A}(\theta)\mathbf{T}$. This may be achieved by solving the following optimization problem, which is linear in $\mathbf{T}$ and nonlinear in θ

$$[\hat{\theta}, \hat{\mathbf{T}}] = \arg\min_{\theta,\mathbf{T}} \left\| \hat{\mathbf{E}}_s - \mathbf{A}(\theta)\mathbf{T} \right\|_F^2 \tag{2.2.38}$$

where $\|.\|_F$ is the Frobenius norm and arg min denotes the minimizing the argument of the proceeding expression. The above equation can be used to define the class of subspace fitting methods (SSF) [16]. It is possible to show that the subspace fitting problem is separable in $\mathbf{A}$ and $\mathbf{T}$ [33], therefore, by solving for $\mathbf{T}$ i.e., $\hat{\mathbf{T}} = \mathbf{A}^{\dagger}\hat{\mathbf{E}}_s$, and substituting back in (2.2.38), $\hat{\theta}$ can be written as

$$\hat{\theta} = \arg\min_{\theta} V(\theta) \tag{2.2.39}$$

where the cost function $V(\theta)$ is defined as

$$\begin{aligned} V(\theta) &= \left\| \hat{\mathbf{E}}_s - \mathbf{A}(\theta)\mathbf{A}^{\dagger}(\theta)\hat{\mathbf{E}}_s \right\|_F^2 \\ &= \left\| \{\mathbf{I} - \mathbf{P}_{\mathbf{A}}(\theta)\}\hat{\mathbf{E}}_s \right\|_F^2 \\ &= tr\{\mathbf{P}_{\mathbf{A}}^{\perp}(\theta)\hat{\mathbf{E}}_s\hat{\mathbf{E}}_s^H\} \end{aligned} \tag{2.2.40}$$

where $\mathbf{A}^{\dagger} = (\mathbf{A}^H\mathbf{A})^{-1}\mathbf{A}^H$ is the pseudo-inverse for $\mathbf{A}$ of full rank, $\mathbf{P}_{\mathbf{A}} = \mathbf{A}\mathbf{A}^{\dagger}$ denotes the projection matrix and $\mathbf{P}_{\mathbf{A}}^{\perp} = \mathbf{I} - \mathbf{P}_{\mathbf{A}}$.

To minimize the distance between $\hat{\mathbf{E}}_s$ and $\mathbf{AT}$, it is sufficient to introduce a weighting matrix for the signal subspace matrix that results in the so-called weighted subspace fitting (WSF) algorithm whenever the optimum weighting matrix that maximizes the accuracy is used [4]. Thus, multiplying the signal subspace matrix by a specific weighting matrix $\mathbf{W}$, the estimator $\hat{\theta}$ takes the form

$$\hat{\theta} = \arg\min_{\theta} V(\theta) = \arg\min_{\theta} tr\{\mathbf{P}_{\mathbf{A}}^{\perp}(\theta)\hat{\mathbf{E}}_s\mathbf{W}\hat{\mathbf{E}}_s^H\} \tag{2.2.41}$$

As shown in [16], the optimum weighting matrix that yields the lowest asymptotic estimation error variance is defined as

$$\mathbf{W} = (\hat{\mathbf{\Lambda}}_s - \hat{\sigma}^2\mathbf{I})^2\hat{\mathbf{\Lambda}}_s^{-1} \tag{2.2.42}$$

where $\hat{\sigma}^2$ is any consistent estimate of the noise variance, e.g., the average of the $m - d'$ smallest eigenvalues of the measured covariance matrix.

2.2.5 Evaluating the WSF Estimator

In order to compute the WSF estimator, the cost function $V(\theta)$ must be minimized as a multi-dimensional nonlinear optimization problem. In the array signal processing literature, many optimization techniques have been suggested e.g., the alternating projection method [22], global search techniques [23], [24], expected maximization methods [25], [26], iterative quadratic maximum likelihood [27], as well as different Newton type techniques [4], [20], [28]-[30]. In this section, the modified variable projection technique [31], [32] which is a modification of the Gauss-Newton technique [33] is considered.

As shown in the previous section, the cost function for the WSF method takes the form

$$V(\theta) = tr\{\mathbf{P}_{\mathbf{A}}^{\perp}(\theta)\hat{\mathbf{E}}_s\mathbf{W}\hat{\mathbf{E}}_s^H\} \tag{2.2.43}$$

where

$$\hat{\theta} = \arg\min_{\theta} V(\theta) \tag{2.2.44}$$

is to be calculated. For this purpose, the damped Newton technique [34], [35] which is an efficient optimization technique may be used. Specifically by choosing an initial estimate θ_0, this method iteratively computes the DOA estimate as

$$\theta_{k+1} = \theta_k - \mu_k \mathbf{H}^{-1} V' \tag{2.2.45}$$

where θ_k is the DOA estimate at iteration k, $\mathbf{H}$ denotes the Hessian matrix (matrix of second derivatives) of the cost function, V' is the gradient (vector of first derivatives) and μ_k is the step length. In order to converge to a local minimum, the step length should generally be chosen to be less than one so that the cost function can be decreased sufficiently. To obtain convergence to a global minimum, the algorithm must be initialized appropriately. For example, if the cost function, $V'(\theta)$, possesses several minima, the iterations must be initialized sufficiently close to the global minimum or a number of random initializations should be performed in order to prevent convergence to local solutions.

The Newton's method approximates the cost function locally around a stationary point by a quadratic function. The Hessian approximation method can be seen as a modification of the gradient direction, to take into account the curvature of the approximation. The Newton's method has some drawbacks when applied to the above problems. First, while the negative gradient is a descent direction for the cost function, the Newton's direction $(\mathbf{H}^{-1}V')$ can be guaranteed to be a descent direction only if $\mathbf{H}$ is positive definite. This may not be the case when one is located far from the minimum, where $V'(\theta)$ cannot, in general, be well approximated by a quadratic function. Hence, there may exists no value of μ_k that causes a decrease in the cost function. Second, the evaluation of the exact Hessian matrix for the WSF criteria is computationally cumbersome.

A standard technique for overcoming the above difficulties is to use a less complex approximation of the Hessian matrix, which is also guaranteed to be positive semi-definite. These techniques use the asymptotic (for large N) form of the Hessian matrices. This method is often referred to as the modified variable projection technique (MVP) [31], [32]. It is closely related to the Gauss-Newton technique for nonlinear least squares problems. The algorithm was applied to the array processing problem by Viberg et al. [4], and our discussion below follows closely that reference.

Introduce a vector $\mathbf{r}$ by stacking the columns of $\mathbf{P}_{\mathbf{A}}^{\perp}\mathbf{M}$,

$$\mathbf{r} = vec(\mathbf{P}_{\mathbf{A}}^{\perp}(\theta)\mathbf{M}) \tag{2.2.46}$$

where $\mathbf{M} = \hat{\mathbf{E}}_s\mathbf{W}^{\frac{1}{2}}$ represents the data. Using (2.2.46) in (2.2.43) gives

$$V(\theta) = |\mathbf{r}|^2 \tag{2.2.47}$$

the first derivative (i.e., gradient) of V with respect to θ_i is

$$\frac{\partial V}{\partial \theta_i} = 2\Re\{(\frac{\partial \mathbf{r}}{\partial \theta_i})^H\mathbf{r}\} = 2\Re\{\mathbf{r}_i^H\mathbf{r}\} \tag{2.2.48}$$

where $\Re$ denotes the real part and

$$\mathbf{r}_i \triangleq \frac{\partial \mathbf{r}}{\partial \theta_i} = \frac{\partial \mathbf{P}_{\mathbf{A}}^{\perp}(\theta)}{\partial \theta_i}\mathbf{M} \tag{2.2.49}$$

and the derivative of the projection matrix is [16],[33]:

$$\frac{\partial \mathbf{P}_{\mathbf{A}}^{\perp}}{\partial \theta_i} = -\frac{\partial \mathbf{P}_{\mathbf{A}}}{\partial \theta_i} = -\mathbf{P}_{\mathbf{A}}^{\perp}\mathbf{A}_i\mathbf{A}^{\dagger} - (\mathbf{P}_{\mathbf{A}}^{\perp}\mathbf{A}_i\mathbf{A}^{\dagger})^H \tag{2.2.50}$$

where

$$\mathbf{A}_i \triangleq \frac{\partial \mathbf{A}}{\partial \theta_i} \tag{2.2.51}$$

Using (2.2.50) in (2.2.48) gives

$$V'(\theta) = -2\Re\{diag(\mathbf{A}^{\dagger}\mathbf{M}\mathbf{M}^H\mathbf{P}_{\mathbf{A}}^{\perp}\mathbf{D})\} \tag{2.2.52}$$

where $diag(\mathbf{A})$ is a column vector formed from the diagonal elements of $\mathbf{A}$ and

$$\mathbf{D}(\theta) = \{\frac{\partial \mathbf{a}(\theta_1)}{\partial \theta_1}, \cdots, \frac{\partial \mathbf{a}(\theta_d)}{\partial \theta_d}\} \tag{2.2.53}$$

The next step is to derive the Hessian matrix. This is done by differentiating (2.2.48) with respect to θ_j, thus we have

$$\frac{\partial^2 V}{\partial \theta_i \partial \theta_j} = 2\Re\{\mathbf{r}_i^H \mathbf{r}_j + \mathbf{r}_{ij}^H \mathbf{r}\} \tag{2.2.54}$$

The Gaussian modification of the Newton's technique assumes that the so called residual, the term in (2.2.54), is small and approximates the Hessian matrix by

$$\mathbf{H} = 2\Re\{\mathbf{r}_i^H \mathbf{r}_j\} \tag{2.2.55}$$

Ignoring the second derivative guarantees that (2.2.45) is a descent method since $\mathbf{H}$ is positive semi-definite. The resulting Gauss-Newton based algorithm is the variable projection scheme of Golub and Pereyra [33]. Using (2.2.46) in (2.2.50) and noting that $\mathbf{P}_{\mathbf{A}}^{\perp}(\mathbf{A}^{\dagger})^H = \mathbf{A}^{\dagger}\mathbf{P}_{\mathbf{A}}^{\perp} = 0$, yields

$$\mathbf{r}_i^H \mathbf{r}_j = tr\{[(\mathbf{A}^{\dagger})^H \mathbf{A}_i^H \mathbf{P}_{\mathbf{A}}^{\perp} \mathbf{A}_j \mathbf{A}^{\dagger} + \mathbf{P}_{\mathbf{A}}^{\perp} \mathbf{A}_i \mathbf{A}^{\dagger} (\mathbf{A}^{\dagger})^H \mathbf{A}_j^H \mathbf{P}_{\mathbf{A}}^{\perp}] \mathbf{M}\mathbf{M}^H\} \tag{2.2.56}$$

Kaufman [31] modified the Gauss-Newton technique by ignoring the second term in (2.2.56) which leads to

$$\mathbf{H}_{ij} = 2\Re\{tr[(\mathbf{A}^{\dagger})^H \mathbf{A}_i^H \mathbf{P}_{\mathbf{A}}^{\perp} \mathbf{A}_j \mathbf{A}^{\dagger} \mathbf{M}\mathbf{M}^H]\} \tag{2.2.57}$$

and in the matrix notation form

$$\mathbf{H} = 2\Re\{(\mathbf{D}^H \mathbf{P}_{\mathbf{A}}^{\perp} \mathbf{D}) \odot (\mathbf{A}^{\dagger} \mathbf{M}\mathbf{M}^H (\mathbf{A}^{\dagger})^H)^T\} \tag{2.2.58}$$

where $\odot$ is the Hadamard product. Therefore, the algorithm may be specified according to (2.2.45), (2.2.52), and (2.2.58). In order to guarantee convergence to a local minimum, the step length, μ_k, should be chosen appropriately. As discussed before, for Newton's techniques this parameter should be selected to be less than unity and one should take $\mu_k = \mu^i$ as the smallest integer $i \geq 0$ that results in sufficient decrease in the cost function.

2.2.6 WSF Implementation and Practical Aspects

In this section, a detailed implementation of the modified variable projection (MVP) method [31], [32] for the WSF algorithm is provided. A number of problems exist as related to practical implementation of this method. For example, the array manifold must be accurately calibrated to obtain reliable estimates of the DOAs. Also, to obtain the gradient and the Hessian, the cost function must be at least twice differentiable with respect to θ. Moreover, the updates must be properly initialized in order to guarantee convergence to the global minimum.

Consequently, a suboptimal estimator such as MUSIC can be used to find an initial estimates of the DOAs. This algorithm can be applied to general array geometries, but as mentioned previously, MUSIC can not cope with coherent sources. A promising algorithm, that can be used to initialize the modified Gauss-Newton based technique is the alternating projection (AP) algorithm. The main idea of the AP algorithm, which was applied to the array processing problem by Ziskind and Wax [22], is to replace the multi-dimensional optimization problem by a sequence of one-dimensional optimization problems. The AP algorithm can be applied to the general array geometry case as well as to the coherent sources. Although, this algorithm converges globally to a local minimum, the convergence can be very slow if the Hessian matrix is ill-conditioned.

In order to implement the WSF estimator, an iteration of the MVP algorithm involves the evaluation of the current values of the cost function V, the gradient V', the approximate Hessian $\mathbf{H}$, and the Newton's direction (search direction) i.e. $\mathbf{s} = -\mathbf{H}^{-1}V'$. Each iteration in the algorithm requires the calculation of $\mathbf{P}_{\mathbf{A}}^{\perp}$ and $\mathbf{A}^{\dagger}$. This can be done by **QR** decomposition of **A** using Householder transformations [36]:

$$\mathbf{A} = \mathbf{QR} = [\mathbf{Q}_1 \quad \mathbf{Q}_2] \begin{bmatrix} \mathbf{R}_1 \\ 0 \end{bmatrix} \tag{2.2.59}$$

thus

$$\mathbf{A}^{\dagger} = \mathbf{R}_1^{-1}\mathbf{Q}_1^H \tag{2.2.60}$$

and

$$\mathbf{P}_{\mathbf{A}}^{\perp} = \mathbf{Q}_2\mathbf{Q}_2^H \tag{2.2.61}$$

Finally, the cost function V, the gradient V' and the approximate Hessian $\mathbf{H}$ take the form

$$V = tr\{\boldsymbol{\Psi}\boldsymbol{\Psi}^H\} \tag{2.2.62}$$

$$V' = -2\Re\{diag(\boldsymbol{\Gamma}\boldsymbol{\Psi}\boldsymbol{\Phi})\} \tag{2.2.63}$$

$$\mathbf{H} = 2\Re\{(\boldsymbol{\Phi}^H\boldsymbol{\Phi}) \odot (\boldsymbol{\Gamma}\boldsymbol{\Gamma}^H)^T\} \tag{2.2.64}$$

where the intermediate variables are defined as

$$\boldsymbol{\Phi} = \mathbf{Q}_2^H\mathbf{D} \tag{2.2.65}$$

$$\boldsymbol{\Psi} = \mathbf{M}^H\mathbf{Q}_2 \tag{2.2.66}$$

$$\boldsymbol{\Gamma} = \mathbf{R}_1^{-1}\mathbf{Q}_1^H\mathbf{M} \tag{2.2.67}$$

2.3 DOA Estimation Techniques for wideband Signals

Array processing techniques can also be used to locate wideband sources. As mentioned before, for wideband signals the frequency bandwidth is relatively large compared to the center frequency. In comparison to narrowband signals, wideband signals are more complicated since a large amount of data is required and more computational effort is demanded to solve the same problem. While the time delays of narrowband signals can be approximated by their respective phase delays, wideband signals require more signal processing prior to using existing methods for solving the detection and estimation problems.

For wideband signals, most of the techniques used to solve the detection and estimation problems convert the data model from the time domain to the frequency domain. Such a conversion is motivated by two reasons. First, the data model in the frequency domain is structurally identical to the narrowband situation in the time domain, and second that all the successful techniques originally developed for narrowband models can then be reused in the set of frequency bins to solve the problem for the wideband signals.

The advantages of the signal subspace approaches for narrowband sources makes it a logical candidate for use in DOA estimation of wideband sources. On the other hand, the methods that were originally developed for narrowband sources, cannot be directly applied to wideband signals. There are a number of different approaches to wideband array processing. Wax et al. [5] has divided the wideband frequency into non-overlapping narrowband intervals, and then narrowband signal subspace processing was performed on each band. An averaging procedure was then applied to combine the individual narrowband frequency results in to a single DOA estimation. Su and Morf [37] developed a different method for which frequency domain division is not explicitly used. They developed a generalization of the one-dimensional signal subspace approach. In this method, the correlation function matrix is first estimated and then transformed into the frequency domain for applying narrowband signal subspace processing to each transformation point or any point interpolated in the frequency domain.

The above so-called incoherent signal subspace methods (ISM) have some drawbacks. First, these methods are computationally demanding since they involve an eigen-decomposition of the spectral density matrix at each frequency band being analyzed. Second, at low SNR the threshold effect prevents the final combination from being effective [38]. Moreover ISM can not effectively process coherent signals even if the SNR is infinitely high and the observation time is infinitely long.

Wang and Kaveh [6] recognized that the main difficulty in developing coherent signal subspace processing for wideband sources is due to the fact that the signal subspace at one frequency is different from that of another frequency. The basic idea of the coherent signal-subspace method (CSM) which was introduced by Wang and Kaveh [6] is to construct a single signal subspace by using a transformation matrix which translates the signal subspaces for all the frequency bands into a common one. This approach improves the DOA estimation by condensing the energy of the narrowband signals in a predefined subspace. Indeed, CSM involves the use of focusing matrices for the purpose of coherent signal subspace processing for DOA estimation of wideband signals. These focusing matrices are used for the alignment of the signal subspaces of narrowband components within the bandwidth of the signals, followed by the averaging of narrowband data covariance matrices into a single covariance matrix, thus achieving a substantial reduction in data processing. Subsequently, any signal subspace direction finding procedure, such as MUSIC, can be applied to this averaged covariance matrix to obtain the DOA estimates.

One of the most challenging issues in the coherent signal-subspace methods is to choose the best focusing frequency to decrease the estimation bias. In the past, the focusing frequency has been chosen to be the center frequency of the spectrum of the signals. If the spectrum of the signal is not symmetric around the center frequency, or the sampling in the frequency domain is not uniform, this choice is not optimal. In [39], Valaee and Kabal have introduced an optimal method for focusing subspace selection in the CSM algorithm. The approach is based on minimizing a subspace fitting error. The subspace fitting error is defined as the Euclidean distance between the focusing steering matrix and the transformed steering matrix at each frequency bin. They have shown that by using the proposed method for focusing subspace selection in the CSM algorithm, the bias of the DOA estimates is minimized and the resolution threshold SNR is reduced. Furthermore, Hung and Kaveh [40] proved that the best performance is obtained if the mapping of the subspaces is done through a unitary transformation.

2.3.1 Wideband Data Model

A uniform linear array composed of m equally spaced sensors is assumed to be in far field of d wideband sources so that a planewave approximation is valid. It is further assumed that the array of sensors are in the same plane as the wideband sources. The wideband sources are bandlimited to a common frequency band with a certain bandwidth. Moreover, the signals of the sources can be non-coherent, and partially or fully coherent. To obtain the general mathematical model of the data, the case of a single incident wavefield will be analyzed and subsequently the obtained model is generalized to the case of multiple wavefields.

For a single incident wavefield in the noise free case, the signal received at the *mth* sensor is

$$\tilde{\mathrm{x}}_l(t) = \mathrm{s}(t - \tau_l(\theta_1)) \cos(\omega_c(t - \tau_l(\theta_1)) + \phi) \quad \text{for} \quad 1 \leq l \leq m \tag{2.3.1}$$

where $\mathrm{s}(t)$ is the baseband source signal, ω_c is the center frequency, θ_1 is the azimuth angle, τ_l is the time delay associated with the *lth* sensor signal and ϕ is the phase angle. Since signal processing operations are best done at baseband frequencies, it is a standard practice in the literature to convert sensor signals by frequency down-shifting. This conversion is achieved by multiplying the received signals by the sinusoidal signals $\cos(\omega_c t)$ and $\sin(\omega_c t)$ and then lowpass filtering these products. The bandwidth of the lowpass filter has to be at least equal to the bandwidth of the source signal $\mathrm{s}(t)$. Therefore, the outputs are given by the in-phase component $\mathrm{s}(t - \tau_l(\theta_1)) \cos(\omega_c \tau_l(\theta_1) + \phi)$ and the quadrature component $\mathrm{s}(t - \tau_l(\theta_1)) \sin(\omega_c \tau_l(\theta_1) + \phi)$ for $1 \leq l \leq m$, and in the complex form

$$\mathrm{x}_l(t) = \mathrm{s}(t - \tau_l(\theta_1)) e^{j(\omega_c \tau_l(\theta_1) + \phi)} \quad \text{for} \quad 1 \leq l \leq m \tag{2.3.2}$$

in which the real and imaginary parts are the in-phase and quadrature components, respectively.

As mentioned before, the wideband data model in the frequency domain is structurally identical to the narrowband situation in the time domain. Thus, by taking the Fourier transform of these time domain signals, we have

$$\mathrm{X}_l(\omega) = \mathrm{S}(\omega)e^{j\phi}e^{-j(\omega-\omega_c)\tau_l(\theta_1)} \text{ for } 1 \leq l \leq m \tag{2.3.3}$$

where $\mathrm{S}(\omega)$ denotes the Fourier transform of the source signal $\mathrm{s}(t)$.

Let us now extend the model to the case of multiple incident wavefields. In this case, there are d wavefields incident on the array. The superposition principle indicates that the mth array sensor signal is defined by the linear combination of the separate effects of the individual wavefields. Therefore the data model in the presence of environmental noise takes the form

$$\mathrm{X}_l(\omega) = \sum_{k=1}^{d} \mathrm{S}_k(\omega)e^{j\phi_k}e^{-j(\omega-\omega_c)\tau_l(\theta_k)} + \mathrm{N}_l(\omega) \text{ for } 1 \leq l \leq m \tag{2.3.4}$$

where $\mathrm{S}_k(\omega)$ denotes the Fourier transform of the kth source signal $\mathrm{s}_k(t)$, $\tau_l(\theta_k)$ is the delay of the kth source signal associated with the mth sensor and $\mathrm{N}_l(\omega)$ denotes the noise of mth sensor. It is assumed that the noise samples are uncorrelated with the signals.

In the matrix form, the model is defined by

$$\mathbf{x}(\omega) = \mathbf{A}(\omega, \theta)\mathbf{s}(\omega) + \mathbf{n}(\omega) \tag{2.3.5}$$

where $\mathbf{x}(\omega)$ is the $m \times 1$ spectral array output vector, $\mathbf{A}(\omega, \theta)$ denotes the $m \times d$ steering matrix, $\mathbf{s}(\omega)$ is the $d \times 1$ spectral source vector and $\mathbf{n}(\omega)$ denotes the $m \times 1$ noise vector so that

$$\mathbf{x}(\omega) = [\mathrm{X}_1(\omega)\ \mathrm{X}_2(\omega)\ \ldots\ \mathrm{X}_m(\omega)]^T \tag{2.3.6}$$

$$\mathbf{s}(\omega) = [\mathrm{S}_1(\omega)e^{j\phi_1}\ \mathrm{S}_2(\omega)e^{j\phi_2}\ \ldots\ \mathrm{S}_d(\omega)e^{j\phi_d}]^T \tag{2.3.7}$$

$$\mathbf{A}(\omega, \theta) = [\mathbf{a}_1(\omega, \theta_1)\ \ \mathbf{a}_2(\omega, \theta_2)\ \ldots\ \mathbf{a}_d(\omega, \theta_d)] \tag{2.3.8}$$

$$\mathbf{n}(\omega) = [\mathrm{N}_1(\omega)\ \mathrm{N}_2(\omega)\ \ldots\ \mathrm{N}_m(\omega)]^T \tag{2.3.9}$$

and

$$\mathbf{a}_k(\omega, \theta_k) = [e^{-j(\omega-\omega_c)\tau_1(\theta_k)} \ \ldots \ e^{-j(\omega-\omega_c)\tau_m(\theta_k)}]^T \ \text{for} \ 1 \le k \le d \tag{2.3.10}$$

where the lower bold face and upper bold face are used to designate the vector and matrix quantities, respectively. It is assumed that the number of sensors m is larger than the number of sources d and that the rank of $\mathbf{A}(\omega, \theta)$ is equal to d for any frequency and angles of arrival.

The direction of arrival problem is concerned with using the noise corrupted sensor signals (2.3.5) to determine the time delays and then using the results to estimate the DOAs. Hence, for solving the direction of arrival problem, one may use the second-order statistics of the spectral array output vector. As in the narrowband situation, it is assumed that the source signals and additive noises are zero mean complex gaussian random processes which are pairwise uncorrelated. With these assumptions in mind, the spectral density matrix $\mathbf{P}_x(\omega)$ of the spectral array output is defined as

$$\mathbf{P}_x(\omega) = E\{\mathbf{x}(\omega)\mathbf{x}^H(\omega)\} \tag{2.3.11}$$

It can be shown that this spectral density matrix is equal to the Fourier transform of the covariance matrix i.e. $\mathbf{R}_x(\tau) = E\{\mathbf{x}(t+\tau)\mathbf{x}^H(t)\}$ where $\mathbf{x}(t)$ denotes the $m \times 1$ snapshot vector whose components are given in expression (2.3.2). Using expression (2.3.5) in (2.3.11), the spectral density matrix takes the form

$$\begin{aligned} \mathbf{P}_x(\omega) &= \mathbf{A}(\omega)E\{\mathbf{s}(\omega)\mathbf{s}^H(\omega)\}\mathbf{A}^H(\omega) + E\{\mathbf{n}(\omega)\mathbf{n}^H(\omega)\} \\ &= \mathbf{A}(\omega)\mathbf{P}_s(\omega)\mathbf{A}^H(\omega) + \sigma^2(\omega)\mathbf{P}_n(\omega) \end{aligned} \tag{2.3.12}$$

The $d \times d$ source spectral density matrix $\mathbf{P}_s(\omega)$ that defines the second order statistical relationship between the d source signals taken as pairs at frequency ω, is given by

$$\mathbf{P}_s(\omega) = E\{\mathbf{s}(\omega)\mathbf{s}^H(\omega)\} \tag{2.3.13}$$

It should be noted that if the source spectral density matrix $\mathbf{P}_s(\omega)$ is diagonal, then the d source signals are said to be pairwise non-coherent. Moreover, a subset of the source signals are coherent if this matrix is non-diagonal and singular. Similarly, a non-diagonal and non-singular source spectral density matrix indicates that the multiple source signals are partially coherent [17]. Finally, the $m \times m$ noise spectral density matrix $\mathbf{P}_n(\omega)$ is assumed to be known (e.g from measurements with no signals present) except for the spectral level $\sigma^2(\omega)$.

In practical applications, the spectral density matrix $\mathbf{P}_x(\omega)$ is unknown and only a set of sampled array sensor outputs are given

$$\mathrm{x}_l(T),\ \mathrm{x}_l(2T),\ \ldots,\ \mathrm{x}_l(nT) \quad \text{for} \quad 1 \leq l \leq m \tag{2.3.14}$$

where T denotes the sampling period and n is the number of samples. With these samples being taken over a time interval of T_0 seconds, the sampling period is determined as $T = T_0/n$. In order to estimate the spectral density matrix, let these samples be partitioned into Q equal subintervals each consisting of $N = n/Q$ samples so that

$$\begin{gathered} \mathrm{x}_l^q(nT) = \mathrm{x}_l(nT + (q-1)NT) \\ \text{for} \quad 1 \leq l \leq m \quad \text{and} \quad 1 \leq q \leq Q \end{gathered} \tag{2.3.15}$$

where the superscript q denotes the qth subinterval. By taking the N point discrete Fourier transform of these sequences (2.3.15) we have

$$\begin{gathered} \mathrm{X}_l^q(\omega_j) = DFT[\mathrm{x}_l^q(n)] \\ \text{for} \quad 0 \leq j \leq N-1 \quad \text{and} \quad 1 \leq q \leq Q \end{gathered} \tag{2.3.16}$$

where ω_j denotes the jth narrowband frequency that takes on the discrete values $\frac{2\pi j}{N}$ for $0 \leq j \leq N-1$.

Now, let $\mathbf{x}_q(\omega_j)$ denotes the $m \times 1$ Fourier coefficient vector computed at frequency ω_j of the qth subinterval, i.e.

$$\mathbf{x}_q(\omega_j) = [\mathrm{X}_1^q(\omega_j)\ \mathrm{X}_2^q(\omega_j)\ \ldots\ \mathrm{X}_m^q(\omega_j)]^T \quad \text{for} \quad 1 \leq q \leq Q \tag{2.3.17}$$

It can be shown [41] that for sufficiently large subinterval duration (i.e. $\Delta T = \frac{T_0}{Q}$) the decomposed components $\mathbf{x}_q(\omega_j)$ are uncorrelated. In other words, if the correlation time of the signal is sufficiently smaller than the length of a snapshot, the Fourier transformed data at different frequency bins are approximately uncorrelated and the maximum likelihood estimation of its covariance matrix $\hat{\mathbf{R}}_x(\omega_j)$ for the jth frequency ω_j is expressed as

$$\hat{\mathbf{R}}_x(\omega_j) = E\{\mathbf{x}(\omega_j)\mathbf{x}^H(\omega_j)\} = \frac{1}{Q}\sum_{q=1}^{Q}\mathbf{x}_q(\omega_j)\mathbf{x}_q^H(\omega_j) \tag{2.3.18}$$

To reduce the computational cost when using the signal eigen-decomposition method for estimating the DOAs, it is rational that only those frequencies ω_j be used for which the SNR ratios are sufficiently large. Therefore, if $\{\omega_1,\ \omega_2,\ \ldots,\ \omega_J\}$ designate the set of frequencies contained in the set $\{\omega_j = \frac{2\pi j}{N} \ \text{for}\ \ 0 \leq j \leq N-1\}$ for which the SNR are deemed suitably large, then we have

$$\hat{\mathbf{R}}_x(\omega_j) \approx \frac{1}{Q}\sum_{q=1}^{Q}\mathbf{x}_q(\omega_j)\mathbf{x}_q^H(\omega_j) \quad \text{for} \quad 1 \leq j \leq J \tag{2.3.19}$$

where J is the number of frequency bins to be considered and ω_j is within the bandwidth.

2.3.2 Coherent Signal Subspace Method (CSM)

In order to have a significant improvement in the DOA estimation performance, it is possible to combine the signal subspaces and direction information at all frequencies for which the SNRs are sufficiently large. Suppose the steering matrices $\mathbf{A}(\omega_j)$ for $1 \leq j \leq J$ have been separately determined. Since the steering matrix is a function of the frequency and consequently the range spaces of these steering matrices are generally not the same for different frequencies, the signal subspace at one frequency bin is different from that of another frequency, and we cannot simply take their average to obtain an improved DOA estimation. Wang and Kaveh [6] proposed the coherent signal subspace method (CSM) whose objective is to transform the signal subspaces of the narrowband components within the common bandwidth of the signals followed by an averaging of these aligned signal subspaces. In other words, the CSM algorithm transforms the steering matrices at different frequencies to a common frequency ω_0 (focusing frequency) using focusing matrices $\mathbf{T}_j$. The following result presented in [6] conveys the basic concepts of the CSM algorithm for a general array geometry.

Theorem 2.3.1. *Under the condition that each steering matrix* $\mathbf{A}(\omega_j)$, for $1 \leq j \leq J$ *has rank d, there exist* $m \times m$ *nonsingular matrices* $\mathbf{T}(\omega_j)$ for $1 \leq j \leq J$ *such that*

$$\mathbf{T}(\omega_j)\mathbf{A}(\omega_j) = \mathbf{A}(\omega_0) \quad \text{for} \quad 1 \leq j \leq J \tag{2.3.20}$$

Proof. See [6]. □

Note that the focusing matrices $\mathbf{T}(\omega_\mathrm{j})$ for $1 \leq j \leq J$ are non-unique. Assume the steering matrices $\mathbf{A}(\omega_j)$'s are transformed by the focusing matrices $\mathbf{T}(\omega_j)$'s to the vicinity of the focusing steering matrix $\mathbf{A}(\omega_0)$. The transformed steering matrices form a cluster around $\mathbf{A}(\omega_0)$. It is quite clear that the closer the transformed matrices are, the better the performance is. In an ideal case all the transformed location matrices superimpose on $\mathbf{A}(\omega_0)$. This case is called the perfect focusing. In perfect focusing, the column vectors of the steering matrices $\mathbf{A}(\omega_j)$'s are transformed to the corresponding column vectors of

$\mathbf{A}(\omega_0)$. This is also seen from the characteristics of the Frobenius norm, that is, the square of the Frobenius norm of a matrix is equal to sum of the square of the Euclidean norm of the column vectors. Thus, using different focusing matrices leads to different performance capabilities. In the following, we will consider two classes of focusing matrices known as diagonal and unitary focusing matrices.

Diagonal Focusing Matrix

In the array signal processing literature, several classes of focusing matrices have been suggested e.g., the diagonal focusing matrices [6], the unitary focusing matrices [40], signal subspace transformation [42], array manifold interpolation [43], the unitary constrained array manifold focusing [44], minimum integral square error [45],[46], among others. However, here we will only consider the diagonal focusing matrices and later the unitary focusing matrices. It is clear that construction of $\mathbf{T}(\omega_\mathrm{j})$ requires a knowledge of the unknown DOAs. Therefore, the first step in estimating $\mathbf{T}(\omega_\mathrm{j})$ is to perform an initial estimate of the angles. Using a classical beamforming gives an estimate of the angles of arrival which can be used in (2.3.20). Suppose all the true angles of arrival are within the neighborhood of preliminary angle θ_0. Then the diagonal focusing matrices $\mathbf{T}(\omega_j)$ can be estimated as [6]

$$\hat{\mathbf{T}}(\omega_j) = \begin{bmatrix} \frac{\mathrm{a}_1(\omega_0,\theta_0)}{\mathrm{a}_1(\omega_j,\theta_0)} & 0 & 0 & \cdots & 0 \\ 0 & \frac{\mathrm{a}_2(\omega_0,\theta_0)}{\mathrm{a}_2(\omega_j,\theta_0)} & \vdots & \vdots & \vdots \\ 0 & 0 & \ddots & 0 & 0 \\ \vdots & \vdots & \vdots & \frac{\mathrm{a}_{m-1}(\omega_0,\theta_0)}{\mathrm{a}_{m-1}(\omega_j,\theta_0)} & 0 \\ 0 & \cdots & 0 & 0 & \frac{\mathrm{a}_m(\omega_0,\theta_0)}{\mathrm{a}_m(\omega_j,\theta_0)} \end{bmatrix} \tag{2.3.21}$$

where $\mathrm{a}_l(\omega_j,\theta_0)$ is the *lth* element of the steering vector $\mathbf{a}(\omega_\mathrm{j},\theta_0)$. In the case of uniform linear array we have

$$\hat{\mathbf{T}}_{ULA}(\omega_j) = \begin{bmatrix} 1 & 0 & 0 & \cdots & 0 \\ 0 & e^{-j\frac{1}{c}(\omega_0-\omega_j)\Delta\sin\theta_0} & \vdots & \vdots & \vdots \\ 0 & 0 & \ddots & 0 & 0 \\ \vdots & \vdots & \vdots & e^{-j\frac{1}{c}(\omega_0-\omega_j)(m-2)\Delta\sin\theta_0} & 0 \\ 0 & \cdots & 0 & 0 & e^{-j\frac{1}{c}(\omega_0-\omega_j)(m-1)\Delta\sin\theta_0} \end{bmatrix} \tag{2.3.22}$$

where Δ is the spacing between adjacent sensors and c is the velocity of wave propagation. Furthermore, focusing matrices $\mathbf{T}(\omega_j)$ for a uniform circular array of m sensors takes the form

$$\hat{\mathbf{T}}_{UCA}(\omega_j) = \begin{bmatrix} e^{-j(\omega_0-\omega_j)\tau_1(\theta_0)} & 0 & 0 & \cdots & 0 \\ 0 & e^{-j(\omega_0-\omega_j)\tau_2(\theta_0)} & \vdots & \vdots & \vdots \\ 0 & 0 & \ddots & 0 & 0 \\ \vdots & \vdots & \vdots & e^{-j(\omega_0-\omega_j)\tau_{l-1}(\theta_0)} & 0 \\ 0 & \cdots & 0 & 0 & e^{-j(\omega_0-\omega_j)\tau_l(\theta_0)} \end{bmatrix} \tag{2.3.23}$$

where

$$\tau_l(\theta_0) = \frac{1}{c}\left(\cos\left(\frac{2\pi(l-1)}{m}\right)\cos\theta_0 + \sin\left(\frac{2\pi(l-1)}{m}\right)\sin\theta_0\right) \quad \text{for} \quad 1 \leq l \leq m \tag{2.3.24}$$

Let us now consider the effects of the focusing operation. Using the focusing matrices $\hat{\mathbf{T}}(\omega_j)$, the observation vectors at different frequency bins are transformed into the focusing subspace. In particular, the random vector $\mathbf{x}(\omega_j)$ is transformed to the random vector $\mathbf{y}(\omega_j)$ such that

$$\mathbf{y}(\omega_j) = \hat{\mathbf{T}}(\omega_j)\mathbf{x}(\omega_j) \quad \text{for} \quad 1 \leq j \leq J \tag{2.3.25}$$

These transformed observation vectors are used to construct the transformed covariance matrices

$$\hat{\mathbf{R}}_y(\omega_j) = E\{\mathbf{y}(\omega_j)\mathbf{y}^H(\omega_j)\} = \frac{1}{Q}\sum_{q=1}^{Q}\mathbf{y}_q(\omega_j)\mathbf{y}_q^H(\omega_j) \quad \text{for} \quad 1 \leq j \leq J \tag{2.3.26}$$

An average of these aligned covariance matrices over the frequency bins gives a universal focused covariance matrix $\hat{\mathbf{R}}$ that can be used for DOA estimation and takes the form

$$\hat{\mathbf{R}} = \sum_{j=1}^{J} \mathrm{w}_j E\{\mathbf{y}(\omega_j)\mathbf{y}^H(\omega_j)\} \tag{2.3.27}$$

where w_j is a normalized weight selected to be proportional to the SNR of the *jth* frequency band. Using (2.3.12), (2.3.20) and (2.3.25) in (2.3.27) gives

$$\begin{aligned} \hat{\mathbf{R}} &= \sum_{j=1}^{J} \mathrm{w}_j \hat{\mathbf{T}}(\omega_j) E\{\mathbf{x}(\omega_j)\mathbf{x}^H(\omega_j)\}\hat{\mathbf{T}}^H(\omega_j) \\ &= \mathbf{A}(\omega_0)\hat{\mathbf{R}}_s\mathbf{A}^H(\omega_0) + \sigma_n^2\hat{\mathbf{R}}_n \end{aligned} \tag{2.3.28}$$

where

$$\hat{\mathbf{R}}_s = \sum_{j=1}^{J} \mathrm{w}_j \mathbf{P}_s(\omega_j) \tag{2.3.29}$$

and

$$\hat{\mathbf{R}}_n = \sum_{j=1}^{J} \mathrm{w}_j \hat{\mathbf{T}}(\omega_j)\mathbf{P}_n(\omega_j)\hat{\mathbf{T}}^H(\omega_j) \tag{2.3.30}$$

Unitary Focusing Matrix

The focusing transformation improves the efficiency of the estimation by condensing the energy of sub-bands in the focusing signal subspace. In spite of this, it is seen that the focusing removes the whiteness of the noise and this in turn causes to changes to the SNR. The focusing loss is defined as the ratio of the array SNR after and before focusing. Using this concept, Hung and Kaveh [40] have shown that the focusing is lossless if the focusing matrices are unitary. They have proposed the following transformation matrices which are obtained by the constrained minimization problem

$$\min_{\mathbf{T}(\omega_j)} \|\mathbf{A}(\omega_0) - \mathbf{T}(\omega_j)\mathbf{A}(\omega_j)\|_F \quad \text{for} \quad 1 \le j \le J \tag{2.3.31}$$

such that

$$\mathbf{T}(\omega_j)^H \mathbf{T}(\omega_j) = \mathbf{I}$$

where $\|.\|_F$, the Frobenius matrix norm that is defined as

$$\|B\|_F = \left[\sum_{i,j} b_{ij}^2\right]^{\frac{1}{2}} = \left[tr(\mathbf{B}^H\mathbf{B})\right]^{\frac{1}{2}} \tag{2.3.32}$$

In fact, this transformation involves the rotation of the jth narrowband signal subspace, *span* $\{\mathbf{A}(\omega_j)\}$, to make it as close as possible in the Forbenius norm sense to the focusing signal subspace, *span* $\{\mathbf{A}(\omega_0)\}$, without changing the noise covariance matrix. In order to find the solution to (2.3.31), we have the following theorem [40].

Theorem 2.3.2. *Given the two matrices* $\mathbf{A}(\omega_0)$ *and* $\mathbf{A}(\omega_j)$*, a solution to (2.3.31) is given by*

$$\mathbf{T}(\omega_j) = \mathbf{V}(\omega_j)\mathbf{U}(\omega_j)^H \tag{2.3.33}$$

where the columns of $\mathbf{U}(\omega_j)$ *and* $\mathbf{V}(\omega_j)$ *are the left and right singular vectors of* $\mathbf{A}(\omega_j)\mathbf{A}(\omega_0)^H$ *respectively.*

Proof. See [40] and [47] ☐

2.3.3 Selection of the Focusing Frequency

As mentioned before, Hung and Kaveh [40] proved that the best performance is obtained if the mapping of the subspaces is done through a unitary transformation. However, they did not discuss how to choose the best focusing subspace. A simple selection for the focusing frequency is the center frequency of the spectrum of the signals. But, if the spectrum of the signal is not symmetric around the center frequency, or the sampling in the frequency domain is not uniform, this choice is not optimal. Thus, one of the most challenging issues in the coherent signal-subspace method is the choice of the best focusing frequency to decrease the estimation bias. Valaee and Kabal [39], have introduced an optimal method for focusing subspace selection in the CSM algorithm.

The approach is based on minimizing a subspace fitting error. The subspace fitting error is defined as the Euclidean distance between the focusing steering matrix and the transformed steering matrix at each frequency bin. In other words, the criterion for focusing frequency selection is based on the error involved in the transformation of the signal subspaces, and the minimization of this criterion gives the focusing frequency. They have shown that by using the proposed method for focusing subspace selection in the CSM algorithm the resolution threshold of SNR is reduced and the bias of the DOA estimate is minimized. Specifically, they have chosen a focusing frequency which is selected by

$$\begin{gathered}\min_{\omega_0}\min_{T(\omega_j)}\sum_{j=1}^{J}\mathrm{w}_j\,\|\mathbf{A}(\omega_0)-\mathbf{T}(\omega_j)\mathbf{A}(\omega_j)\|_F^2 \\ \text{s.t. } \mathbf{T}(\omega_j)^H\mathbf{T}(\omega_j)=\mathbf{I} \\ \mathbf{A}(\omega_0)\in\mathcal{A}(\theta)\end{gathered} \tag{2.3.34}$$

where $\mathcal{A}(\theta)$ is the set of all steering matrices for given DOA θ and w_j is a weighting factor proportional to the SNR at the jth frequency bin with $\sum_{j=1}^{J}\mathrm{w}_j=1$. Using (2.3.33), the subspace fitting error is given by

$$\begin{aligned}\epsilon_j &= \sum_{j=1}^{J} \mathrm{w}_j \left\| \mathbf{A}(\omega_0) - \mathbf{T}(\omega_j)\mathbf{A}(\omega_j) \right\|_F^2 \\ &= \sum_{j=1}^{J} \mathrm{w}_j \Big[\left\|\mathbf{A}(\omega_0)\right\|_F^2 + \left\|\mathbf{A}(\omega_j)\right\|_F^2 - 2\Re\{tr(\mathbf{A}(\omega_0)\mathbf{A}(\omega_j)^H \mathbf{T}(\omega_j)^H)\} \Big] \\ &= 2Jmd - 2\sum_{j=1}^{J}\sum_{k=1}^{d} \mathrm{w}_j \sigma_k(\mathbf{A}(\omega_0)\mathbf{A}(\omega_j)^H) \end{aligned} \tag{2.3.35}$$

where $\sigma_k(\mathbf{A}(\omega_0)\mathbf{A}(\omega_j)^H)$ for $k = 1, \ldots, d$ are the singular values of the matrix $\mathbf{A}(\omega_0)\mathbf{A}(\omega_j)^H$ arranged in non-increasing order. In above, the following equality has been used

$$\|\mathbf{A}\|_F^2 = \sum_{k=1}^{d} \|\mathbf{a}_k\|_F^2 = md \tag{2.3.36}$$

which is true for an arbitrary array manifold.

From (2.3.35) it is seen that the minimization problem (2.3.34) is equivalent to the following maximization

$$\max_{\omega_0} \sum_{j=1}^{J}\sum_{k=1}^{d} \mathrm{w}_j \sigma_k(\mathbf{A}(\omega_0)\mathbf{A}(\omega_j)^H) \quad \text{s.t. } \mathbf{A}(\omega_0) \in \mathcal{A}(\theta) \tag{2.3.37}$$

Direct maximization of (2.3.37) is complicated and the computational complexity increases with the number of frequency samples. Valaee and Kabal [39] used a suboptimal method which is based on maximizing an upper bound to (2.3.37). They have shown that in the vicinity of the maximum point the bound is tight. The tightness of the bound at the maximum point indicates that the method performs very close to the optimal case. The following lemma [39], establishes a lower bound on the norm of the difference of two matrices.

Lemma 2.3.3. *If* $\mathbf{E}$ *and* $\mathbf{F}$ *are two* $m \times n$ *matrices with ordered singular values* $\sigma_1(\mathbf{E}) \geqslant$

$\cdots \geqslant \sigma_q(\mathbf{E}) \geqslant 0$ *and* $\sigma_1(\mathbf{F}) \geqslant \cdots \geqslant \sigma_q(\mathbf{F}) \geqslant 0$, *where* $q = \min\{m, n\}$, *then*

$$\|\mathbf{E} - \mathbf{F}\|_F^2 \geqslant \sum_{i=1}^{q} [\sigma_i(\mathbf{E}) - \sigma_i(\mathbf{F})]^2 \tag{2.3.38}$$

Proof. See [47]. □

Using (2.3.38) to (2.3.35) gives

$$\sum_{j=1}^{J} \sum_{k=1}^{d} \mathrm{w_j} \sigma_k(\mathbf{A}(\omega_0)\mathbf{A}(\omega_j)^H) \leqslant \sum_{j=1}^{J} \sum_{k=1}^{d} \mathrm{w_j} \sigma_k(\mathbf{A}(\omega_0))\sigma(\mathbf{A}(\omega_j)^H) \tag{2.3.39}$$

The proposed method is based on maximization of the right hand side of (2.3.39) i.e.

$$\max_{\omega_0} \sum_{j=1}^{J} \sum_{k=1}^{d} \mathrm{w_j} \sigma_k(\mathbf{A}(\omega_0))\sigma(\mathbf{A}(\omega_j)^H) \tag{2.3.40}$$

$$\text{s.t.} \quad \mathbf{A}(\omega_0) \in \mathcal{A}(\theta)$$

In order to perform this maximization, the singular values of the focusing steering matrix $\mathbf{A}(\omega_0)$ are determined and then using the known structure of the steering matrix the focusing frequency ω_0 is found. Thus, the maximization problem (2.3.40) can be written as

$$\max_{\omega_0} \sum_{k=1}^{d} \mu_k \sigma_k(\mathbf{A}(\omega_0)) \tag{2.3.41}$$

$$\text{s.t.} \quad \mathbf{A}(\omega_0) \in \mathcal{A}(\theta)$$

where μ_k is defined as

$$\mu_k \triangleq \sum_{j=1}^{J} \mathrm{w_j} \sigma_k(\mathbf{A}(\omega_j)) \tag{2.3.42}$$

This is a one variable maximization problem that can be solved by searching for the best ω_0 in the interval of interest. It is seen that the computational complexity for the maximization in (2.3.41) is independent of the number of frequency samples.

2.4 Conclusion

In this chapter, the fundamental issues and problems relating to both the narrowband and the wideband array signal processing techniques were provided. The narrowband data model was presented followed by a brief exposition of the different array geometries and the introduction to the array manifold. Definitions for non-coherent, partially coherent and coherent sources were also included. The multiple signal classification (MUSIC) and the weighted subspace fitting (WSF) direction of arrival (DOA) estimation techniques characterized by the eigen-decomposition of the sample covariance matrix were studied.

Data model for the challenging wideband signals were derived. The incoherent signal subspace method (ISM) and the coherent signal subspace method (CSM) were considered. The derivation for the diagonal focusing matrices and unitary focusing matrices were also performed in this chapter. Finally, the selection of the optimum focusing frequency for the CSM scheme was considered.

Chapter 3

Development of Wideband Methods to Specific Geometries of Sensors using the MUSIC Algorithm

3.1 Introduction

While the majority of research efforts in array processing have so far been given to uniform linear arrays (ULAs), attempts have been made to apply and extend the results to other array geometries such as uniform circular array, uniform rectangular array and so on. There are distinct advantages for pursuing these attempts. For example, the most obvious advantage in the use of UCAs in comparison to ULAs is the UCAs ability to provide a full azimuth coverage, which is the result of their two-dimensional array structure. Furthermore, when called for, UCAs can provide a 180° coverage in the elevation. On the other hand, while one UCA is able to provide the full azimuth coverage, at least three separate ULAs are required for the same task in which each array covers a 120° sector. Therefore, the use of UCAs can lead to a reduction in hardware requirements. In comparison to other array geometries, ULAs also suffer from decreasing effective array aperture as the look direction changes while for the UCAs with a reasonable number of sensors, the effective array aperture is almost constant over any look direction in the azimuth. Despite these advantages, many useful array processing techniques that were derived for ULAs have not been extended to other array geometries.

In this chapter, we will first consider an array geometry that consists of several nodes in which each node is a 5-element half-wavelength spaced cross shaped subarray. Then, numerical examples and simulation results using these array geometries for both the narrowband and wideband signals using MUSIC and CSM algorithms will be presented.

3.2 Cross Shaped Array Geometry

In this section, we consider four types of array geometries that are of interest. Fig. 3.2 shows these array geometries known as linear cross shaped array (LCSA), diagonal cross shaped array (DCSA), triangular cross shaped array (TCSA) and square cross shaped array (SCSA) where the space between two elements in each node is equal to half-wavelength and the distance between two vicinal nodes can change with a multiplication of half-wavelength. It should be noted that in the case of linear geometries the distance between two nodes is defined as the distance between the most left hand sensor and the most right hand sensor. In the case of diagonal geometries, this distance is defined as the nearest distance between two upper and two lower sensors diagonally. In computer simulations, we will find that both the node topology and the aperture are important i.e., the performance capabilities of the techniques used in array processing will be modified by variation of these parameters.

Assume that the location of the sensors in the xy-plane are

$$\mathbf{r} = \begin{bmatrix} x_1 & x_2 & \cdots & x_m \\ y_1 & y_2 & \cdots & y_m \end{bmatrix} \tag{3.2.1}$$

To find the array steering matrix for an arbitrary array geometry, equation (2.2.13) can

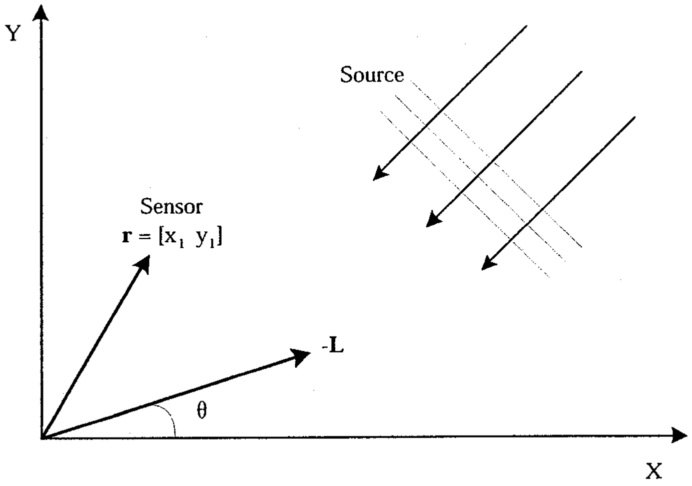

Figure 3.1: Two dimensional array geometry (**r** is the location of sensors and **L** is the wave vector).

be substituted by

$$\mathbf{a}(\theta_k) = e^{-j\mathbf{r}^T\mathbf{L}(\theta_k)} \quad \text{for} \quad 1 \leq k \leq d \tag{3.2.2}$$

where

$$\mathbf{L}(\theta_k) = \frac{2\pi}{\lambda}\begin{bmatrix}\cos\theta_k & \sin\theta_k\end{bmatrix}^T \quad \text{for} \quad 1 \leq k \leq d \tag{3.2.3}$$

is defined as the wave vector and θ_k is the direction of the kth signal propagation, defined counter clockwise relative to the x-axis (Fig. 3.1).

In order to develop and implement the MUSIC algorithm (refer to equation (2.2.32)) using the array geometries presented above, the steering matrices for these array geometries are derived below.

Linear Cross Shaped Array Geometry

In the following, the array steering matrix for a linear cross shaped array (LCSA) consists of two nodes (Fig. 3.2.a with two nodes i.e. $m = 10$) with the distance between the nodes equal to half-wavelength will be derived. For this purpose, assume that the location of

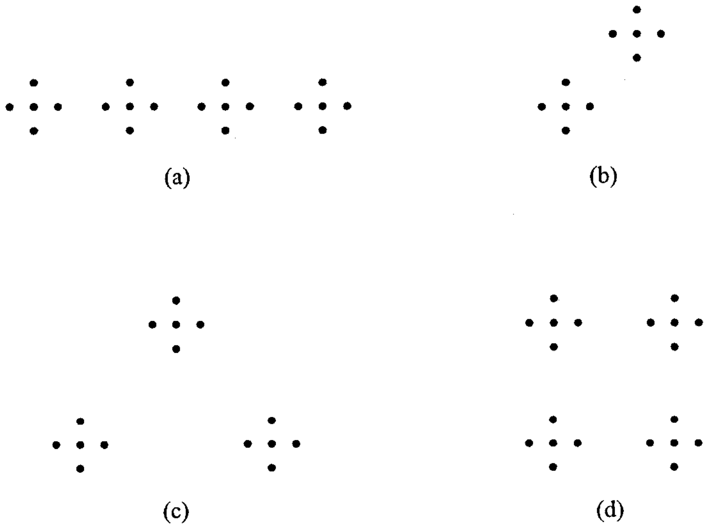
(a) (b) (c) (d)

Figure 3.2: Four different types of array geometries using the cross shaped nodes a) Linear Cross Shaped Geometry composed of four nodes, b) Diagonal Cross Shaped Geometry, c) Triangular Cross Shaped Geometry, and d) Squared Cross Shaped Geometry. The space between the two elements in each node is equal to half-wavelength and the distance between the two vicinal nodes can change with a multiplication of half-wavelength.

the sensors in the xy-plane are

$$\mathbf{r} = \Delta \times \begin{bmatrix} 0 & 1 & 2 & 1 & 1 & 3 & 4 & 5 & 4 & 4 \\ 0 & 0 & 0 & 1 & -1 & 0 & 0 & 0 & 1 & -1 \end{bmatrix} \tag{3.2.4}$$

Substituting this matrix in the equation (3.2.2) and using the equations (3.2.3) and (2.2.13) the array steering matrix (if the number of sources is equal to d) takes the form

$$\mathbf{A}_{LCSA}(\theta) = \begin{bmatrix} 0 & 0 & \cdots & 0 \\ e^{-j\frac{2\pi\Delta}{\lambda}\cos\theta_1} & e^{-j\frac{2\pi\Delta}{\lambda}\cos\theta_2} & \cdots & e^{-j\frac{2\pi\Delta}{\lambda}\cos\theta_d} \\ e^{-j\frac{2\pi\Delta}{\lambda}2\cos\theta_1} & e^{-j\frac{2\pi\Delta}{\lambda}2\cos\theta_2} & \cdots & e^{-j\frac{2\pi\Delta}{\lambda}2\cos\theta_d} \\ e^{-j\frac{2\pi\Delta}{\lambda}(\cos\theta_1+\sin\theta_1)} & e^{-j\frac{2\pi\Delta}{\lambda}(\cos\theta_2+\sin\theta_2)} & \cdots & e^{-j\frac{2\pi\Delta}{\lambda}(\cos\theta_d+\sin\theta_d)} \\ e^{-j\frac{2\pi\Delta}{\lambda}(\cos\theta_1-\sin\theta_1)} & e^{-j\frac{2\pi\Delta}{\lambda}(\cos\theta_2-\sin\theta_2)} & \cdots & e^{-j\frac{2\pi\Delta}{\lambda}(\cos\theta_d-\sin\theta_d)} \\ e^{-j\frac{2\pi\Delta}{\lambda}3\cos\theta_1} & e^{-j\frac{2\pi\Delta}{\lambda}3\cos\theta_2} & \cdots & e^{-j\frac{2\pi\Delta}{\lambda}3\cos\theta_d} \\ e^{-j\frac{2\pi\Delta}{\lambda}4\cos\theta_1} & e^{-j\frac{2\pi\Delta}{\lambda}4\cos\theta_2} & \cdots & e^{-j\frac{2\pi\Delta}{\lambda}4\cos\theta_d} \\ e^{-j\frac{2\pi\Delta}{\lambda}5\cos\theta_1} & e^{-j\frac{2\pi\Delta}{\lambda}5\cos\theta_2} & \cdots & e^{-j\frac{2\pi\Delta}{\lambda}5\cos\theta_d} \\ e^{-j\frac{2\pi\Delta}{\lambda}(4\cos\theta_1+\sin\theta_1)} & e^{-j\frac{2\pi\Delta}{\lambda}(4\cos\theta_2+\sin\theta_2)} & \cdots & e^{-j\frac{2\pi\Delta}{\lambda}(4\cos\theta_d+\sin\theta_d)} \\ e^{-j\frac{2\pi\Delta}{\lambda}(4cos\theta_1-\sin\theta_1)} & e^{-j\frac{2\pi\Delta}{\lambda}(4\cos\theta_2-\sin\theta_2)} & \cdots & e^{-j\frac{2\pi\Delta}{\lambda}(4\cos\theta_d-\sin\theta_d)} \end{bmatrix} \tag{3.2.5}$$

Diagonal Cross Shaped Array Geometry

Assume that the location of the sensors for the diagonal cross shaped array consists of two nodes (Fig. 3.2.b with $m = 10$) with the distance between the nodes equal to $\sqrt{2}\Delta$ in the xy-plane are

$$\mathbf{r} = \Delta \times \begin{bmatrix} 0 & 1 & 2 & 1 & 1 & 2 & 3 & 4 & 3 & 3 \\ 0 & 0 & 0 & 1 & -1 & 2 & 2 & 2 & 3 & 1 \end{bmatrix} \tag{3.2.6}$$

Therefore, the array steering matrix for the diagonal cross shaped array (DCSA) geometry takes the form

$$\mathbf{A}_{DCSA}(\theta) = \begin{bmatrix} 0 & 0 & \cdots & 0 \\ e^{-j\frac{2\pi\Delta}{\lambda}\cos\theta_1} & e^{-j\frac{2\pi\Delta}{\lambda}\cos\theta_2} & \cdots & e^{-j\frac{2\pi\Delta}{\lambda}\cos\theta_d} \\ e^{-j\frac{2\pi\Delta}{\lambda}2\cos\theta_1} & e^{-j\frac{2\pi\Delta}{\lambda}2\cos\theta_2} & \cdots & e^{-j\frac{2\pi\Delta}{\lambda}2\cos\theta_d} \\ e^{-j\frac{2\pi\Delta}{\lambda}(\cos\theta_1+\sin\theta_1)} & e^{-j\frac{2\pi\Delta}{\lambda}(\cos\theta_2+\sin\theta_2)} & \cdots & e^{-j\frac{2\pi\Delta}{\lambda}(\cos\theta_d+\sin\theta_d)} \\ e^{-j\frac{2\pi\Delta}{\lambda}(\cos\theta_1-\sin\theta_1)} & e^{-j\frac{2\pi\Delta}{\lambda}(\cos\theta_2-\sin\theta_2)} & \cdots & e^{-j\frac{2\pi\Delta}{\lambda}(\cos\theta_d-\sin\theta_d)} \\ e^{-j\frac{2\pi\Delta}{\lambda}(2\cos\theta_1+2\sin\theta_1)} & e^{-j\frac{2\pi\Delta}{\lambda}(2\cos\theta_2+2\sin\theta_2)} & \cdots & e^{-j\frac{2\pi\Delta}{\lambda}(2\cos\theta_d+2\sin\theta_d)} \\ e^{-j\frac{2\pi\Delta}{\lambda}(3\cos\theta_1+2\sin\theta_1)} & e^{-j\frac{2\pi\Delta}{\lambda}(3\cos\theta_2+2\sin\theta_2)} & \cdots & e^{-j\frac{2\pi\Delta}{\lambda}(3\cos\theta_d+2\sin\theta_d)} \\ e^{-j\frac{2\pi\Delta}{\lambda}(4\cos\theta_1+2\sin\theta_1)} & e^{-j\frac{2\pi\Delta}{\lambda}(4\cos\theta_2+2\sin\theta_2)} & \cdots & e^{-j\frac{2\pi\Delta}{\lambda}(4\cos\theta_d+2\sin\theta_d)} \\ e^{-j\frac{2\pi\Delta}{\lambda}(3\cos\theta_1+3\sin\theta_1)} & e^{-j\frac{2\pi\Delta}{\lambda}(3\cos\theta_2+3\sin\theta_2)} & \cdots & e^{-j\frac{2\pi\Delta}{\lambda}(3\cos\theta_d+3\sin\theta_d)} \\ e^{-j\frac{2\pi\Delta}{\lambda}(3\cos\theta_1+\sin\theta_1)} & e^{-j\frac{2\pi\Delta}{\lambda}(3\cos\theta_2+\sin\theta_2)} & \cdots & e^{-j\frac{2\pi\Delta}{\lambda}(3\cos\theta_d+\sin\theta_d)} \end{bmatrix} \tag{3.2.7}$$

Triangular Cross Shaped Array Geometry

Similar to the two previous geometries suppose that the location of the sensors for the triangular cross shaped array (Fig. 3.2.c with $m = 15$) with the distance among the nodes equal to five-wavelength in the xy-plane is given by

$$\mathbf{r} = \Delta \times \begin{bmatrix} 0 & 1 & 2 & 1 & 1 & 7 & 8 & 9 & 8 & 8 & 0 & 1 & 2 & 1 & 1 \\ 0 & 0 & 0 & 1 & -1 & 0 & 0 & 0 & 1 & -1 & 7 & 7 & 7 & 8 & 6 \end{bmatrix} \tag{3.2.8}$$

Thus, the array steering matrix for the triangular cross shaped array (TCSA) geometry (if the number of sources is equal to d) can be presented by

$$\mathbf{A}_{TCSA}(\theta) = \begin{bmatrix} 0 & 0 & \cdots & 0 \\ e^{-j\frac{2\pi\Delta}{\lambda}\cos\theta_1} & e^{-j\frac{2\pi\Delta}{\lambda}\cos\theta_2} & \cdots & e^{-j\frac{2\pi\Delta}{\lambda}\cos\theta_d} \\ e^{-j\frac{2\pi\Delta}{\lambda}2\cos\theta_1} & e^{-j\frac{2\pi\Delta}{\lambda}2\cos\theta_2} & \cdots & e^{-j\frac{2\pi\Delta}{\lambda}2\cos\theta_d} \\ e^{-j\frac{2\pi\Delta}{\lambda}(\cos\theta_1+\sin\theta_1)} & e^{-j\frac{2\pi\Delta}{\lambda}(\cos\theta_2+\sin\theta_2)} & \cdots & e^{-j\frac{2\pi\Delta}{\lambda}(\cos\theta_d+\sin\theta_d)} \\ e^{-j\frac{2\pi\Delta}{\lambda}(\cos\theta_1-\sin\theta_1)} & e^{-j\frac{2\pi\Delta}{\lambda}(\cos\theta_2-\sin\theta_2)} & \cdots & e^{-j\frac{2\pi\Delta}{\lambda}(\cos\theta_d-\sin\theta_d)} \\ e^{-j\frac{2\pi\Delta}{\lambda}7\cos\theta_1} & e^{-j\frac{2\pi\Delta}{\lambda}7\cos\theta_2} & \cdots & e^{-j\frac{2\pi\Delta}{\lambda}7\cos\theta_d} \\ e^{-j\frac{2\pi\Delta}{\lambda}8\cos\theta_1} & e^{-j\frac{2\pi\Delta}{\lambda}8\cos\theta_2} & \cdots & e^{-j\frac{2\pi\Delta}{\lambda}8\cos\theta_d} \\ e^{-j\frac{2\pi\Delta}{\lambda}9\cos\theta_1} & e^{-j\frac{2\pi\Delta}{\lambda}9\cos\theta_2} & \cdots & e^{-j\frac{2\pi\Delta}{\lambda}9\cos\theta_d} \\ e^{-j\frac{2\pi\Delta}{\lambda}(8\cos\theta_1+\sin\theta_1)} & e^{-j\frac{2\pi\Delta}{\lambda}(8\cos\theta_2+\sin\theta_2)} & \cdots & e^{-j\frac{2\pi\Delta}{\lambda}(8\cos\theta_d+\sin\theta_d)} \\ e^{-j\frac{2\pi\Delta}{\lambda}(8cos\theta_1-\sin\theta_1)} & e^{-j\frac{2\pi\Delta}{\lambda}(8\cos\theta_2-\sin\theta_2)} & \cdots & e^{-j\frac{2\pi\Delta}{\lambda}(8\cos\theta_d-\sin\theta_d)} \\ e^{-j\frac{2\pi\Delta}{\lambda}7\sin\theta_1} & e^{-j\frac{2\pi\Delta}{\lambda}7\sin\theta_2} & \cdots & e^{-j\frac{2\pi\Delta}{\lambda}7\sin\theta_d} \\ e^{-j\frac{2\pi\Delta}{\lambda}(\cos\theta_1+7\sin\theta_1)} & e^{-j\frac{2\pi\Delta}{\lambda}(\cos\theta_2+7\sin\theta_2)} & \cdots & e^{-j\frac{2\pi\Delta}{\lambda}(\cos\theta_d+7\sin\theta_d)} \\ e^{-j\frac{2\pi\Delta}{\lambda}(2\cos\theta_1+7\sin\theta_1)} & e^{-j\frac{2\pi\Delta}{\lambda}(2\cos\theta_2+7\sin\theta_2)} & \cdots & e^{-j\frac{2\pi\Delta}{\lambda}(2\cos\theta_d+7\sin\theta_d)} \\ e^{-j\frac{2\pi\Delta}{\lambda}(\cos\theta_1+8\sin\theta_1)} & e^{-j\frac{2\pi\Delta}{\lambda}(\cos\theta_2+8\sin\theta_2)} & \cdots & e^{-j\frac{2\pi\Delta}{\lambda}(\cos\theta_d+8\sin\theta_d)} \\ e^{-j\frac{2\pi\Delta}{\lambda}(\cos\theta_1+6\sin\theta_1)} & e^{-j\frac{2\pi\Delta}{\lambda}(\cos\theta_2+6\sin\theta_2)} & \cdots & e^{-j\frac{2\pi\Delta}{\lambda}(\cos\theta_d+6\sin\theta_d)} \end{bmatrix} \tag{3.2.9}$$

Square Cross Shaped Array Geometry

Finally, the array steering matrix for the square cross shaped array (SCSA) geometry (Fig. 3.2.d with $m = 20$) with the distance among the nodes equal to half-wavelength takes the form

$$\mathbf{A}_{SCSA}(\theta)=\begin{bmatrix}
0 & 0 & \cdots & 0\\
e^{-j\frac{2\pi\Delta}{\lambda}\cos\theta_1} & e^{-j\frac{2\pi\Delta}{\lambda}\cos\theta_2} & \cdots & e^{-j\frac{2\pi\Delta}{\lambda}\cos\theta_d}\\
e^{-j\frac{2\pi\Delta}{\lambda}2\cos\theta_1} & e^{-j\frac{2\pi\Delta}{\lambda}2\cos\theta_2} & \cdots & e^{-j\frac{2\pi\Delta}{\lambda}2\cos\theta_d}\\
e^{-j\frac{2\pi\Delta}{\lambda}(\cos\theta_1+\sin\theta_1)} & e^{-j\frac{2\pi\Delta}{\lambda}(\cos\theta_2+\sin\theta_2)} & \cdots & e^{-j\frac{2\pi\Delta}{\lambda}(\cos\theta_d+\sin\theta_d)}\\
e^{-j\frac{2\pi\Delta}{\lambda}(\cos\theta_1-\sin\theta_1)} & e^{-j\frac{2\pi\Delta}{\lambda}(\cos\theta_2-\sin\theta_2)} & \cdots & e^{-j\frac{2\pi\Delta}{\lambda}(\cos\theta_d-\sin\theta_d)}\\
e^{-j\frac{2\pi\Delta}{\lambda}3\cos\theta_1} & e^{-j\frac{2\pi\Delta}{\lambda}3\cos\theta_2} & \cdots & e^{-j\frac{2\pi\Delta}{\lambda}3\cos\theta_d}\\
e^{-j\frac{2\pi\Delta}{\lambda}4\cos\theta_1} & e^{-j\frac{2\pi\Delta}{\lambda}4\cos\theta_2} & \cdots & e^{-j\frac{2\pi\Delta}{\lambda}4\cos\theta_d}\\
e^{-j\frac{2\pi\Delta}{\lambda}5\cos\theta_1} & e^{-j\frac{2\pi\Delta}{\lambda}5\cos\theta_2} & \cdots & e^{-j\frac{2\pi\Delta}{\lambda}5\cos\theta_d}\\
e^{-j\frac{2\pi\Delta}{\lambda}(4\cos\theta_1+\sin\theta_1)} & e^{-j\frac{2\pi\Delta}{\lambda}(4\cos\theta_2+\sin\theta_2)} & \cdots & e^{-j\frac{2\pi\Delta}{\lambda}(4\cos\theta_d+\sin\theta_d)}\\
e^{-j\frac{2\pi\Delta}{\lambda}(4cos\theta_1-\sin\theta_1)} & e^{-j\frac{2\pi\Delta}{\lambda}(4\cos\theta_2-\sin\theta_2)} & \cdots & e^{-j\frac{2\pi\Delta}{\lambda}(4\cos\theta_d-\sin\theta_d)}\\
e^{-j\frac{2\pi\Delta}{\lambda}3\sin\theta_1} & e^{-j\frac{2\pi\Delta}{\lambda}3\sin\theta_2} & \cdots & e^{-j\frac{2\pi\Delta}{\lambda}3\sin\theta_d}\\
e^{-j\frac{2\pi\Delta}{\lambda}(\cos\theta_1+3\sin\theta_1)} & e^{-j\frac{2\pi\Delta}{\lambda}(\cos\theta_2+3\sin\theta_2)} & \cdots & e^{-j\frac{2\pi\Delta}{\lambda}(\cos\theta_d+3\sin\theta_d)}\\
e^{-j\frac{2\pi\Delta}{\lambda}(2\cos\theta_1+3\sin\theta_1)} & e^{-j\frac{2\pi\Delta}{\lambda}(2\cos\theta_2+3\sin\theta_2)} & \cdots & e^{-j\frac{2\pi\Delta}{\lambda}(2\cos\theta_d+3\sin\theta_d)}\\
e^{-j\frac{2\pi\Delta}{\lambda}(\cos\theta_1+4\sin\theta_1)} & e^{-j\frac{2\pi\Delta}{\lambda}(\cos\theta_2+4\sin\theta_2)} & \cdots & e^{-j\frac{2\pi\Delta}{\lambda}(\cos\theta_d+4\sin\theta_d)}\\
e^{-j\frac{2\pi\Delta}{\lambda}(\cos\theta_1+2\sin\theta_1)} & e^{-j\frac{2\pi\Delta}{\lambda}(\cos\theta_2+2\sin\theta_2)} & \cdots & e^{-j\frac{2\pi\Delta}{\lambda}(\cos\theta_d+2\sin\theta_d)}\\
e^{-j\frac{2\pi\Delta}{\lambda}(3\cos\theta_1+3\sin\theta_1)} & e^{-j\frac{2\pi\Delta}{\lambda}(3\cos\theta_2+3\sin\theta_2)} & \cdots & e^{-j\frac{2\pi\Delta}{\lambda}(3\cos\theta_d+3\sin\theta_d)}\\
e^{-j\frac{2\pi\Delta}{\lambda}(4\cos\theta_1+3\sin\theta_1)} & e^{-j\frac{2\pi\Delta}{\lambda}(4\cos\theta_2+3\sin\theta_2)} & \cdots & e^{-j\frac{2\pi\Delta}{\lambda}(4\cos\theta_d+3\sin\theta_d)}\\
e^{-j\frac{2\pi\Delta}{\lambda}(5\cos\theta_1+3\sin\theta_1)} & e^{-j\frac{2\pi\Delta}{\lambda}(5\cos\theta_2+3\sin\theta_2)} & \cdots & e^{-j\frac{2\pi\Delta}{\lambda}(5\cos\theta_d+3\sin\theta_d)}\\
e^{-j\frac{2\pi\Delta}{\lambda}(4\cos\theta_1+4\sin\theta_1)} & e^{-j\frac{2\pi\Delta}{\lambda}(4\cos\theta_2+4\sin\theta_2)} & \cdots & e^{-j\frac{2\pi\Delta}{\lambda}(4\cos\theta_d+4\sin\theta_d)}\\
e^{-j\frac{2\pi\Delta}{\lambda}(4\cos\theta_1+2\sin\theta_1)} & e^{-j\frac{2\pi\Delta}{\lambda}(4\cos\theta_2+2\sin\theta_2)} & \cdots & e^{-j\frac{2\pi\Delta}{\lambda}(4\cos\theta_d+2\sin\theta_d)}
\end{bmatrix}\tag{3.2.10}$$

3.3 Numerical Examples and Simulation Results for Narrowband Sources

In this section a number of numerical examples are presented to demonstrated the performance of MUSIC algorithm using the array geometries presented above. In the simulation, 100 independent Monte Carlo runs are performed for each example and for each trial, the array output is observed for $N = 100$ independent snapshots. The array of sensors composed of two, three or four nodes is exposed to three coherent, non-coherent and partially coherent narrowband planar wavefronts arriving from 20, 25 and 30 degrees. The additive noise is independent zero mean Gaussian and the SNR is defined relative to each source. Moreover, beamforming technique is used on the simulated data to form the three initial azimuth angle estimates used by the MUSIC algorithm.

3.3.1 Performance Capabilities of the MUSIC Algorithm

In the first experiment, the performance capabilities of the MUSIC algorithm in the presence of coherent, non-coherent and partially coherent sources are studied. Two cross shaped arrays composed of $m = 10$ elements (5 elements for each node) with one half-wavelength element spacing is used and the array of sensors are exposed to the three narrowband planar wavefronts arriving from 20, 25 and 30 degrees where each narrowband signal is the sum of a set of cosine signals with random amplitude and the same center frequency $f_c = 1700Hz$. The results of the simulations for 100 independent trials are presented in Table 3.1. In order to obtain the probability of resolution, 100 independent trials are performed and the number of times that the method resolved the three DOAs is counted. It can be seen that the MUSIC algorithm could resolve 3 non-coherent and partially coherent sources while it failed to resolve coherent signals. In other words, for non-coherent and partially coherent signals, the MUSIC algorithm has a good performance but for the coherent signals the efficiency is very low even in higher SNR values. The pseudo spectrum of the MUSIC estimator in the presence of non-coherent, partially coherent and coherent signals is depicted in Fig 3.3.

To study the performance capabilities of the MUSIC algorithm in response to changing the number of sensors using different geometries in the presence of partially coherent

SNR (dB)	Probability of Resolution			
	3 non-coherent sources (source covariance matrix is diagonal)	3 partially coherent sources (source covariance matrix is non-diagonal and non-singular)	2 coherent and 1 non-coherent sources (source covariance matrix is singular)	3 coherent sources (source covariance matrix is singular)
0	0.00	0.00	could not resolve sources even for higher values of SNR	could not resolve sources even for higher values of SNR
5	0.00	0.00		
10	0.73	0.00		
15	0.95	0.65		
20	1.00	1.00		
25	1.00	1.00		

Table 3.1: Performance capabilities of the MUSIC algorithm in the presence of the coherent, non-coherent and partially coherent sources.

signals a second experiment is performed. The number of snapshots is $N = 100$, whereas the location of sources are 20, 25 and 30 degrees and the number of sensors are varied from $m = 10$ to $m = 20$. The geometry of array sensors is shown in Fig. 3.2 where the distance among the nodes is chosen to be half-wavelength. The results of the simulations for 100 independent trials are depicted in Fig. 3.4. It is observed that by increasing the number of sensors, the probability of resolution is improved for all the geometries. However, for $m = 10$ the linear cross shaped geometry has a lower resolving threshold than the diagonal cross shaped geometry while for $m = 15$ and $m = 20$ the triangular and square geometries have a better resolving threshold than the linear case. To show the effects of increasing the distance between the nodes, the experiments are repeated where the distance among the nodes is selected to be 10 half-wavelength. Fig. 3.5 depicts that the resolving threshold is significantly improved by increasing the distance among the nodes in different geometries. Again, for the triangular and square geometries the estimator has a lower resolving threshold than the linear case while for $m = 10$ the linear cross shaped geometry has a better resolving threshold than the diagonal cross shaped geometry. It is also seen that the resolving threshold for the case with $m = 10$, using 10

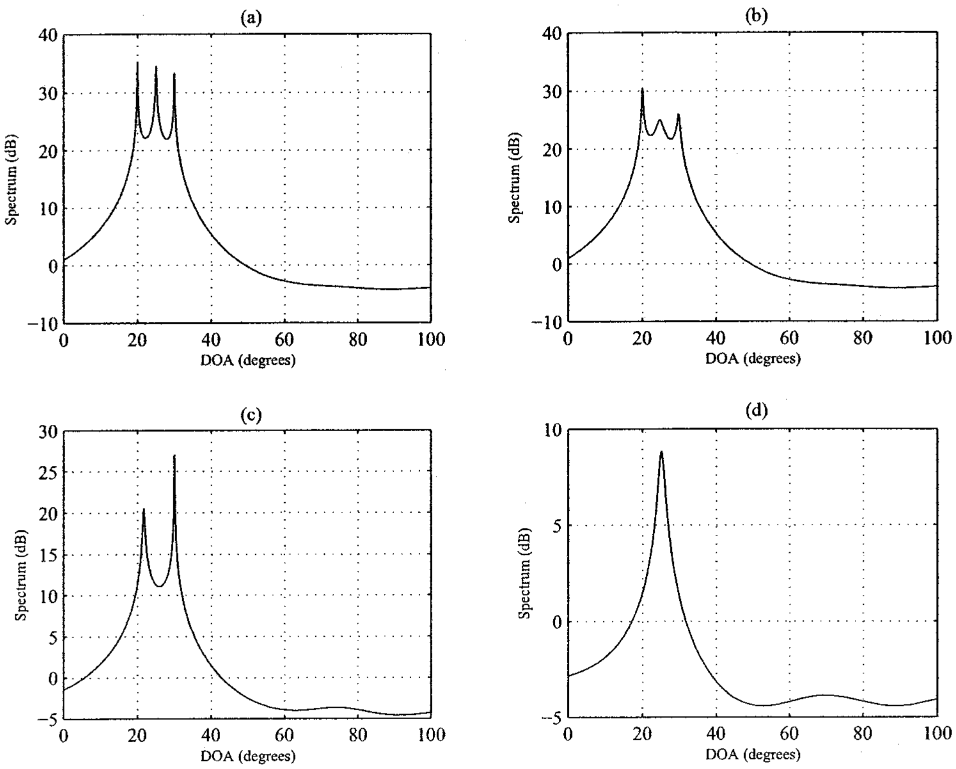

Figure 3.3: The pseudo spectrum of the MUSIC estimator using linear cross shaped geometry composed of two nodes in the presence of (a) Three non-coherent sources, (b) Three partially coherent sources, (c) Two coherent sources and one non-coherent source and (d) Three coherent sources. $SNR = 30dB$, $N = 100$, $m = 10$, DOA = [20 25 30] with the distance between the nodes is equal to one half-wavelength.

half-wavelength distance between two nodes, is lower than the case of $m = 20$ but with half-wavelength distance among the nodes.

The third example in this section is designed to demonstrate and illustrate the capability of the MUSIC estimator in resolving the closely spaced sources. For this example the three source signals are partially coherent and for each simulation their locations are chosen according to Table 3.2. The geometry of array sensors is the linear cross shaped where the number of sensors are varied from $m = 10$ to $m = 20$ with the distance between the two nodes is chosen to be 10 half-wavelength. The number of snapshots and

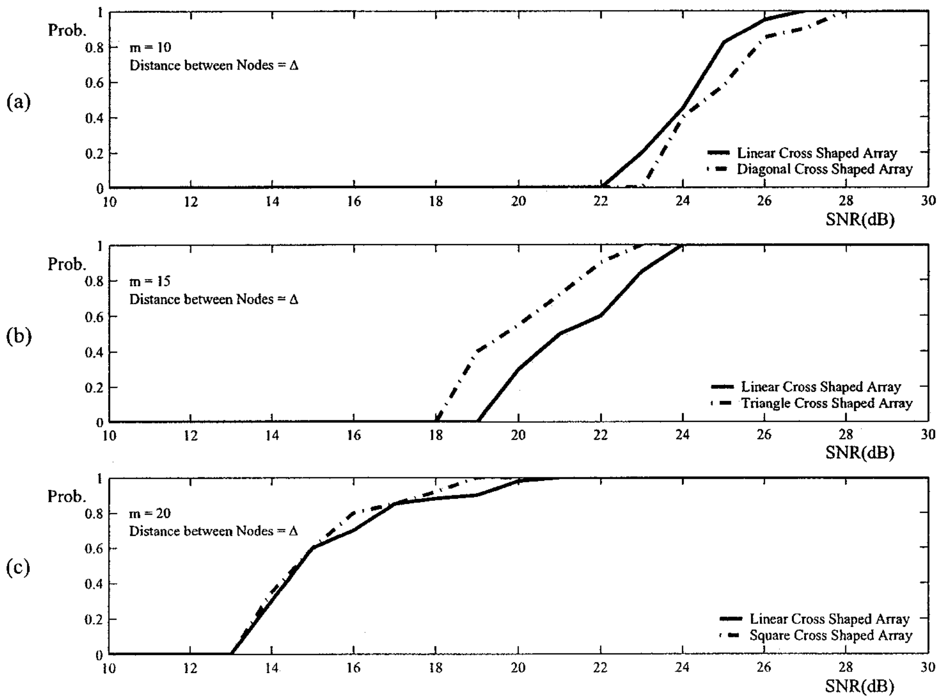

Figure 3.4: Probability of resolution (Prob. in above figures) versus the SNR for (a) $m = 10$, (b) $m = 15$ and (c) $m = 20$. The distance among the nodes is equal to one half-wavelength.

the distance among the nodes are 100 and 10 half-wavelength, respectively. The simulation results show that the resolution capability of this estimator improves by increasing the angle among the sources which is intuitively expected. Indeed, the threshold SNR is higher for locating the closely spaced sources. As seen in Fig. 3.6, the SNR threshold is decreased by increasing the number of sensors form $m = 10$ to $m = 20$.

The last and the most important experiment in this section is performed to show the effects of changing the distance between two nodes in the array sensors for resolving the sources using the MUSIC algorithm. In this example the number of snapshots is taken as $N = 100$ and the location of the sources are at 20, 25 and 30 degrees. The simulation results show that by increasing the distance between two nodes from Δ to 10Δ, the

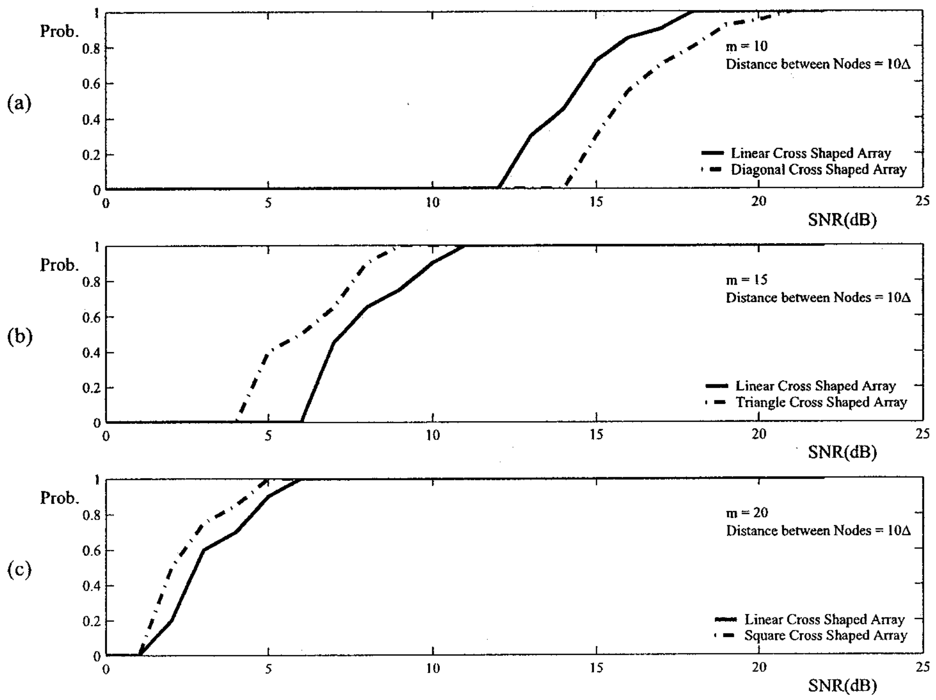

Figure 3.5: Probability of resolution (Prob. in above figures) versus the SNR for (a) $m = 10$, (b) $m = 15$ and (c) $m = 20$. The distance among the nodes is equal to 10 half-wavelength.

capability of the DOA estimator improves for resolving the sources, i.e. by increasing the distance between two nodes the SNR threshold is decreased (Fig. 3.7a). These results are confirmed by those obtained in Fig. 3.7b where the probability of resolution is improved by increasing the distance between two nodes. However, this improvement is achieved only for a few decades of Δ (almost 50Δ) and after that the capability of resolving the sources have again decreased.

To confirm the above results, another simulation scenario is designed. For this purpose, the norm of bias vector is measured versus the distance between the two nodes. As depicted in Fig. 3.8, the estimation error is decreased from Δ to 40Δ and has remained unchanged up to 65Δ and beyond this is then increased, so that the MUSIC

Angle between sources (deg)	Location of sources (deg)		
	θ_1	θ_2	θ_3
1	20	21	22
2	20	22	24
3	20	23	26
4	20	24	28
5	20	25	30
6	20	26	32
7	20	27	34
8	20	28	36
9	20	29	38
10	20	30	40

Table 3.2: The location of sources in Section 3.3.1.

DOA algorithm is not able to resolve the sources.

3.4 Coherent Signal Subspace Method using Cross Shaped Array Geometry

The main objective of the coherent signal subspace method (CSM) is to transform the signal subspaces of the narrowband components within the common bandwidth of the signals followed by an averaging of these aligned signal subspaces. In other words, the CSM algorithm transforms the steering matrices at different frequencies to a common frequency ω_0 (focusing frequency) using focusing matrices $\mathbf{T}_j$. As discussed in Chapter 2, theorem 2.3.1 conveys the basic concepts of the CSM algorithm for a general array geometry. It is clear that construction of $\mathbf{T}(\omega_\mathrm{j})$ requires a knowledge of the unknown DOAs. Therefore, the first step in estimating $\mathbf{T}(\omega_\mathrm{j})$ is to perform an initial estimate of the DOA angles. Using a classical beamforming gives an estimate of the angles of arrival which can be used in estimating $\mathbf{T}(\omega_\mathrm{j})$. Suppose all the true angles of arrival are within the neighborhood of the preliminary angle θ_0. Then the diagonal focusing matrices $\mathbf{T}(\omega_j)$ for $m = 10$ sensors can be estimated as

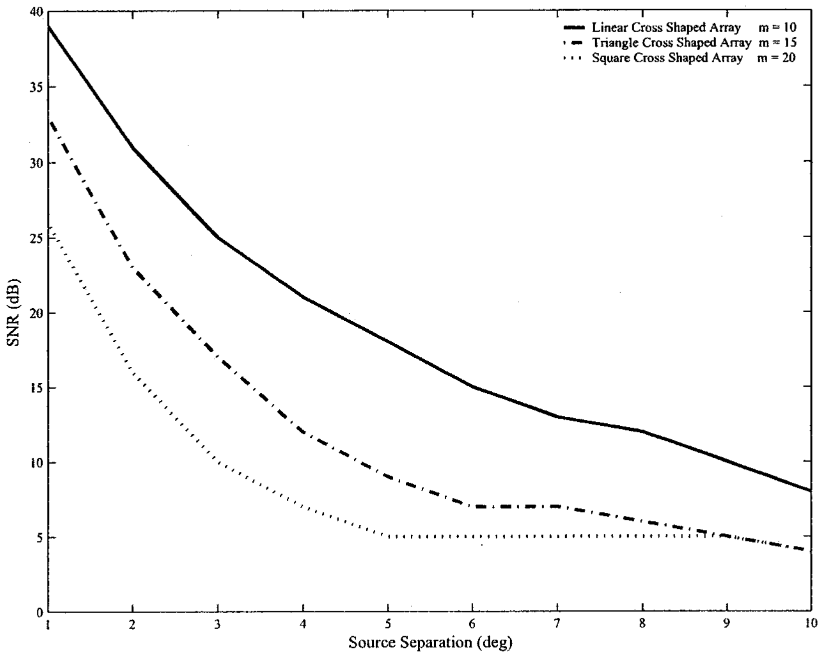

Figure 3.6: The minimum SNR required for the source separation using the MUSIC estimator. The locations of the sources are shown in Table 3.2 and the number of sensors are $m = 10$, $m = 15$ and $m = 20$.

$$\hat{\mathrm{T}}(\omega_j) = \begin{bmatrix} \frac{\mathrm{a}_1(\omega_0,\theta_0)}{\mathrm{a}_1(\omega_j,\theta_0)} & 0 & 0 & \cdots & 0 \\ 0 & \frac{\mathrm{a}_2(\omega_0,\theta_0)}{\mathrm{a}_2(\omega_j,\theta_0)} & \vdots & \vdots & \vdots \\ 0 & 0 & \ddots & 0 & 0 \\ \vdots & \vdots & \vdots & \frac{\mathrm{a}_9(\omega_0,\theta_0)}{\mathrm{a}_9(\omega_j,\theta_0)} & 0 \\ 0 & \cdots & 0 & 0 & \frac{\mathrm{a}_{10}(\omega_0,\theta_0)}{\mathrm{a}_{10}(\omega_j,\theta_0)} \end{bmatrix} \tag{3.4.1}$$

where $\mathrm{a}_l(\omega_j, \theta_0)$ for $1 \leq l \leq 10$ is the lth element of the steering vector $\mathbf{a}(\omega_\mathrm{j}, \theta_0)$. In the case of linear cross shaped array (LCSA) consisting of two nodes (Fig. 3.2.a with two nodes i.e. $m = 10$) with the distance between the nodes equal to half-wavelength (refer to (3.2.4) and (3.2.5)) the diagonal focusing matrices take the form

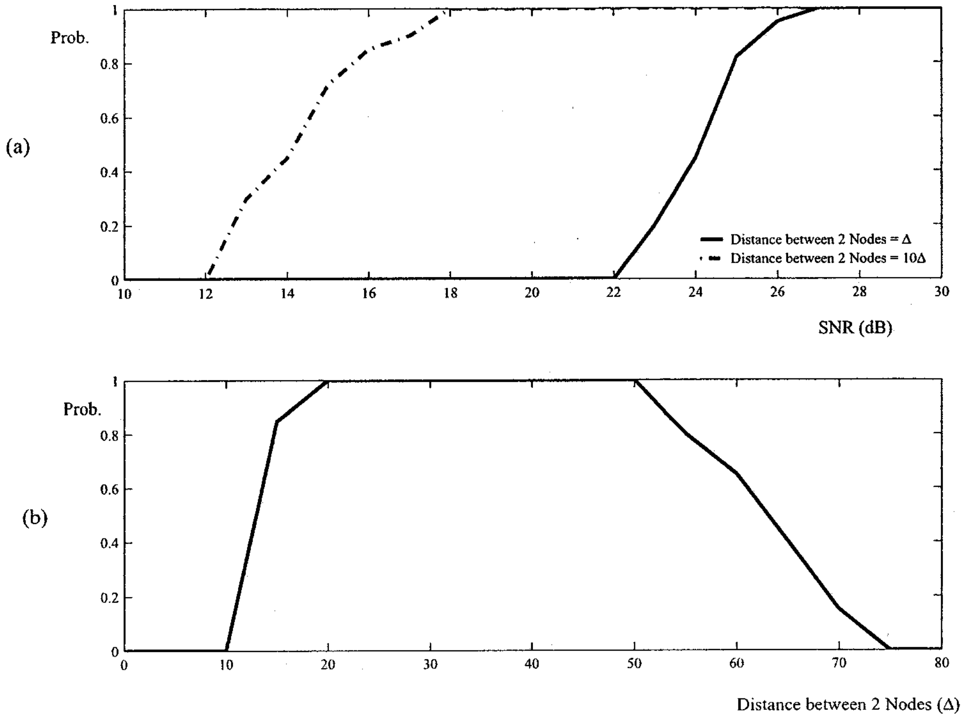

Figure 3.7: (a) Probability of resolution (Prob. in above figures) versus the SNR. The distances between the two nodes are equal to one half-wavelength and 10 half-wavelength. (b) Probability of resolution versus the distance between the two nodes ($m = 10$, $N = 100$, DOA = [20 25 30], $SNR = 10dB$).

$$\hat{\mathbf{T}}_{LCSA}(\omega_j) = \begin{bmatrix} e^{-j(\omega_0-\omega_j)\tau_1(\theta_0)} & 0 & 0 & \cdots & 0 \\ 0 & e^{-j(\omega_0-\omega_j)\tau_2(\theta_0)} & \vdots & \vdots & \vdots \\ 0 & 0 & \ddots & 0 & 0 \\ \vdots & \vdots & \vdots & e^{-j(\omega_0-\omega_j)\tau_9(\theta_0)} & 0 \\ 0 & \cdots & 0 & 0 & e^{-j(\omega_0-\omega_j)\tau_{10}(\theta_0)} \end{bmatrix} \tag{3.4.2}$$

where

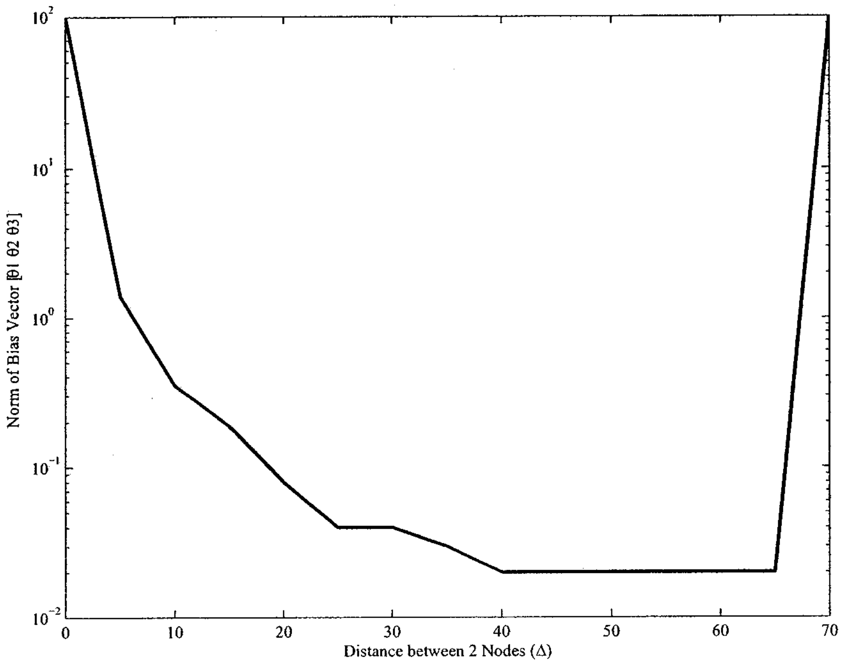

Figure 3.8: The norm of the bias vector versus distance between two nodes for the MUSIC algorithm ($m = 10$, $N = 100$, $SNR = 20dB$, DOA = [20 25 30]).

$$
\begin{aligned}
\tau_1(\theta_0) &= 0 & \tau_2(\theta_0) &= \frac{2\pi\Delta}{\lambda}\cos\theta_0 \\
\tau_3(\theta_0) &= \frac{2\pi\Delta}{\lambda}2\cos\theta_0 & \tau_4(\theta_0) &= \frac{2\pi\Delta}{\lambda}(\cos\theta_0 + \sin\theta_0) \\
\tau_5(\theta_0) &= \frac{2\pi\Delta}{\lambda}(\cos\theta_0 - \sin\theta_0) & \tau_6(\theta_0) &= \frac{2\pi\Delta}{\lambda}3\cos\theta_0 \\
\tau_7(\theta_0) &= \frac{2\pi\Delta}{\lambda}4\cos\theta_0 & \tau_8(\theta_0) &= \frac{2\pi\Delta}{\lambda}5\cos\theta_0 \\
\tau_9(\theta_0) &= \frac{2\pi\Delta}{\lambda}(4\cos\theta_0 + \sin\theta_0) & \tau_{10}(\theta_0) &= \frac{2\pi\Delta}{\lambda}(4\cos\theta_0 - \sin\theta_0)
\end{aligned}
$$

Furthermore, focusing matrices $\mathbf{T}(\omega_j)$ for the square cross shaped array (SCSA) geometry (Fig. 3.2.d with $m = 20$) with the distance among the nodes equal to half-wavelength take the form

$$\hat{\mathbf{T}}_{SCSA}(\omega_j) = \begin{bmatrix} e^{-j(\omega_0-\omega_j)\tau_1(\theta_0)} & 0 & 0 & \cdots & 0 \\ 0 & e^{-j(\omega_0-\omega_j)\tau_2(\theta_0)} & \vdots & \vdots & \vdots \\ 0 & 0 & \ddots & 0 & 0 \\ \vdots & \vdots & \vdots & e^{-j(\omega_0-\omega_j)\tau_{19}(\theta_0)} & 0 \\ 0 & \cdots & 0 & 0 & e^{-j(\omega_0-\omega_j)\tau_{20}(\theta_0)} \end{bmatrix} \tag{3.4.3}$$

where

$$\begin{aligned}
\tau_1(\theta_0) &= 0 & \tau_2(\theta_0) &= \frac{2\pi\Delta}{\lambda}\cos\theta_0 \\
\tau_3(\theta_0) &= \frac{2\pi\Delta}{\lambda}2\cos\theta_0 & \tau_4(\theta_0) &= \frac{2\pi\Delta}{\lambda}(\cos\theta_0+\sin\theta_0) \\
\tau_5(\theta_0) &= \frac{2\pi\Delta}{\lambda}(\cos\theta_0-\sin\theta_0) & \tau_6(\theta_0) &= \frac{2\pi\Delta}{\lambda}3\cos\theta_0 \\
\tau_7(\theta_0) &= \frac{2\pi\Delta}{\lambda}4\cos\theta_0 & \tau_8(\theta_0) &= \frac{2\pi\Delta}{\lambda}5\cos\theta_0 \\
\tau_9(\theta_0) &= \frac{2\pi\Delta}{\lambda}(4\cos\theta_0+\sin\theta_0) & \tau_{10}(\theta_0) &= \frac{2\pi\Delta}{\lambda}(4\cos\theta_0-\sin\theta_0) \\
\tau_{11}(\theta_0) &= \frac{2\pi\Delta}{\lambda}3\sin\theta_0 & \tau_{12}(\theta_0) &= \frac{2\pi\Delta}{\lambda}(\cos\theta_0+3\sin\theta_0) \\
\tau_{13}(\theta_0) &= \frac{2\pi\Delta}{\lambda}(2\cos\theta_0+3\sin\theta_0) & \tau_{14}(\theta_0) &= \frac{2\pi\Delta}{\lambda}(\cos\theta_0+4\sin\theta_0) \\
\tau_{15}(\theta_0) &= \frac{2\pi\Delta}{\lambda}(\cos\theta_0+2\sin\theta_0) & \tau_{16}(\theta_0) &= \frac{2\pi\Delta}{\lambda}(3\cos\theta_0+3\sin\theta_0) \\
\tau_{17}(\theta_0) &= \frac{2\pi\Delta}{\lambda}(4\cos\theta_0+3\sin\theta_0) & \tau_{18}(\theta_0) &= \frac{2\pi\Delta}{\lambda}(5\cos\theta_0+3\sin\theta_0) \\
\tau_{19}(\theta_0) &= \frac{2\pi\Delta}{\lambda}(4\cos\theta_0+4\sin\theta_0) & \tau_{20}(\theta_0) &= \frac{2\pi\Delta}{\lambda}(4\cos\theta_0+2\sin\theta_0)
\end{aligned}$$

It should be noted that extraction of focusing matrices using the diagonal cross shaped array and the triangular cross shaped array is straightforward. In the next section, a number of numerical examples and simulation results using the four different types of array geometries for the wideband signals using MUSIC and CSM algorithms will be presented.

3.5 Numerical Examples and Simulation Results for Wideband Sources

In the following, a number of numerical examples are presented to demonstrated the performance capabilities of the CSM algorithm using the above discussed array geometries (in conjunction with using MUSIC algorithm as a narrowband estimator). In the simulations, 100 independent Monte Carlo runs are performed for each example. Two bandpass coherent sources incident on an array of sensors composed of two, three or four nodes are considered. Two incident plane waves are taken to have bearing angles at 45 and 50 degrees (unless otherwise explicitly stated) where each wideband signal is the sum of a set of cosine signals with random amplitude, the same center frequency $f_c = 100Hz$ and the same bandwidth $BW = 40Hz$. The array noise $n(t)$ is taken as a complex valued additive bandpass (the same passband as the signals) white Gaussian process whose components are statistically independent of the source signals. The array signal model (2.3.2) is then employed to generate data to be used in forming the array covariance matrix (2.3.19). The sensor signals are observed over a $T = 48sec$ time interval. These signals are then sampled at the rate of 80 samples/sec to give a total of $L = 3840$ samples for each array sensor. To approximate the underlying array covariance matrix, each data length is decomposed into $Q = 60$ non-overlapping segments each consisting of 64 samples, i.e., each segment has $\Delta T = \frac{T}{Q} = 0.8sec$. Using the relationship (2.3.19), an estimate of the array covariance matrix is made with $J = 33$ equal frequency intervals spaced across the passband. Therefore, the data (signal plus noise) consists of 60 snapshots for each of the

33 narrowband frequency components.

3.5.1 Focusing Frequency Selection using the CSM Algorithm

As mentioned in Section 2.3.3, minimizing the subspace fitting error is an appropriate criterion for the focusing frequency selection i.e., minimizing the Euclidean distance between the focusing steering matrix and the transformed steering matrix at each frequency bin gives the optimum focusing frequency. Furthermore, by using this focusing frequency the bias of the estimator is minimized and the resolution threshold of SNR is reduced. Therefore, in our simulation results we first attempt to find the optimum focusing frequency and also to study the bias of the CSM algorithm using this optimum frequency. Fig. 3.9a shows the norm of the bias vector versus the focusing frequency for two coherent wideband sources arriving at a linear cross shaped array composed of two nodes with 10 half-wavelength distance between the nodes. It is seen that the bias is minimized between 90 and 95 Hz, while the center frequency for this example is 100 Hz. It should be noted that the most accurate assignment of the focusing frequency is not obtained since the search test was done with frequency steps equal to $5Hz$. In order to assign the optimum focusing frequency, the singular value maximization criteria is used. Indeed for this purpose, the singular values of the focusing steering matrix $\mathbf{A}(\omega_0)$ are determined and then using the known structure of the steering matrix the focusing frequency ω_0 was found (refer to equations (2.3.39), (2.3.40) and (2.3.41)). Fig. 3.9b depicts the singular value maximization criteria versus the focusing frequency. Using this criteria, the optimum focusing frequency was obtained to be equal to 93.75 Hz.

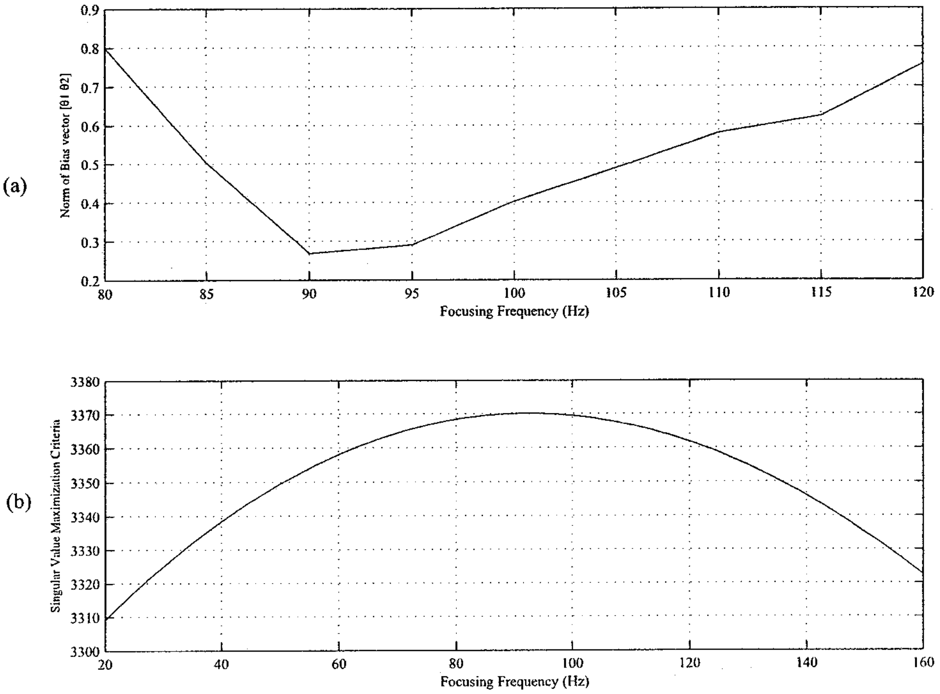

Figure 3.9: Focusing frequency selection a) The norm of the bias vector versus the focusing frequency for two coherent wideband sources arriving at a linear cross shaped array, b) Singular value maximization criteria versus the focusing frequency ($m = 10$, $SNR = 10dB$, DOA = [45 50] with distance between the two nodes = 10Δ).

3.5.2 Performance Capabilities of the CSM Algorithm

To study the performance capabilities of the CSM algorithm in response to changing the number of sensors using different geometries in the presence of wideband coherent sources this experiment is performed. The location of sources are 45 and 50 degrees and the number of sensors are varied from $m = 10$ to $m = 20$. The geometry of array sensors is shown in Fig. 3.2 where the distance among the nodes is chosen to be half-wavelength. The results of the simulation for 100 independent trials are depicted in Fig. 3.10. It is observed that by increasing the number of sensors, the probability of resolution has improved for all the geometries. As seen in Fig. 3.10, for all the cases the linear cross shaped geometry has the lowest resolving threshold as compared to the diagonal, triangular and square cross shaped geometries. To demonstrate the effects of increasing the distance among the nodes, the experiment is repeated where the distance among the nodes is selected to be 10 half-wavelength. Fig. 3.11 shows that the resolving threshold is significantly improved by increasing the distance among the nodes in different geometries. Again, for $m = 10$ and $m = 15$, the linear cross shaped geometry has the lowest resolving threshold as compared to the diagonal and triangular cross shaped geometries while for $m = 20$ the square cross shaped geometry had a better resolving threshold than the linear case. It is also seen that the resolving threshold for the case of $m = 10$ using 10 half-wavelength distance between two nodes is equal to the case of $m = 20$ but using half-wavelength distance among the nodes.

The above experiment has shown that a larger array aperture results in a lower resolving threshold and yields more accurate DOA estimates with more robust resolution of closely spaced sources but resulting in some ambiguous estimates of the DOAs. Fig. 3.12 shows this ambiguity for different array geometries. As depicted in this figure the ambiguity for the triangular and square cross shaped geometries is less than the linear case while the resolving threshold for linear case is much better than the two other geometries.

The second example is designed to demonstrate the capability of the CSM algorithm in resolving the closely spaced sources and also to illustrate the effects of increasing the number of nodes in the array geometry. For this example the two source signals are coherent and for each simulation their locations are chosen according to Table 3.3. The geometry of array sensors is the linear cross shaped where the number of sensors are

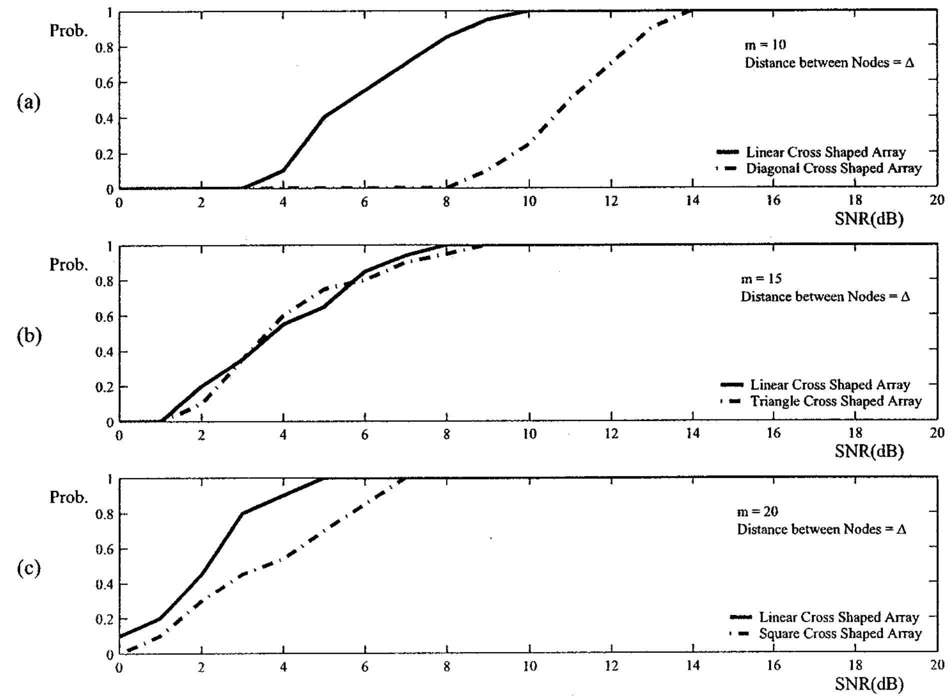

Figure 3.10: Resolution probability (Prob. in above figures) of the CSM algorithm (using the MUSIC algorithm as a narrowband estimator) versus the SNR for (a) $m = 10$, (b) $m = 15$ and (c) $m = 20$. The distance among the nodes is equal to one half-wavelength.

varied from $m = 10$ to $m = 20$ with the distance between the two nodes is chosen to be 10 half-wavelength. The simulation results show that the resolution capability of the DOA estimator is improved by increasing the angle among the sources which is intuitively expected. Indeed, the threshold SNR is higher for locating the closely spaced sources. Furthermore, as depicted in Fig. 3.13, the SNR threshold is decreased by increasing the number of nodes in the array geometry from 2 cross shaped nodes to 4 cross shaped nodes.

The third example in this section is conducted to study the capability of the CSM algorithm in resolving the coherent wideband sources by changing the number of nodes in the array sensors and the signal to noise ratios. Table 3.4 shows the minimum number of sensors that are required to resolve 2, 3 and 5 coherent wideband sources for a fixed value

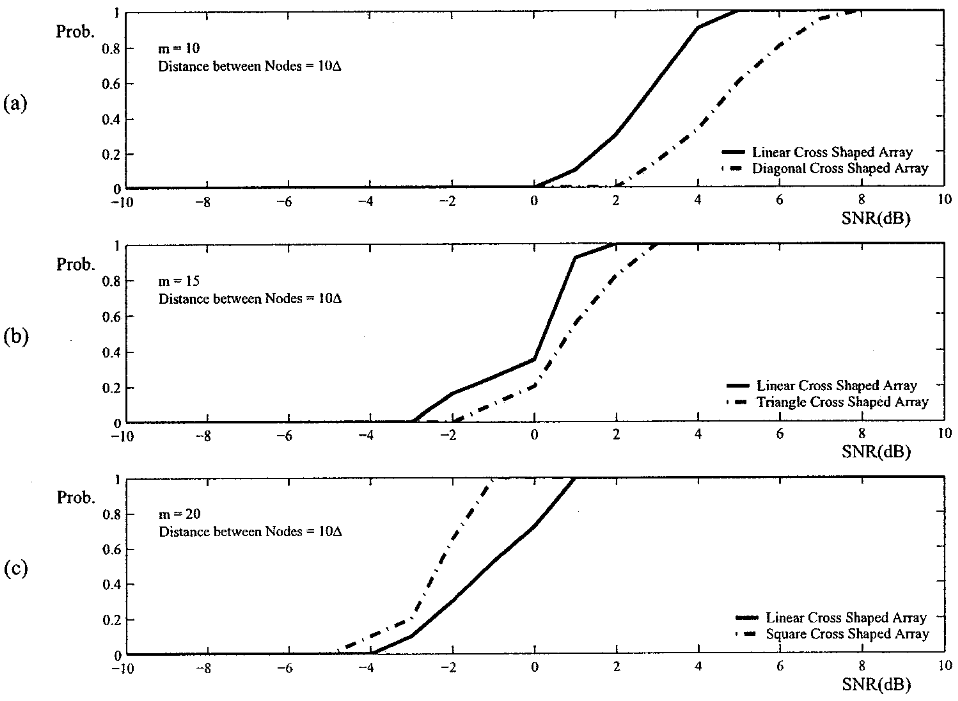

Figure 3.11: Resolution probability (Prob. in above figures) of the CSM algorithm (using the MUSIC algorithm as a narrowband estimator) versus the SNR for (a) $m = 10$, (b) $m = 15$ and (c) $m = 20$. The distance among the nodes is equal to 10 half-wavelength.

of $SNR = 10dB$ with the distance among the nodes being equal to 10Δ. The minimum values of SNR required for resolving 2, 3, 4 and 5 coherent wideband sources using linear cross shaped array composed of 10 sensors with 10 half-wavelength spacing between two nodes are shown in Table 3.5.

To demonstrate the performance of the CSM algorithm in response to increasing the distance between the two nodes in the array sensors the next experiment is designed. As seen in the first example of the present section a larger array aperture causes a lower resolving threshold and produces more accurate DOA estimates and more robust resolution of closely spaced sources but it also results in ambiguous estimates of the DOA's. Fig. 3.14 to Fig. 3.18 show this ambiguity for a linear cross shaped array composed of two

Angle between sources (deg)	Location of sources (deg)	
	θ_1	θ_2
1	45	46
2	45	47
3	45	48
4	45	49
5	45	50
6	45	51
7	45	52
8	45	53
9	45	54
10	45	55

Table 3.3: The location of sources in Section 3.5.2.

The minimum number of sensors required	The number of sources that the CSM algorithm resolved
1 node (5 sensors)	2
2 nodes (10 sensors)	3
3 nodes (15 sensors)	5

Table 3.4: The minimum numbers of sensors required to resolve coherent wideband sources in Section 3.5.2.($SNR = 10dB$ with the distance among the nodes = 10Δ).

The minimum values of SNR(dB) required	The number of sources that the CSM algorithm resolved
5	2
12	3
17	4
24	5

Table 3.5: The minimum value of SNRs required to resolve coherent wideband sources in Section 3.5.2.($m = 10$ with the distance between two nodes = 10Δ).

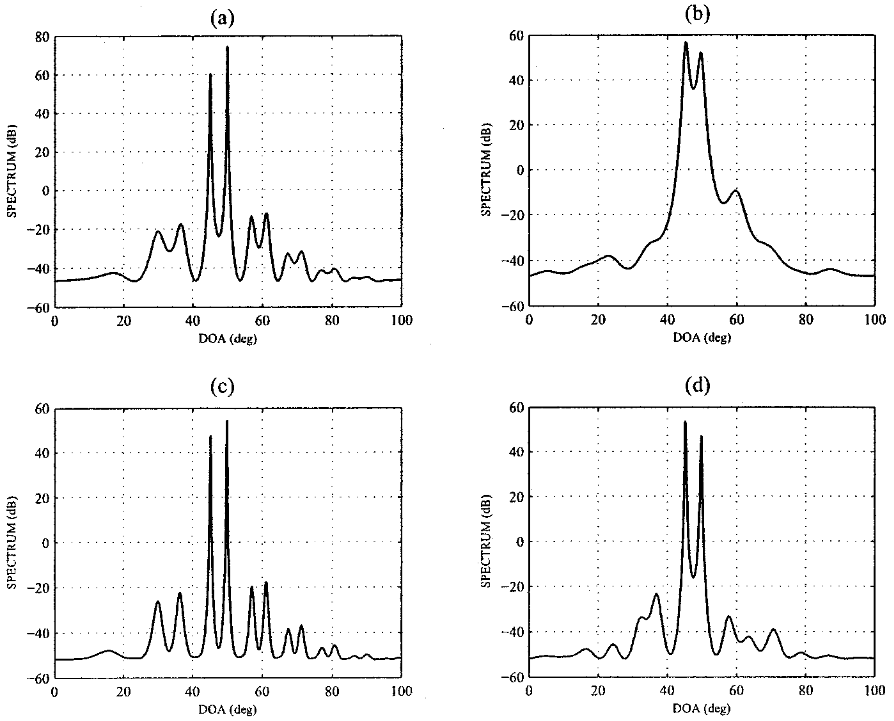

Figure 3.12: The pseudo spectrum of the MUSIC estimator in the presence of two wide-band coherent sources showing the ambiguous estimates for (a) Linear cross shaped array $m = 15$, (b) Triangular cross shaped array $m = 15$, (c) Linear cross shaped array $m = 20$ and (d) Square cross shaped array $m = 20$ with $SNR = 10dB$, DOA = [45 50] with distance among the nodes = 10Δ.

nodes where the distance between the nodes is changed from 5 to 60 half-wavelength with the step size equal to 5 half-wavelength and the SNR is varied from 0 to $20dB$ with the step size equal to $5dB$. As depicted in these figures this ambiguity is increased for larger array aperture while the resolving threshold is decreased. It should be noted that after 60Δ the estimation errors have increased so that the algorithm is not able to resolve the sources even for high SNR values.

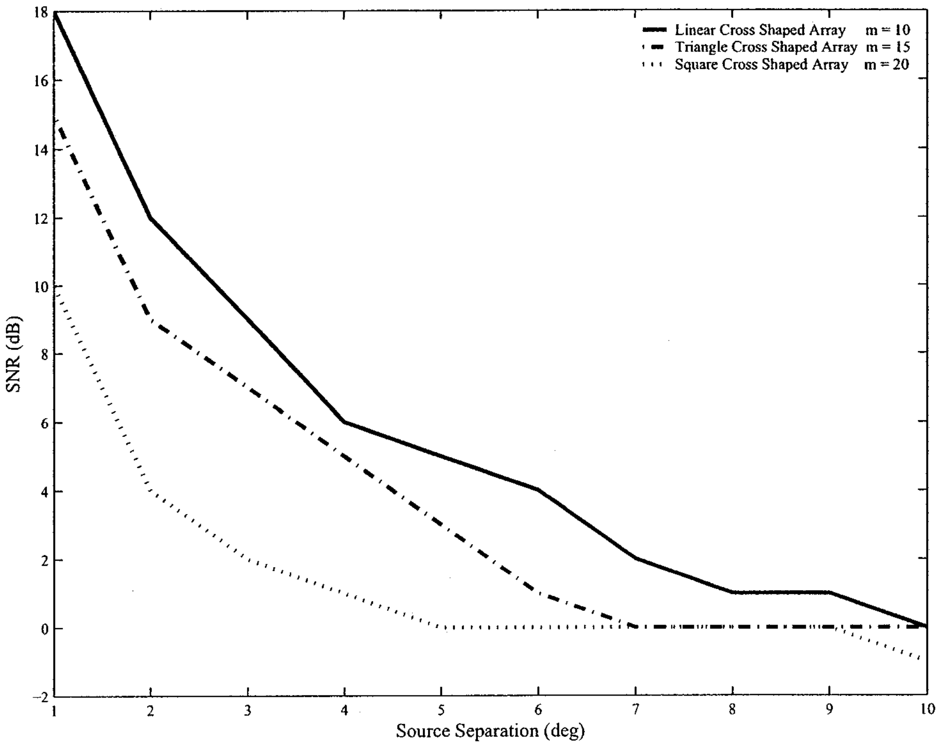

Figure 3.13: The minimum SNR required for the source separation in the CSM algorithm using MUSIC algorithm as a narrowband estimator. The locations of the sources are shown in Table 3.3 and the number of sensors are $m = 10$, $m = 15$ and $m = 20$.

3.5.3 Performance Comparison of the CSM Algorithm using the Diagonal and the Unitary Focusing Transformation Matrices

In this section, the performance capabilities of the CSM algorithm using the diagonal focusing transformation matrix and the unitary focusing transformation matrix is compared. As mentioned in Chapter 2, the CSM algorithm has the best performance if the mapping of the subspaces is performed through a unitary transformation. In fact, using the unitary focusing transformation matrix to align the steering matrices causes one to minimize the bias of the DOA estimates. Fig. 3.19a depicts the pseudo spectrum of the

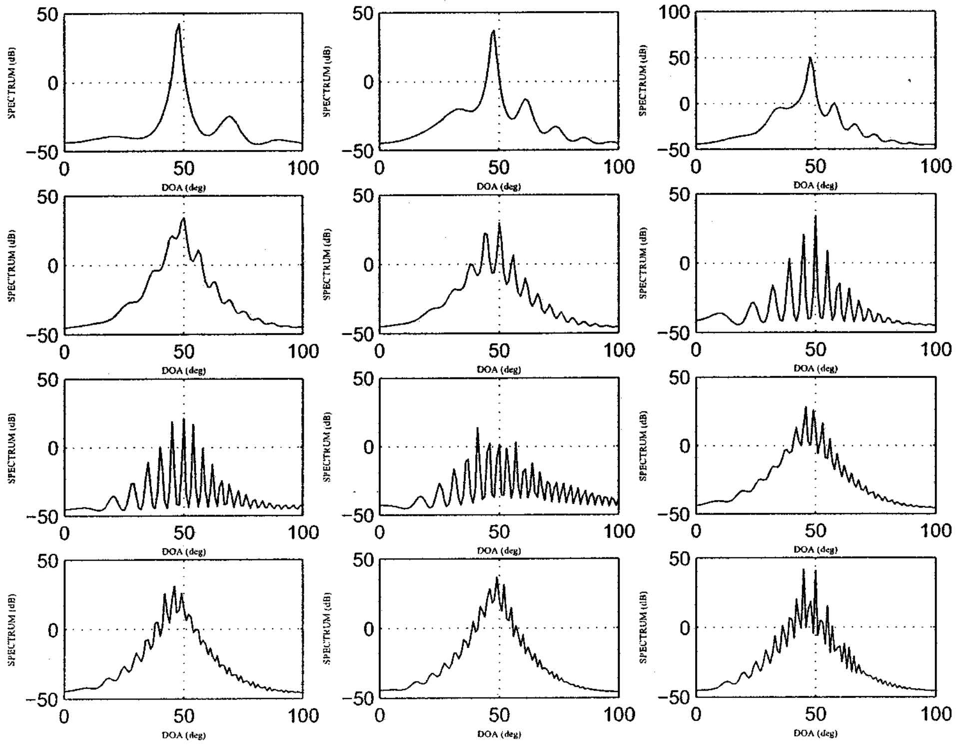

Figure 3.14: The pseudo spectrum of the MUSIC estimator in the presence of two wideband coherent sources showing the ambiguous estimates using the linear cross shaped array $m = 10$, $SNR = 0dB$, DOA = [45 50] and the distance between the two nodes is changed from 5 to 60 half-wavelength with the step size equal to 5Δ.

MUSIC estimator for the CSM using both diagonal and unitary matrices. As can be seen from this figure, both methods have some deviations form the true DOAs. To study this error, the norm of the bias vector as a function of SNR for both the diagonal and the unitary focusing transformation matrices is calculated and the results are shown in Fig. 3.19b. As can be observed from this figure the estimator error using the unitary focusing transformation matrix is lower than that of the diagonal case. Unfortunately, in spite of the fact that the CSM is very effective in wideband signal processing, it suffers from an asymptotic bias of the peaks as a result of the errors in estimated focusing subspaces. The bias increases with the bandwidth of the sources and the deviation of the focusing

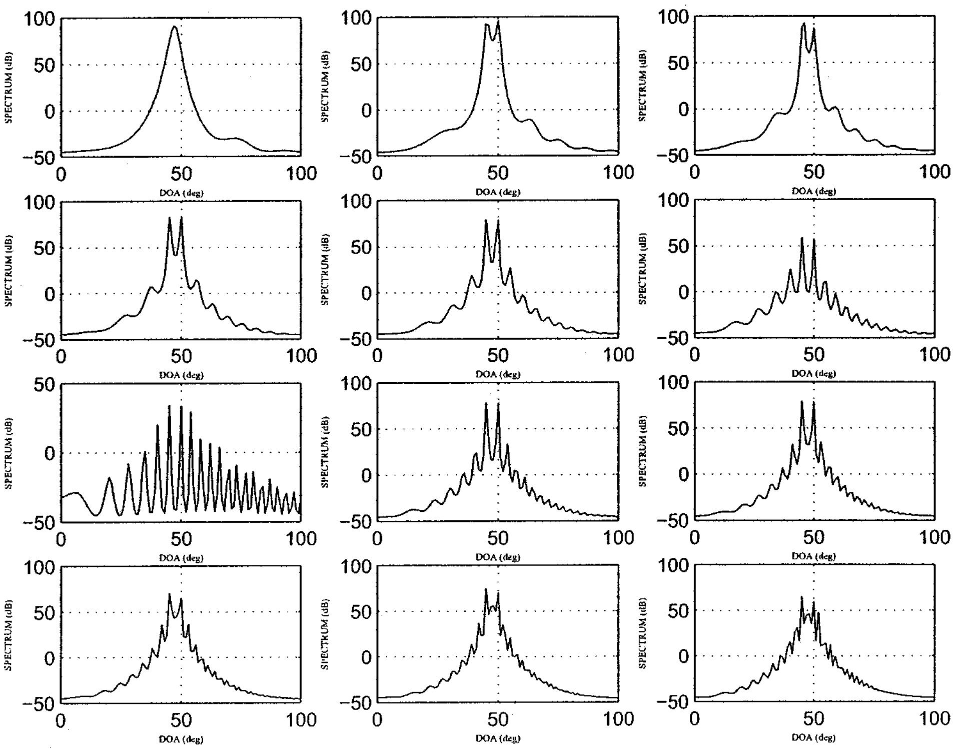

Figure 3.15: The pseudo spectrum of the MUSIC estimator in the presence of two wideband coherent sources showing the ambiguous estimates using the linear cross shaped array $m = 10$, $SNR = 5dB$, DOA = [45 50] and the distance between the two nodes is changed from 5 to 60 half-wavelength with the step size equal to 5Δ.

subspaces from the true subspaces. In this experiment the location of sources are 45 and 50 degrees and the geometry of array sensors is the linear cross shaped with $m = 10$ where the distance between the two nodes is chosen to be 10 half-wavelength.

3.6 Conclusion

Four different types of array geometries denoted as linear cross shaped array, diagonal cross shaped array, triangular cross shaped array and square cross shaped array are considered. As can be seen from the computer simulations both the node topology and the aperture are important parameters and the performance capabilities of both the narrowband and

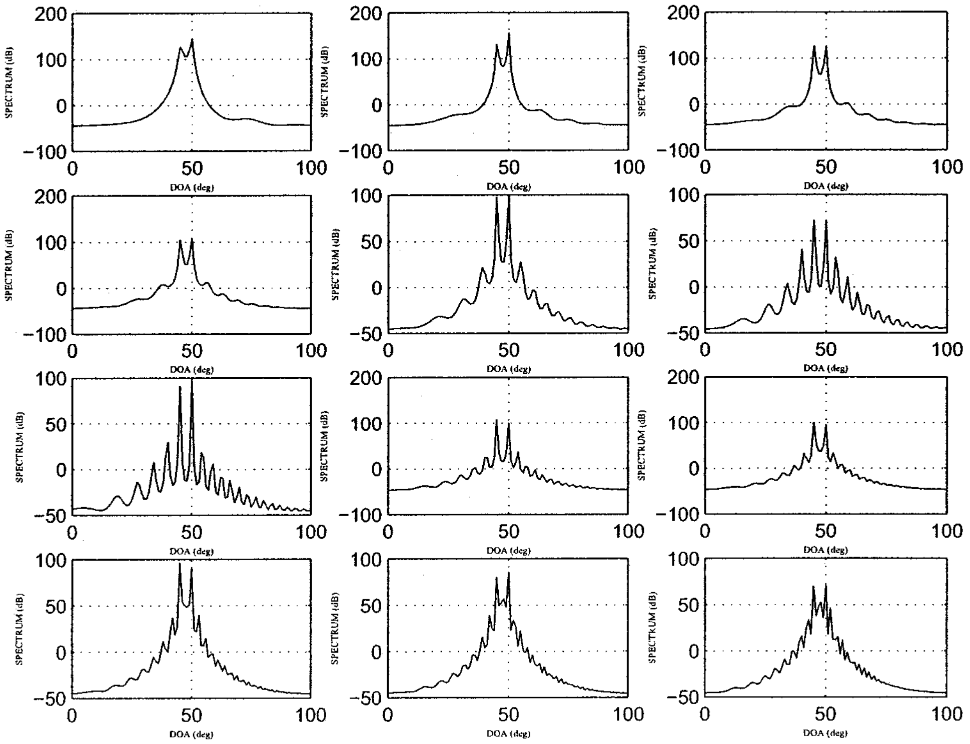

Figure 3.16: The pseudo spectrum of the MUSIC estimator in the presence of two wideband coherent sources showing the ambiguous estimates using the linear cross shaped array $m = 10$, $SNR = 10dB$, DOA = [45 50] and the distance between the two nodes is changed from 5 to 60 half-wavelength with the step size equal to 5Δ.

the wideband techniques are affected by adjusting these parameters. It is observed that by increasing the number of sensors and the distance among the nodes the probability of resolution is improved for all the geometries and it is also seen that the bias of estimator is decreased by increasing the above two mentioned parameters. Although a larger array aperture does result in a lower resolving threshold and produces more accurate DOA estimates but it also results in ambiguous estimates of the DOAs. As seen this ambiguity for the triangular and square cross shaped geometries is less than the linear case while the resolving threshold for the linear case is much better than the two other geometries.

The subspace fitting error criterion is used in the CSM algorithm for selection of the

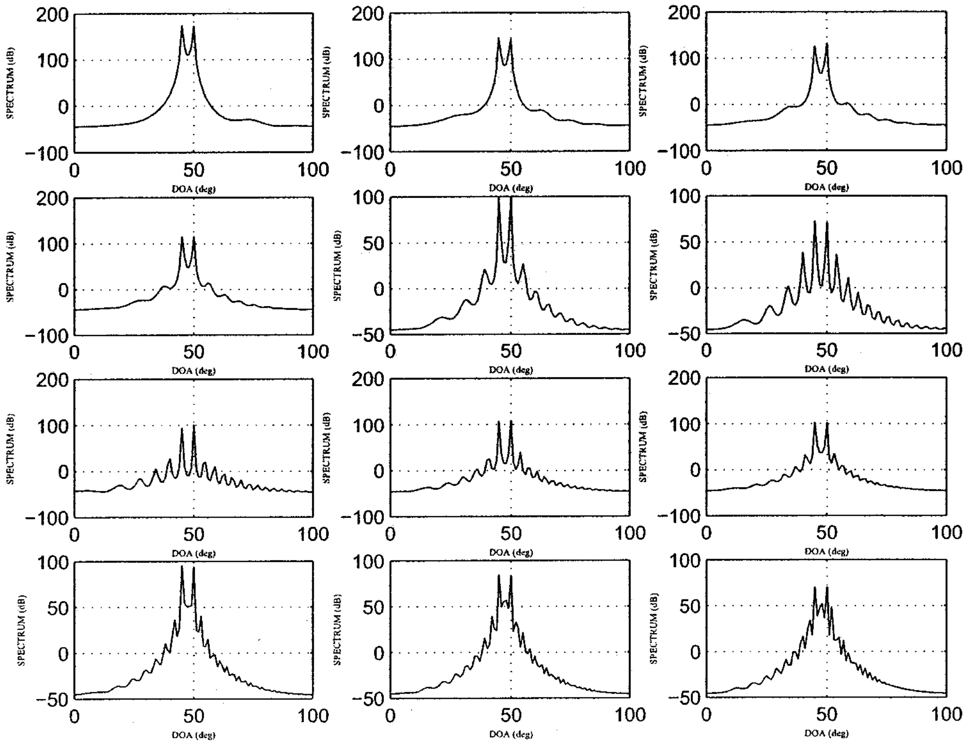

Figure 3.17: The pseudo spectrum of the MUSIC estimator in the presence of two wideband coherent sources showing the ambiguous estimates using the linear cross shaped array $m = 10$, $SNR = 15dB$, DOA = [45 50] and the distance between the two nodes is changed from 5 to 60 half-wavelength with the step size equal to 5Δ.

optimum focusing frequency. Using this optimum focusing frequency, it is observed that the bias of the estimator is minimized and the resolution threshold of the SNR is also reduced. Finally, the performance of the CSM algorithm using the diagonal focusing transformation matrix and the unitary focusing transformation matrix is considered. It can be observed that the DOA estimator error using the unitary focusing transformation matrix is lower than the one for the diagonal case.

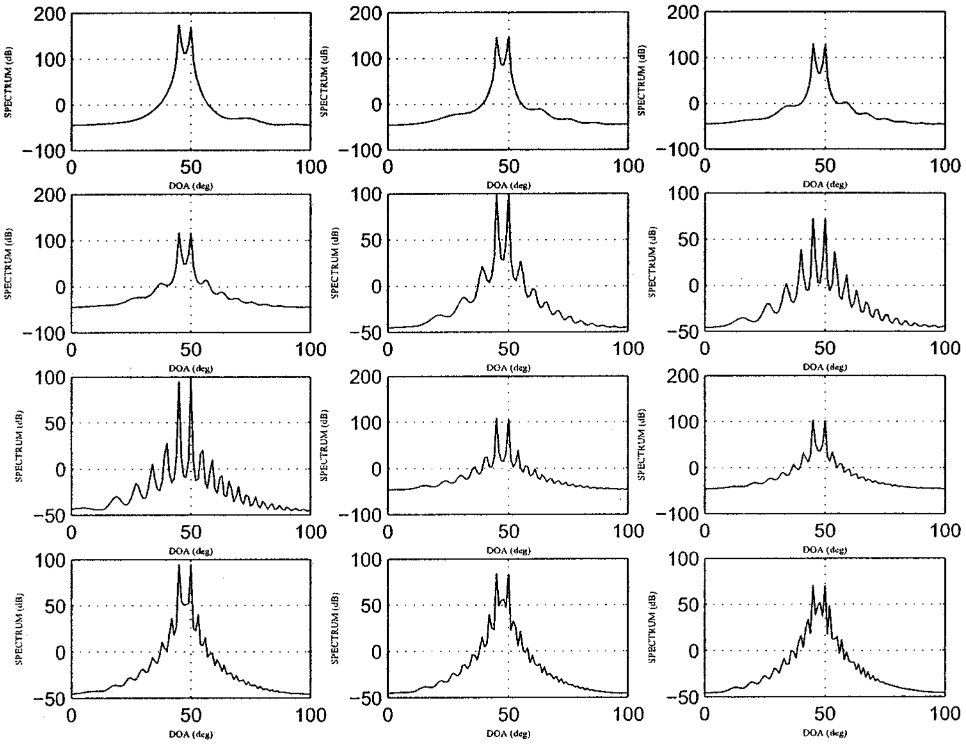

Figure 3.18: The pseudo spectrum of the MUSIC estimator in the presence of two wideband coherent sources showing the ambiguous estimates using the linear cross shaped array $m = 10$, $SNR = 20dB$, DOA = [45 50] and the distance between the two nodes is changed from 5 to 60 half-wavelength with the step size equal to 5Δ.

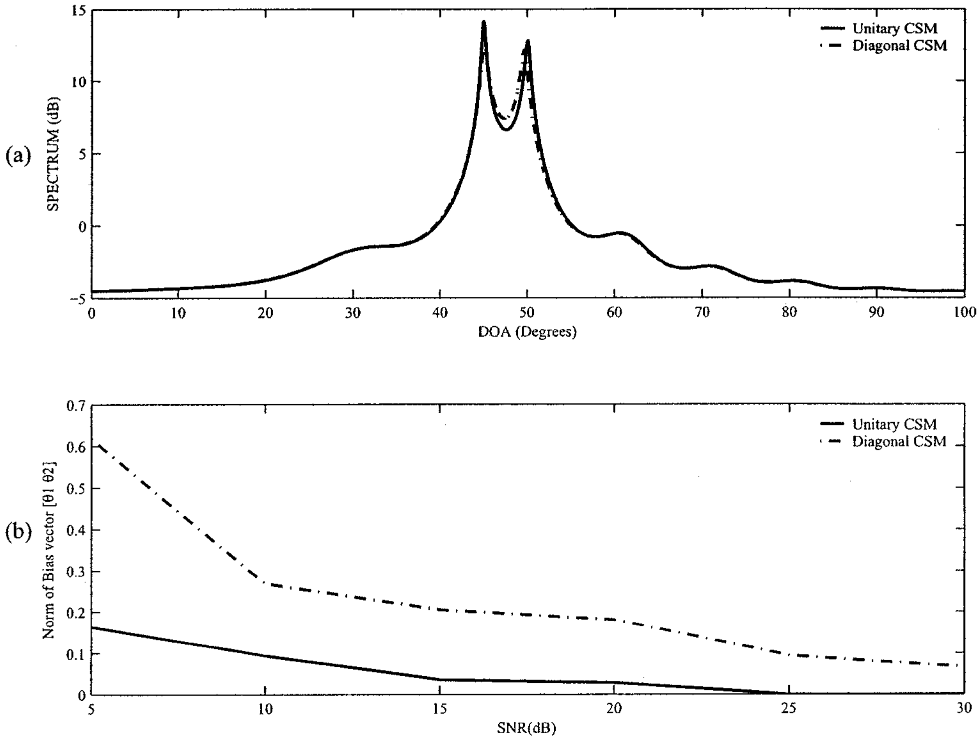

Figure 3.19: Performance of CSM algorithm using diagonal and unitary focusing transformation matrices in the presence of two wideband coherent sources a) The pseudo spectrum of the MUSIC estimator, b) The norm of bias vector versus SNR ($m = 10$, $SNR = 10dB$, DOA = [45 50] with the distance between two nodes = 10Δ).

Chapter 4

Development of Wideband Methods to Specific Geometries of Sensors using the WSF Algorithm

4.1 Introduction

As discussed in chapter 2, in spite of the MUSIC ability to resolve relatively closely spaced sources, this algorithm fails to produce peaks associated with true DOAs in small samples and at low SNRs, specially, in the presence of coherent sources. In the case of coherent sources, the orthogonal property of signal and noise subspaces is violated and the MUSIC algorithm fails to provide consistent estimates. In other words, the MUSIC algorithm usually suffers from a large finite sample bias in the presence of coherent sources which results in resolution problems. For these reasons, the weighted subspace fitting (WSF) method that was discussed in Chapter 2 for its relatively perfect performance is utilized to yield consistent estimates for the coherent sources. As we will see in the following sections the WSF algorithm has an excellent performance capabilities in the presence of coherent sources. This chapter attempts to show the ability of the WSF estimation algorithm in resolving closely spaced sources in the presence of coherent signals for both narrowband and wideband sources using the array geometries discussed in Chapter 3 (Fig. 3.2).

4.2 Coherent Signal Subspace Method using WSF algorithm

In this section, we will develop the narrowband WSF algorithm to the framework of the coherent signal subspace method discussed in Chapter 2 using cross shaped array geometry discussed previously.

Consider a linear cross shaped array consisting of two nodes (Fig. 3.2.a with two nodes i.e. $m = 10$) with the distance between the nodes equal to half-wavelength receiving d wideband sources. The locations of the sensors in the xy-plane are defined according to equation (3.2.4). The wideband sources are bandlimited to a common frequency band with a certain bandwidth. The array noise $n(t)$ is taken as a zero mean complex gaussian random process (the same passband as the signals) whose components are statistically independent of the source signals. Moreover, the signals of the sources can be non-coherent, and partially or fully coherent. As demonstrated in Chapter 2 the general wideband model is defined by

$$\mathbf{x}(\omega) = \mathbf{A}(\omega, \theta)\mathbf{s}(\omega) + \mathbf{n}(\omega) \tag{4.2.1}$$

where $\mathbf{x}(\omega)$ is the $m \times 1$ spectral array output vector, $\mathbf{A}(\omega, \theta)$ denotes the $m \times d$ steering matrix, $\mathbf{s}(\omega)$ is the $d \times 1$ spectral source vector and $\mathbf{n}(\omega)$ denotes the $m \times 1$ noise vector so that

$$\mathbf{x}(\omega) = [\mathrm{X}_1(\omega)\ \mathrm{X}_2(\omega)\ \ldots\ \mathrm{X}_m(\omega)]^T \tag{4.2.2}$$

$$\mathbf{s}(\omega) = [\mathrm{S}_1(\omega)e^{j\phi_1}\ \mathrm{S}_2(\omega)e^{j\phi_2}\ \ldots\ \mathrm{S}_d(\omega)e^{j\phi_d}]^T \tag{4.2.3}$$

$$\mathbf{n}(\omega) = [\mathrm{N}_1(\omega)\ \mathrm{N}_2(\omega)\ \ldots\ \mathrm{N}_m(\omega)]^T \tag{4.2.4}$$

and (refer to section 3.2)

$$\mathbf{A}(\omega,\theta) = \begin{bmatrix} 0 & \cdots & 0 \\ e^{-j(\omega-\omega_c)\frac{2\pi\Delta}{\lambda}\cos\theta_1} & \cdots & e^{-j(\omega-\omega_c)\frac{2\pi\Delta}{\lambda}\cos\theta_d} \\ e^{-j(\omega-\omega_c)\frac{2\pi\Delta}{\lambda}2\cos\theta_1} & \cdots & e^{-j(\omega-\omega_c)\frac{2\pi\Delta}{\lambda}2\cos\theta_d} \\ e^{-j(\omega-\omega_c)\frac{2\pi\Delta}{\lambda}(\cos\theta_1+\sin\theta_1)} & \cdots & e^{-j(\omega-\omega_c)\frac{2\pi\Delta}{\lambda}(\cos\theta_d+\sin\theta_d)} \\ e^{-j(\omega-\omega_c)\frac{2\pi\Delta}{\lambda}(\cos\theta_1-\sin\theta_1)} & \cdots & e^{-j(\omega-\omega_c)\frac{2\pi\Delta}{\lambda}(\cos\theta_d-\sin\theta_d)} \\ e^{-j(\omega-\omega_c)\frac{2\pi\Delta}{\lambda}3\cos\theta_1} & \cdots & e^{-j(\omega-\omega_c)\frac{2\pi\Delta}{\lambda}3\cos\theta_d} \\ e^{-j(\omega-\omega_c)\frac{2\pi\Delta}{\lambda}4\cos\theta_1} & \cdots & e^{-j(\omega-\omega_c)\frac{2\pi\Delta}{\lambda}4\cos\theta_d} \\ e^{-j(\omega-\omega_c)\frac{2\pi\Delta}{\lambda}5\cos\theta_1} & \cdots & e^{-j(\omega-\omega_c)\frac{2\pi\Delta}{\lambda}5\cos\theta_d} \\ e^{-j(\omega-\omega_c)\frac{2\pi\Delta}{\lambda}(4\cos\theta_1+\sin\theta_1)} & \cdots & e^{-j(\omega-\omega_c)\frac{2\pi\Delta}{\lambda}(4\cos\theta_d+\sin\theta_d)} \\ e^{-j(\omega-\omega_c)\frac{2\pi\Delta}{\lambda}(4cos\theta_1-\sin\theta_1)} & \cdots & e^{-j(\omega-\omega_c)\frac{2\pi\Delta}{\lambda}(4\cos\theta_d-\sin\theta_d)} \end{bmatrix} \tag{4.2.5}$$

where the lower bold face and upper bold face are used to designate the vector and matrix quantities, respectively. It is assumed that the number of sensors m is larger than the number of sources d and that the rank of $\mathbf{A}(\omega,\theta)$ is equal to d for any frequency and angle of arrival.

Using the results of section 2.3.1 the covariance matrix can be estimated by

$$\hat{\mathbf{R}}_x(\omega_j) \approx \frac{1}{Q}\sum_{q=1}^{Q}\mathbf{x}_q(\omega_j)\mathbf{x}_q^H(\omega_j) \quad \text{for} \quad 1 \le j \le J \tag{4.2.6}$$

where J is the number of frequency bins to be considered, Q is the number of subinterval, and ω_j is the frequency within the bandwidth. The coherent signal subspace algorithm transforms the observation vector at different frequency bins into the focusing subspace through the focusing matrices $\hat{\mathbf{T}}_{LCSA}(\omega_j)$ which is defined by (refer to equation (3.4.2))

$$\hat{\mathbf{T}}_{LCSA}(\omega_j) = \begin{bmatrix} e^{-j(\omega_0-\omega_j)\tau_1(\theta_0)} & 0 & 0 & \cdots & 0 \\ 0 & e^{-j(\omega_0-\omega_j)\tau_2(\theta_0)} & \vdots & \vdots & \vdots \\ 0 & 0 & \ddots & 0 & 0 \\ \vdots & \vdots & \vdots & e^{-j(\omega_0-\omega_j)\tau_9(\theta_0)} & 0 \\ 0 & \cdots & 0 & 0 & e^{-j(\omega_0-\omega_j)\tau_{10}(\theta_0)} \end{bmatrix} \tag{4.2.7}$$

where

$$
\begin{aligned}
\tau_1(\theta_0) &= 0 & \tau_2(\theta_0) &= \frac{2\pi\Delta}{\lambda}\cos\theta_0 \\
\tau_3(\theta_0) &= \frac{2\pi\Delta}{\lambda}2\cos\theta_0 & \tau_4(\theta_0) &= \frac{2\pi\Delta}{\lambda}(\cos\theta_0 + \sin\theta_0) \\
\tau_5(\theta_0) &= \frac{2\pi\Delta}{\lambda}(\cos\theta_0 - \sin\theta_0) & \tau_6(\theta_0) &= \frac{2\pi\Delta}{\lambda}3\cos\theta_0 \\
\tau_7(\theta_0) &= \frac{2\pi\Delta}{\lambda}4\cos\theta_0 & \tau_8(\theta_0) &= \frac{2\pi\Delta}{\lambda}5\cos\theta_0 \\
\tau_9(\theta_0) &= \frac{2\pi\Delta}{\lambda}(4\cos\theta_0 + \sin\theta_0) & \tau_{10}(\theta_0) &= \frac{2\pi\Delta}{\lambda}(4\cos\theta_0 - \sin\theta_0)
\end{aligned}
$$

Using these focusing matrices gives the universal focused covariance matrix $\hat{\mathbf{R}}$ (see equations (2.3.25) - (2.3.30))

$$
\begin{aligned}
\hat{\mathbf{R}} &= \sum_{j=1}^{J} \mathrm{w}_j \hat{\mathbf{T}}(\omega_j) E\{\mathbf{x}(\omega_j)\mathbf{x}^H(\omega_j)\}\hat{\mathbf{T}}^H(\omega_j) \\
&= \mathbf{A}(\omega_0)\hat{\mathbf{R}}_s\mathbf{A}^H(\omega_0) + \sigma_n^2\hat{\mathbf{R}}_n \qquad (4.2.8)
\end{aligned}
$$

where

$$
\hat{\mathbf{R}}_s = \sum_{j=1}^{J} \mathrm{w}_j \mathbf{P}_s(\omega_j) \qquad (4.2.9)
$$

and

$$
\hat{\mathbf{R}}_n = \sum_{j=1}^{J} \mathrm{w}_j \hat{\mathbf{T}}(\omega_j)\mathbf{P}_n(\omega_j)\hat{\mathbf{T}}^H(\omega_j) \qquad (4.2.10)
$$

Subsequently, the narrowband weighted subspace fitting algorithm discussed in Chapter 2 can be applied to this focused covariance matrix to obtain the DOA estimates.

4.3 Numerical Examples and Simulation Results for Narrowband Sources

In this section a number of numerical examples are presented to investigate the performance of the WSF algorithm using the various array geometries discussed previously.

Again, in the computer simulations 100 independent Monte Carlo runs are performed for each example and for each trial the array output is observed for $N = 100$ independent snapshots. The array of sensors are composed of two, three or four nodes that are exposed to three coherent, non-coherent and partially coherent narrowband planar wavefronts arriving from 20, 25 and 30 degrees where each narrowband signal is the sum of a set of cosine signals with random amplitude and the same center frequency $f_c = 1700Hz$. The additive noise is independent zero mean Gaussian and the SNR is defined relative to each source. Moreover, the alternating projection (AP) algorithm was used on the simulated data to form the three initial azimuth angle estimates.

4.3.1 Performance Capabilities of the WSF Algorithm

In the first example, the performance capabilities of the WSF algorithm in the presence of coherent, non-coherent and partially coherent sources are studied. Two cross shaped arrays composed of $m = 10$ elements (5 elements for each node) with one half-wavelength element spacing is used and the array of sensors are exposed to the three narrowband planar wavefronts arriving from 20, 25 and 30 degrees. The results of the simulations for 100 independent trials are presented in Table 4.1. In order to obtain the probability of resolution, 100 independent trials are performed and the number of times that the method resolved the three DOAs is counted. It can be seen that the WSF algorithm could resolve coherent, non-coherent and partially coherent sources and has a good performance for all the cases.

In the second experiment we study the performance capabilities of the WSF algorithm as a function of the changes in the number of sensors for different geometries and in the

S N R (dB)	Probability of Resolution			
	3 non-coherent sources (source covariance matrix is diagonal)	3 partially coherent sources (source covariance matrix is non-diagonal and non-singular)	2 coherent and 1 non-coherent sources (source covariance matrix is singular)	3 coherent sources (source covariance matrix is singular)
0	0.00	0.00	0.00	0.00
5	0.55	0.25	0.10	0.00
10	1.00	1.00	0.42	0.00
15	1.00	1.00	1.00	0.25
20	1.00	1.00	1.00	0.65
25	1.00	1.00	1.00	1.00

Table 4.1: Performance capabilities of the WSF algorithm in the presence of the coherent, non-coherent and partially coherent sources.

presence of partially coherent signals. The number of snapshots is taken as $N = 100$ and the location of the sources are at 20, 25 and 30 degrees with the number of sensors varied from $m = 10$ to $m = 20$. The geometries of array sensors consider are shown in Fig. 3.2 where the distance among the nodes is chosen to be half-wavelength. The results of the simulations for 100 independent trials are depicted in Fig. 4.1. It is observed that by increasing the number of sensors the probability of resolution has improved for all the geometries. However, the linear cross shaped and the diagonal cross shaped geometries for $m = 10$ and the linear cross shaped and the square cross shaped geometries for $m = 20$ have almost the same resolving threshold while for $m = 15$ the triangular cross shaped has a better resolving threshold than the linear geometry. To show the effects of increasing the distance among the nodes, we repeat this experiment where the distance among the nodes is selected to be 10 half-wavelength. Fig. 4.2 shows that the resolving threshold is significantly improved by increasing the distance among the nodes for the different geometries. In this scenario, for $m = 15$ and the triangular geometry the DOA estimator has a lower resolving threshold than the linear case while for $m = 10$ and $m = 20$ the linear geometry has a better resolving threshold than the diagonal and the square cross

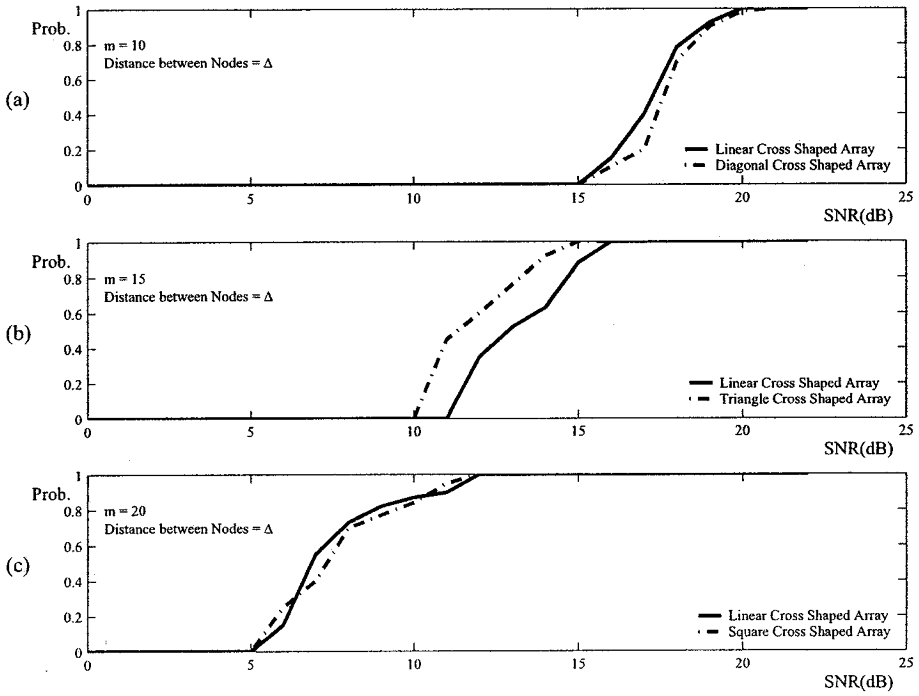

Figure 4.1: Probability of resolution (Prob. in above figures) versus the SNR for (a) $m = 10$, (b) $m = 15$ and (c) $m = 20$. The distance among the nodes is equal to one half-wavelength.

shaped geometries. It is also seen that the resolving threshold for the case of $m = 10$, using 10 half-wavelength distance between two nodes, is lower than the case of $m = 20$ with half-wavelength distance among the nodes.

To demonstrate the capability of the WSF algorithm in resolving the closely spaced sources the third experiment is conducted. For this example the three source signals are partially coherent and for each simulation their locations are chosen according to Table 3.2. Two cross shaped arrays composed of $m = 10$ elements (5 elements for each node) is used and the array of sensors are exposed to the three narrowband planar wavefronts arriving from 20, 25 and 30 degrees. The number of snapshots and the distance between the two nodes are 100 and 10 half-wavelength, respectively. The simulation results show

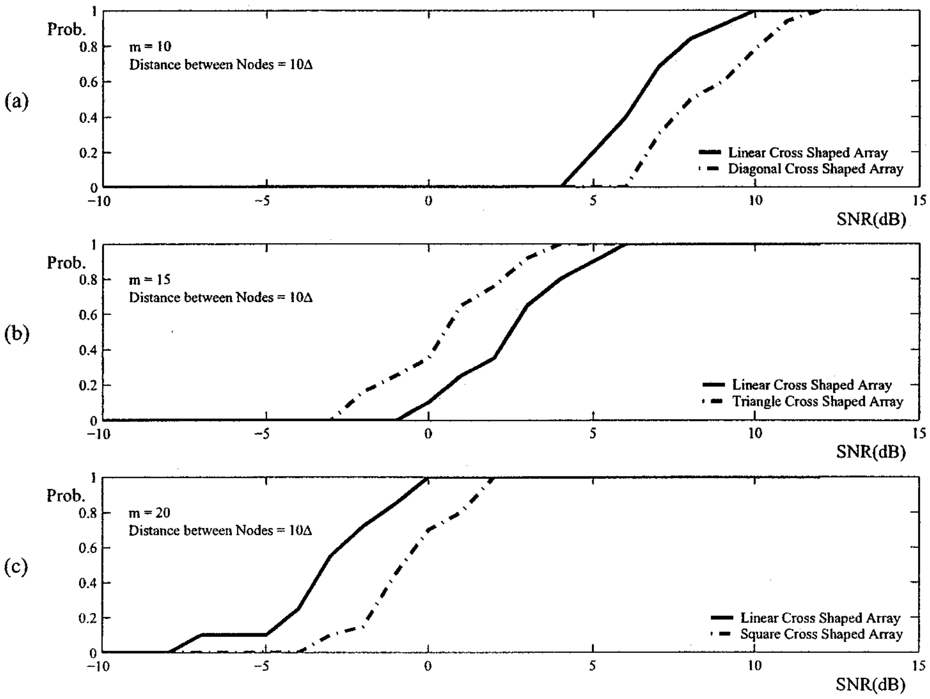

Figure 4.2: Probability of resolution (Prob. in above figures) versus the SNR for (a) $m = 10$, (b) $m = 15$ and (c) $m = 20$. The distance among the nodes is equal to 10 half-wavelength.

that the resolution capability of the DOA estimator improves by increasing the angle among the sources which is what one intuitively expects. Indeed, the threshold SNR is higher for locating the closely spaced sources. As seen in Fig. 4.3, the SNR threshold is decreased by increasing the angle among the sources.

In the last example in the present section the effects of changing the distance between the two nodes for resolving the sources using the WSF algorithm are illustrated. In this experiment the number of snapshots is taken as $N = 100$ and the location of the sources are at 20, 25 and 30 degrees. The simulation results show that by increasing the distance between the two nodes from Δ to 10Δ, the capability of estimator is improved for resolving the sources, i.e. by increasing the distance between the two nodes the SNR threshold has

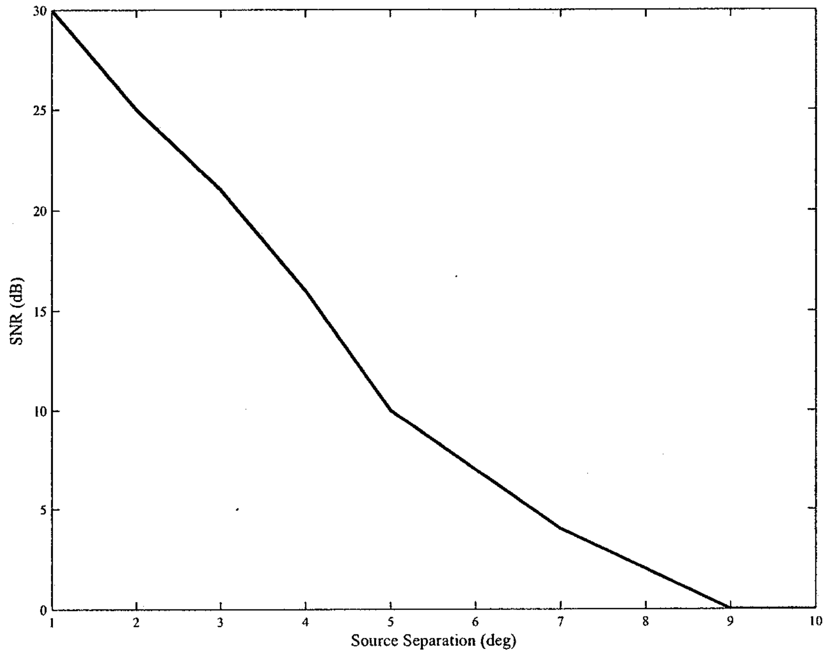

Figure 4.3: The minimum SNR required for the source separation using the WSF estimator. The location of the sources are shown in Table 3.2 and the number of sensors are $m = 10$.

decreased (refer to Fig. 4.4a). These results are confirmed by those obtained in Fig. 4.4b where the probability of resolution has improved by increasing the distance between the two nodes. However, this improvement is achieved only for a few decades of Δ (almost 30Δ) and beyond this point the capability of the DOA estimator in resolving the sources has again decreased.

To confirm these results another set of simulation results are performed. For this purpose, the norm of the bias vector is measured versus the distance between the two nodes. As depicted in Fig. 4.5, the estimation errors decrease from Δ to 25Δ, remain unchanged up to 30Δ and subsequently increase so that the DOA estimator is not able in resolving the sources beyond this point.

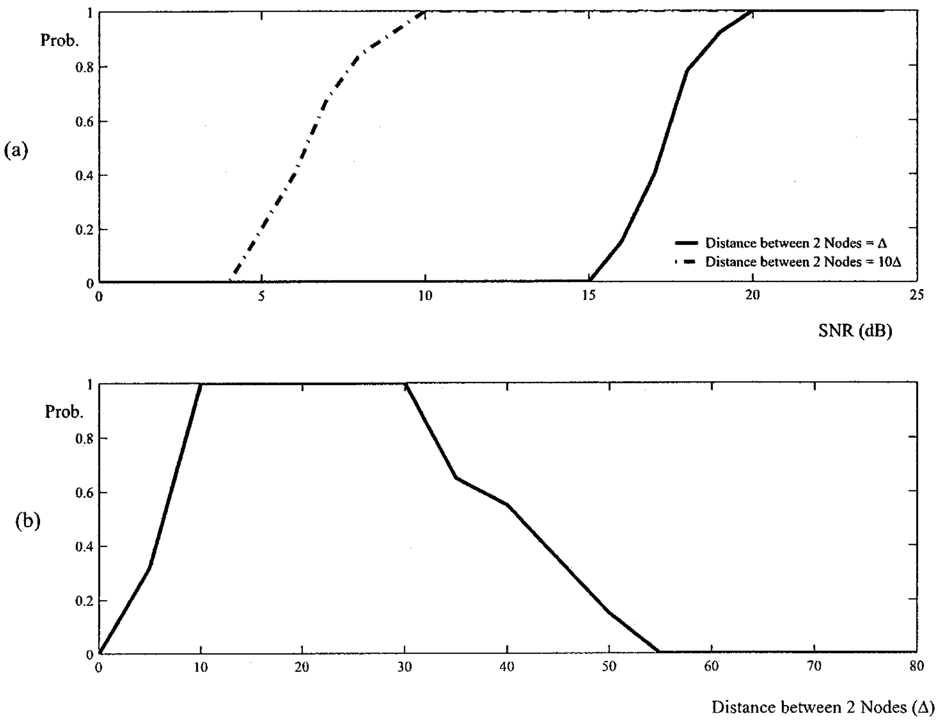

Figure 4.4: (a) Probability of resolution (Prob. in above figures) versus the SNR. The distance between the two nodes is equal to one half-wavelength and 10 half-wavelength. (b) Probability of resolution versus the distance between the two nodes ($m = 10$, $N = 100$, DOA = [20 25 30], $SNR = 10dB$).

4.4 Numerical Examples and Simulation Results for Wideband Sources

In the following section a number of numerical examples are presented to show the performance capabilities of the CSM algorithm for the array geometries discussed previously (and utilizing the WSF algorithm as a narrowband estimator). In the simulations conducted 100 independent Monte Carlo runs are performed for each example. Two bandpass coherent sources incident on an array of sensors composed of two, three or four nodes are considered. Two incident plane waves are taken to have bearing angles at 45 and 50 degrees (unless otherwise explicitly stated) where each wideband signal is the sum of a set

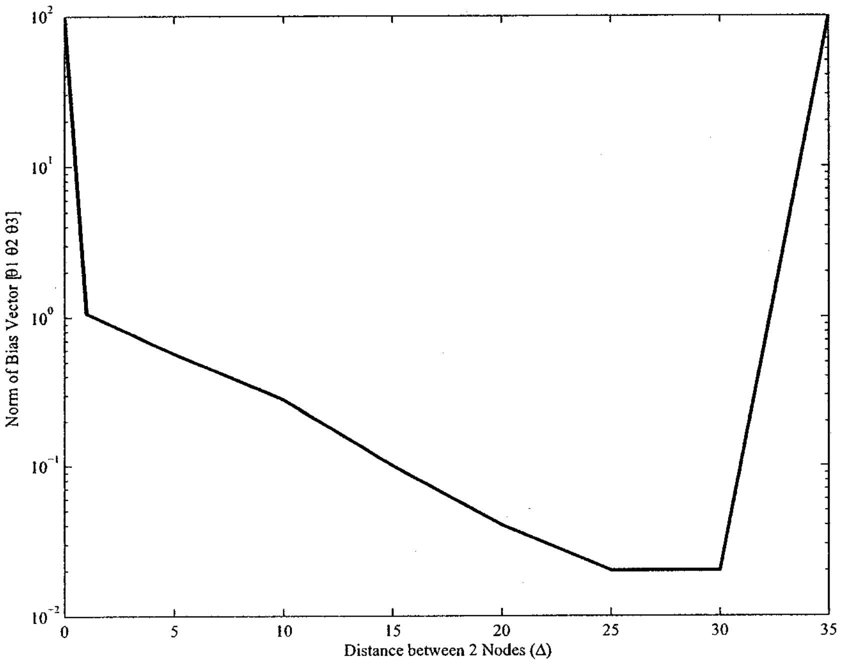

Figure 4.5: The norm of the bias vector versus the distance between the two nodes for the WSF estimator ($m = 10$, $N = 100$, $SNR = 20dB$, DOA = [20 25 30]).

of cosine signals with random amplitude, the same center frequency $f_c = 100Hz$ and the same bandwidth $BW = 40Hz$. The array noise $n(t)$ is taken as a complex valued additive bandpass (the same passband as the signals) white Gaussian process whose components are statistically independent of the source signals. The array signal model (2.3.2) is then employed to generate data to be used in forming the array covariance matrix (2.3.19). The sensor signals are observed over a $T = 48sec$ interval. These signals are then sampled at the rate of 80 samples/sec to give a total of $L = 3840$ samples for each array sensor. To approximate the underlying array covariance matrix, each data length is decomposed into $Q = 60$ non-overlapping segments each consisting of 64 samples, i.e., each segment $\Delta T = \frac{T}{Q} = 0.8sec$. Using the relationship (2.3.19), an estimate of the array covariance matrix is made with $J = 33$ equal frequency intervals spaced across the passband. Therefore, the data (signal plus noise) consists of 60 snapshots for each of the 33 narrowband frequency components.

4.4.1 Performance Capabilities of the CSM Algorithm

This experiment is conducted to study the performance of the CSM algorithm (using the WSF algorithm as a narrowband estimator) in response to changes in the number of sensors using different geometries and in the presence of wideband coherent sources. The location of sources are 45 and 50 degrees and the number of sensors are varied from $m = 10$ to $m = 20$. The geometries of the array sensors are shown in Fig. 3.2 where the distance among the nodes is chosen to be half-wavelength. The results of the simulations for 100 independent trials are depicted in Fig. 4.6. It is observed that by increasing the number of sensors, the probability of resolution improves for all the geometries. As seen in Fig. 4.6, for all cases the linear cross shaped geometry has a lower resolving threshold than the diagonal, triangular and square cross shaped geometries.

To show the effects of increasing the distance among the nodes, the above experiment is repeated where the distance between the two nodes is selected to be 10 half-wavelength. Fig. 4.7 shows that the resolving threshold is significantly improved by increasing the distance among the nodes for different geometries. Again, for all the cases the linear cross shaped geometry has a better resolving threshold than the diagonal, triangular and square cross shaped geometries. It is also seen that the resolving threshold for the case of $m = 10$ with 10 half-wavelength distance between the two nodes, is almost equal to the case of $m = 20$ with half-wavelength distance among the nodes. This example demonstrates

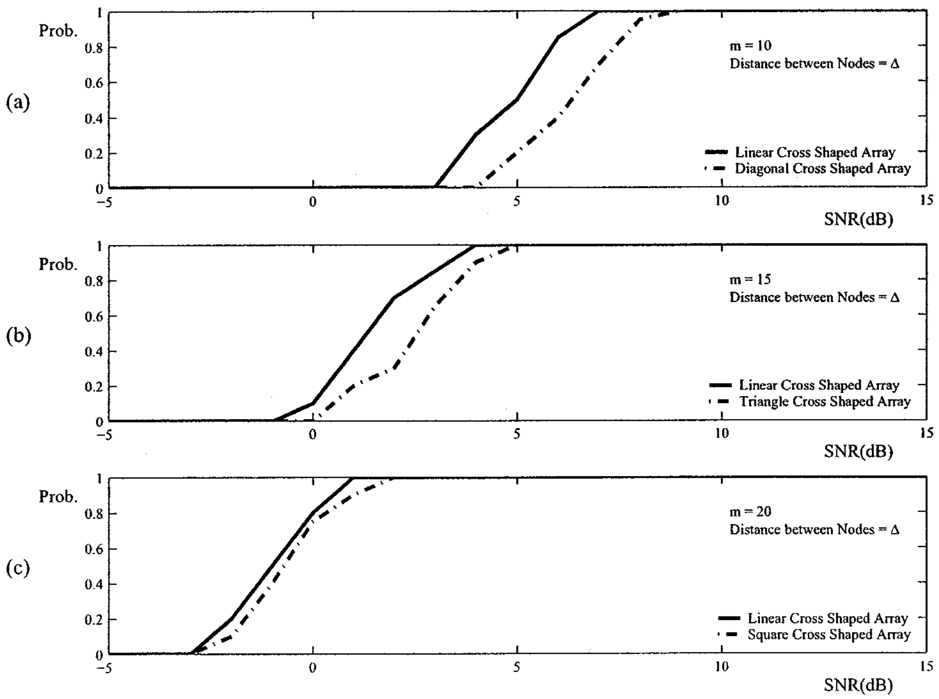

Figure 4.6: Resolution probability (Prob. in above figures) of the CSM algorithm (using the WSF algorithm as a narrowband estimator) versus the SNR for (a) $m = 10$, (b) $m = 15$ and (c) $m = 20$. The distance among the nodes is equal to one half-wavelength.

that a larger array aperture causes a lower resolving threshold and produces a more accurate DOA estimate but can result in a more challenging initialization step for the search methods. Therefore, necessitating the use of the the alternating projection (AP) algorithm for more than one time. It is also seen that the number of initial conditions leading to the global minimum is also reduced by increasing the number of sensors m (refer to Fig. 4.8).

To demonstrate the capability of the CSM method (using the WSF algorithm as a narrowband estimator) in resolving the closely spaced sources the experiment below is carried out. The simulation results show that the resolution capability of the DOA estimator improves by increasing the angle among the sources which is what one would

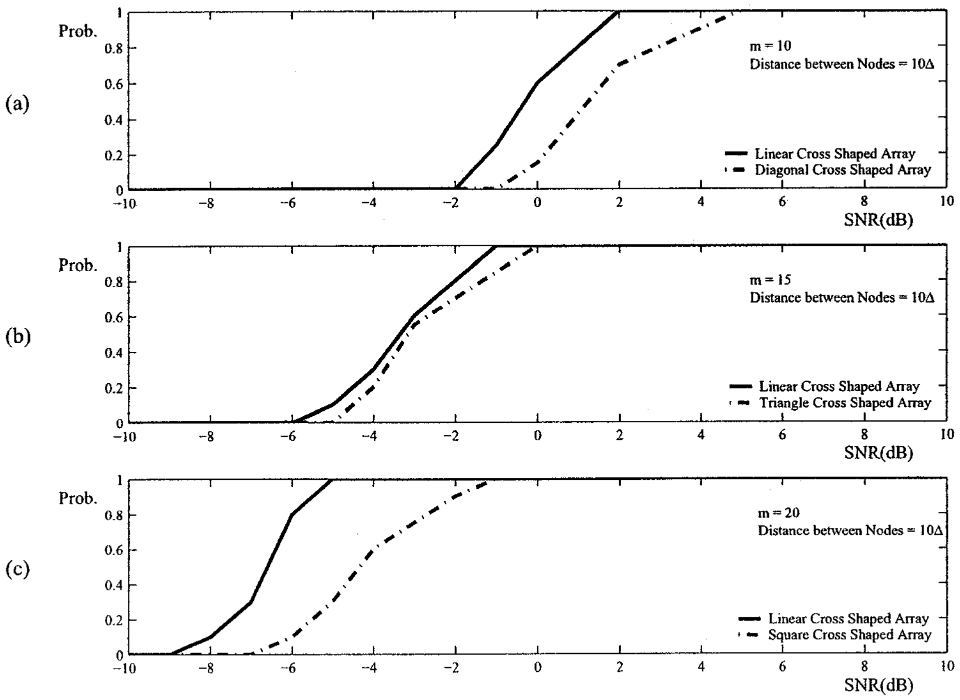

Figure 4.7: Resolution probability (Prob. in above figures) of the CSM algorithm (using the WSF algorithm as a narrowband estimator) versus the SNR for (a) $m = 10$, (b) $m = 15$ and (c) $m = 20$. The distance among the nodes is equal to 10 half-wavelength.

intuitively expect. Indeed, the threshold SNR is higher for locating the closely spaced sources as shown in Fig. 4.9. For this example the two source signals are coherent and for each simulation their locations are chosen according to Table 3.3. The geometry of array sensors is the linear cross shaped with $m = 10$ where the distance between the two nodes is chosen to be 10 half-wavelength.

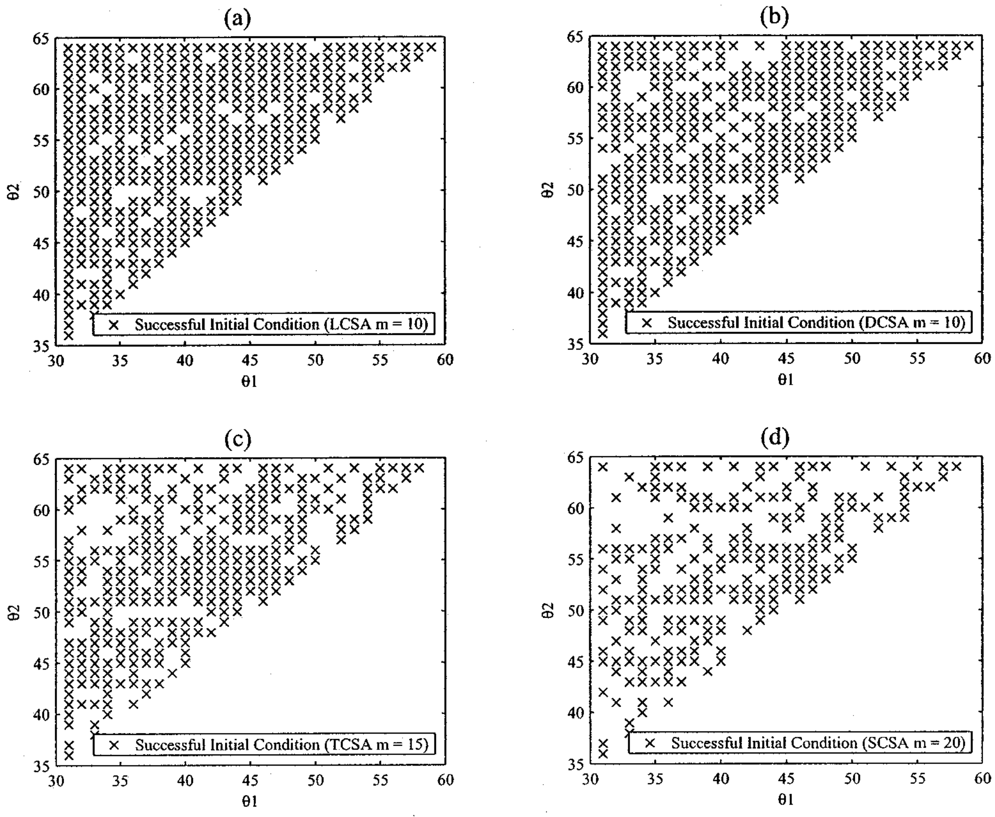

Figure 4.8: Initial conditions that lead to the global minimum using WSF algorithm for (a) Linear cross shaped array (LCSA $m = 10$), (b) Diagonal cross shaped array (DCSA $m = 10$), (c) Triangular cross shaped array (TCSA $m = 15$), and d) Square cross shaped array (SCSA $m = 20$). The distance among the nodes is equal to one half-wavelength.

4.4.2 Performance Comparison of the CSM Algorithm using the Diagonal and the Unitary Focusing Transformation Matrices

The last example in this chapter is performed to compare the performance capabilities of the CSM algorithm using the diagonal focusing transformation matrix and the unitary focusing transformation matrix. As mentioned in Chapter 2, for the CSM algorithm the best performance is obtained if the mapping of the subspaces is performed through a unitary transformation. In fact, using the unitary focusing transformation matrix to

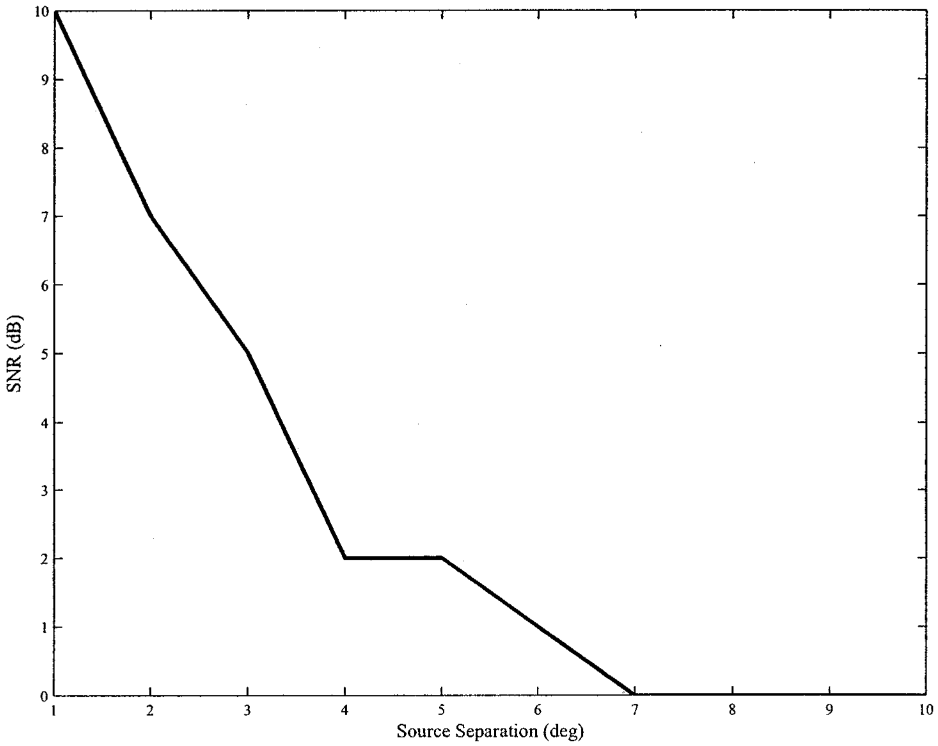

Figure 4.9: The minimum SNR required for the source separation in the CSM algorithm using the WSF algorithm as a narrowband estimator. The location of the sources are shown in Table 3.3.

align the steering matrices results in minimizing the bias of the DOA estimates. In this experiment the location of sources are 45 and 50 degrees and the geometry of array sensors is the linear cross shaped with $m = 10$ where the distance between the two nodes is chosen to be 10 half-wavelength. Fig. 4.10 depicts the norm of bias vector as a function of SNR for both the diagonal and the unitary focusing transformation matrices. As can be observed from this figure the estimator error using the unitary focusing transformation matrix is lower than the diagonal case. Unfortunately, in spite of the fact that the CSM is very effective in wideband signal processing, it suffers from an asymptotic bias as a result of errors in estimated focusing subspaces. The bias increases with the bandwidth of the sources and the deviation of the focusing subspaces from the true subspaces.

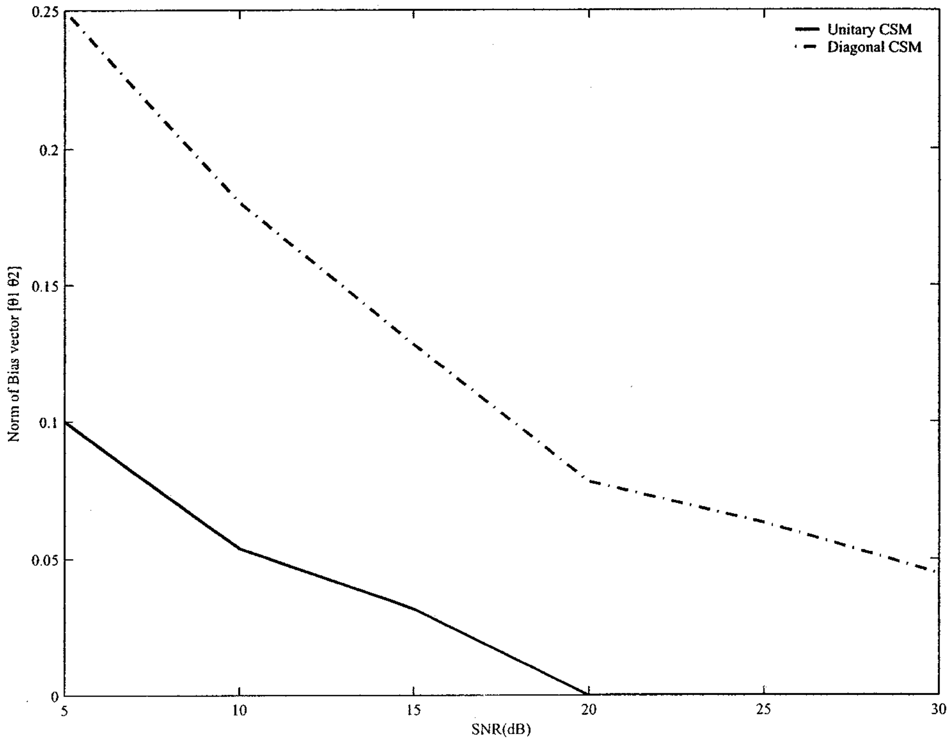

Figure 4.10: Performance of CSM algorithm using diagonal and unitary focusing transformation matrices in the presence of two wideband coherent sources ($m = 10$, $SNR = 10dB$, DOA = [45 50], Distance between nodes = 10Δ).

4.5 Conclusion

The performance capabilities of the WSF estimator using the four types of array geometries are investigated in this chapter for both the narrowband and the wideband sources. The main interest in the simulation results is to study the performance of the estimator by changing the node topology and the aperture of the array geometry. Similar to the MUSIC estimator, it is observed that by increasing the number of sensors and the distance among the nodes, the probability of resolution improves and the bias of estimator decreases for all types of geometries. Although, a larger array aperture yields a lower resolving threshold and produces a more accurate DOA estimate but it can also result in more difficulty with the initialization stage of the search methods for the WSF estimator. Therefore, the alternating projection (AP) algorithm has to be utilized for more than one time and in some situations the global convergence can not still be guaranteed. It should be noted that the iterations required in the AP algorithm increase the computational cost of the DOA estimation schemes. Finally, the performance capabilities of the CSM algorithm using both the diagonal focusing transformation matrix and the unitary focusing transformation matrix is compared. It is concluded that the estimator error using the unitary focusing transformation matrix is lower than that of the diagonal case.

Chapter 5

Performance Comparison of Wideband Techniques using the MUSIC and the WSF DOA Estimators

5.1 Introduction

Thus far in the thesis the MUSIC and the WSF estimators were discussed and using the introduced array geometries a number of numerical simulation examples showed the advantages and disadvantages of each estimator separately. This chapter attempts to compare the capabilities of the WSF and the MUSIC estimators in resolving closely spaced sources in the presence of coherent signals for both the narrowband and the wideband sources using various array geometries. As demonstrated subsequently the WSF algorithm has excellent performance in most of the situations as compared to the MUSIC algorithm but, as seen in the following examples, using a larger array aperture causes more difficulty in selecting the initialization parameters of the search methods for the WSF estimator so that AP algorithm has to be performed more than once and this iterative process increases the computational cost, and in some situations the global convergence can not still be guaranteed.

5.2 Comparison of the Results for Narrowband Case using the MUSIC and the WSF Estimators

In this section a number of numerical examples are presented to compare the performance of the MUSIC and the WSF algorithms using the previously introduced array geometries. In the simulation results 100 independent Monte Carlo runs are performed for each example and for each trial the array output is observed for $N = 100$ independent snapshots. The array of sensors are composed of two, three or four nodes and are exposed to three coherent, non-coherent and partially coherent narrowband planar wavefronts arriving from 20, 25 and 30 degrees where each narrowband signal is the sum of a set of cosine signals with random amplitude and the same center frequency $f_c = 1700Hz$. The additive noise is independent zero mean Gaussian and the SNR is defined relative to each source. Moreover, the beamforming technique (for the MUSIC algorithm) and the alternating projection (AP) algorithm (for the WSF algorithm) are used on the simulated data to form the three initial azimuth angle estimates.

In the first experiment the performance of the MUSIC and the WSF algorithms in the presence of coherent, non-coherent and partially coherent sources is compared. The results of the simulations for 100 independent trials are represented in Table 5.1. In order to find probability of resolution 100 independent trials are performed and the number of times that the method resolved the three DOAs is counted. It can be seen that the WSF estimator could resolve 3 sources even in the presence of completely coherent signals while the MUSIC estimator fails to resolve coherent sources. In other words, for non-coherent and partially coherent signals, the MUSIC algorithm has a good performance but for the coherent signals the efficiency is very low even in high SNR values. It should be noted

SNR (dB)	Probability of Resolution							
	3 non-coherent sources (source covariance matrix is diagonal)		3 partially coherent sources (source covariance matrix is non-diagonal and non-singular)		2 coherent and 1 non-coherent sources (source covariance matrix is singular)		3 coherent sources (source covariance matrix is singular)	
	MUSIC	WSF	MUSIC	WSF	MUSIC	WSF	MUSIC	WSF
0	0.00	0.00	0.00	0.00	could not resolve sources even for higher values of SNR	0.00	could not resolve sources even for higher values of SNR	0.00
5	0.00	0.55	0.00	0.25		0.10		0.00
10	0.73	1.00	0.00	1.00		0.42		0.00
15	0.95	1.00	0.65	1.00		1.00		0.25
20	1.00	1.00	1.00	1.00		1.00		0.65
25	1.00	1.00	1.00	1.00		1.00		1.00

Table 5.1: Performance comparison of the MUSIC and the WSF estimators in the presence of the coherent, non-coherent and partially coherent sources.

that in this example two cross shaped arrays composed of $m = 10$ elements (5 elements for each node) with one half-wavelength element spacing is used and the array of sensors is exposed to the three narrowband planar wavefronts arriving from 20, 25 and 30 degrees.

The second experiment is conducted to compare the performance capabilities of the MUSIC and the WSF estimators as a result of changing the number of sensors for different geometries and in the presence of partially coherent signals. The number of snapshots is $N = 100$ and the location of sources are 20, 25 and 30 degrees with the number of sensors varied from $m = 10$ to $m = 20$. The geometries of the array sensors are shown in Fig. 3.2 where the distance between the nodes is chosen to be 10 half-wavelength. The results of the simulations for 100 independent trials are depicted in Fig. 5.1. It can be observed that by increasing the number of sensors, the probability of resolution improves for both estimators and all the geometries. However, for all the cases the WSF estimator has a lower resolving threshold. It is also seen that the resolving threshold for the case of $m = 15$ using the WSF estimator is lower than the case of $m = 20$ with the MUSIC estimator.

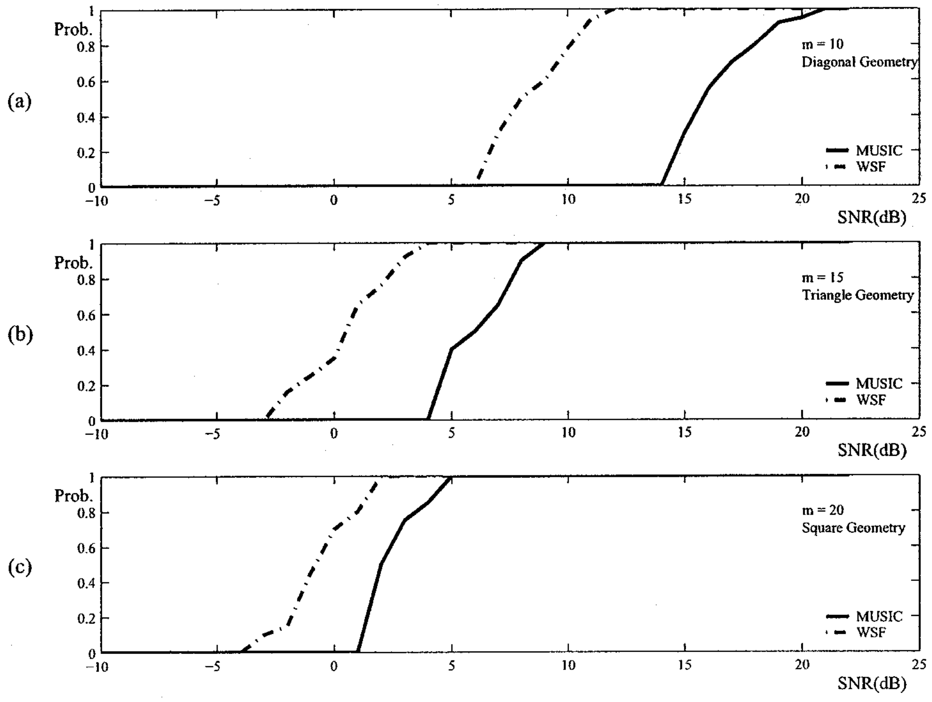

Figure 5.1: Probability of resolution (Prob. in above figures) versus the SNR for the MUSIC and the WSF estimators (a) $m = 10$, (b) $m = 15$ and (c) $m = 20$. The distance between nodes is equal to 10 half-wavelength.

To demonstrate the capabilities of the two estimators in resolving the closely spaced sources this example is designed. The simulation results show that the resolution capabilities of the estimators improve by increasing the angle among the sources which is what one intuitively expect. Indeed, the threshold SNR is higher for locating the closely spaced sources. As seen in Fig. 5.2, the SNR threshold for the WSF estimator is lower than that of the MUSIC estimator. For this experiment the three source signals are partially coherent and for each simulation their locations are chosen according to Table 3.2. Two cross shaped arrays composed of $m = 10$ elements (5 elements for each node) is used and the array of sensors are exposed to the three narrowband planar wavefronts arriving from 20, 25 and 30 degrees. The number of snapshots and the distance between the two nodes

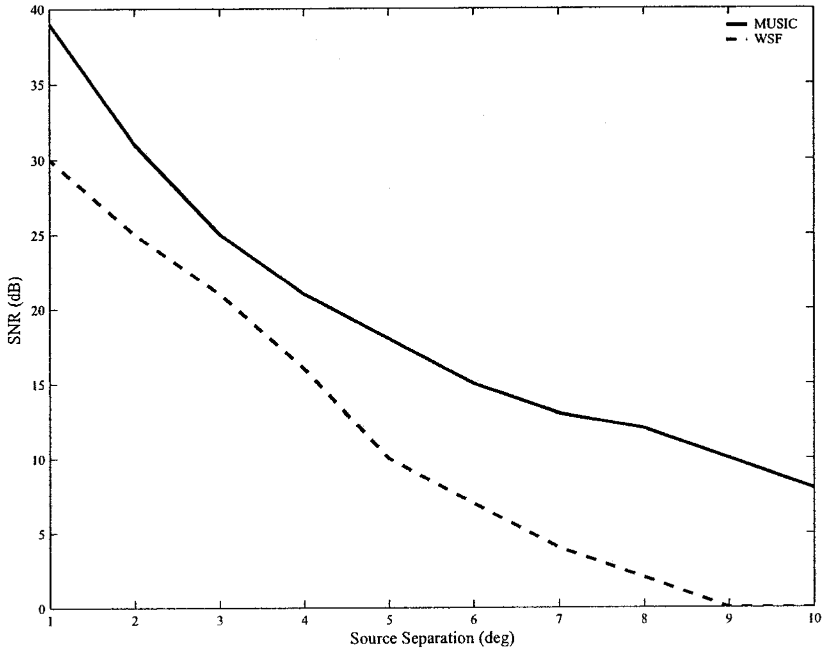

Figure 5.2: The minimum SNR required for the source separation using the MUSIC and the WSF estimators. The location of the sources are shown in Table 3.2 and the number of sensors are $m = 10$.

are 100 and 10 half-wavelength, respectively.

The last experiment in this section is performed to show the effects of changing the distance between the two nodes in the array sensors for resolving the sources for the MUSIC and the WSF estimators. In this example the number of snapshots is taken as $N = 100$ and the location of the sources are at 20, 25 and 30 degrees. The simulation results show that by increasing the distance between the two nodes from Δ to 10Δ, the capability of both estimators improves for resolving the sources, i.e. by increasing the distance between the two nodes the SNR threshold decreases (refer to Fig. 5.3a and Fig. 5.3b). These results are confirmed by those obtained in Fig. 5.3c where the probability of resolution improves by increasing the distance between the two nodes. However, this improvement can be sustained for only a few decades of Δ (almost 50Δ for the MUSIC estimator and 30Δ for the WSF estimator) and beyond that the capability of resolving the sources again decreases. Overall, the performance of the WSF estimator is again better than that of the MUSIC estimator.

To confirm the above results, another simulation result is conducted. For this purpose, the norm of the bias vector is measured versus the distance between the two nodes. As depicted in Fig. 5.4, the estimation errors for the WSF decrease from Δ to 25Δ, remain unchanged up to 30Δ and then increase, so that the estimator is not able to resolve the sources. Similar results are obtained for the MUSIC estimator where the range of performance is longer than that of the WSF. Decreasing the estimation errors starts from Δ to 40Δ, remains constant up to 65Δ and then again increases beyond this point.

5.3 Comparison of Results for the CSM Method using the MUSIC and the WSF estimators in Wideband Case

In the following simulation results a number of numerical examples are presented to compare the performance of the MUSIC and the WSF algorithms as narrowband estimators used in the CSM algorithm for the various array geometries considered previously. The scenario used here is similar to that defined in section 3.5.

The first example is carried out to compare the performance of the CSM algorithm (using the MUSIC and the WSF algorithms as narrowband estimators) in response to changing the number of sensors for different geometries in the presence of wideband coherent sources. The location of sources are 45 and 50 degrees and the number of sensors are varied from $m = 10$ to $m = 20$. The geometries of the array sensors are shown in Fig. 3.2 where the distance among the nodes is chosen to be 10 half-wavelength. The

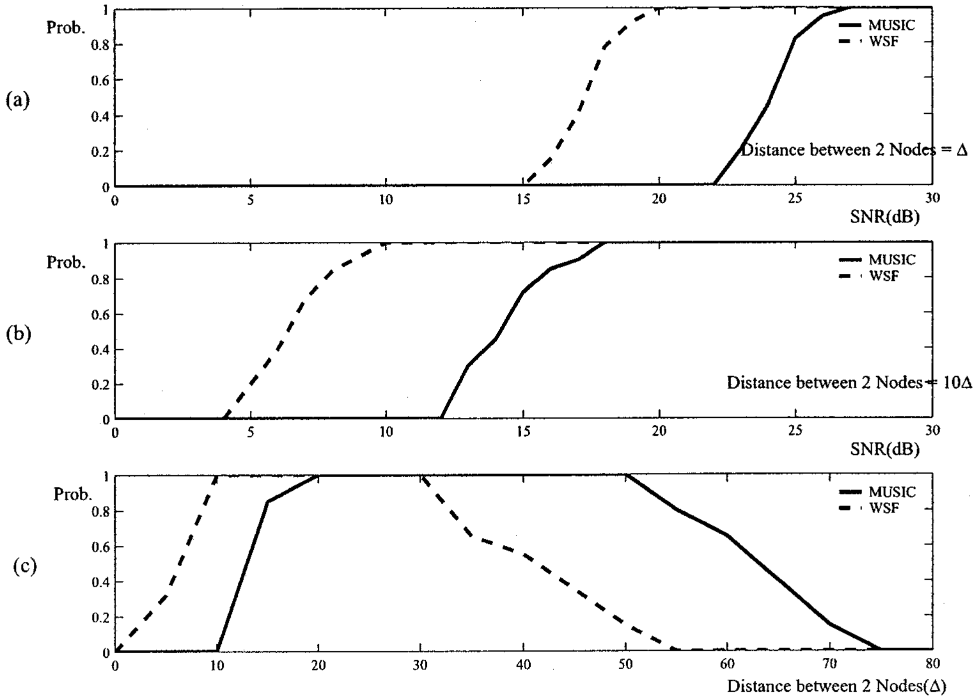

Figure 5.3: Probability of resolution (Prob. in above figures) versus the SNR for (a) Distance between the two nodes = Δ, (b) Distance between the two nodes = 10Δ (c) Probability of resolution versus the distance between the two nodes ($m = 10$, $N = 100$, DOA = [20 25 30], $SNR = 10dB$).

results of the simulations for 100 independent trials are depicted in Fig. 5.5 where the geometry of sensors is selected to be linear composed of 2, 3 and 4 nodes. It is observed that by increasing the number of sensors, the probability of resolution improves for all the geometries. As seen in this figure, for all the cases the WSF algorithm has a lower resolving threshold. To show the effects of changing the geometries of the sensors, this experiment is repeated by using diagonal cross shaped geometry ($m = 10$), triangular cross shaped geometry ($m = 15$) and square cross shaped geometry ($m = 20$). Again, as seen in Fig. 5.6, the WSF estimator has a better resolving threshold as compared to the MUSIC algorithm and the probability of resolution improves by increasing the number of sensors for all the geometries. It should be noted that the difference in resolving threshold

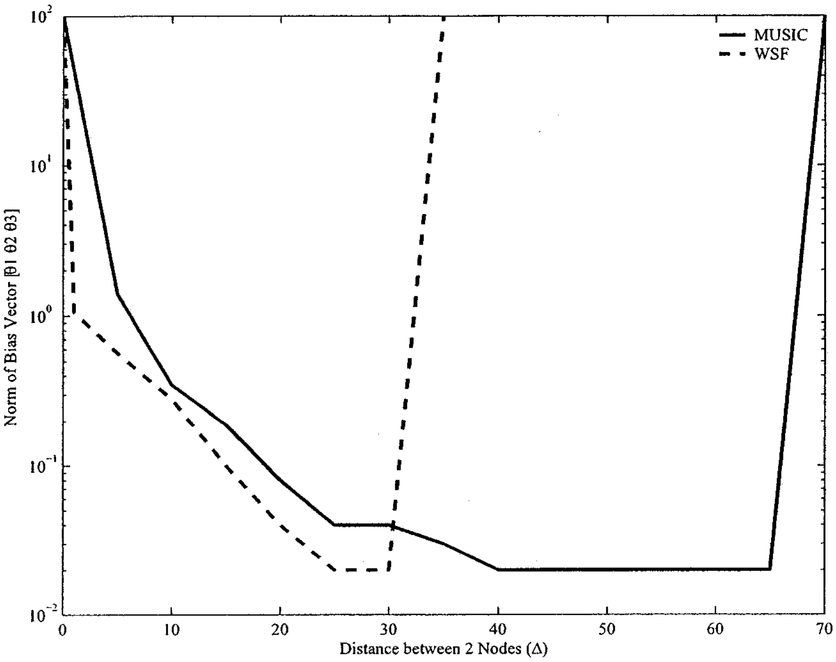

Figure 5.4: The norm of the bias vector versus the distance between the two nodes for the MUSIC and the WSF estimator ($m = 10$, $N = 100$, $SNR = 20dB$, DOA = [20 25 30]).

is more significant in the case of linear geometry ($m = 20$) than the square geometry. It is also seen that the resolving threshold for the case of $m = 15$ (linear geometry) using the WSF estimator is lower than the case of $m = 20$ with the MUSIC estimator.

This experiment does demonstrate that a larger array aperture yields a lower resolving threshold and produces a more accurate DOA estimates but it could also result in ambiguous estimates of the DOAs (refer to Fig. 3.12) for the MUSIC algorithm and more difficulty with the initialization step of the search methods for the WSF estimator.

The second experiment is performed to compare the capabilities of the MUSIC and the WSF algorithms as narrowband estimators used in the CSM scheme for resolving the closely spaced sources. The simulation results show that the resolution capabilities of both estimators improve by increasing the angles among the sources which is what one

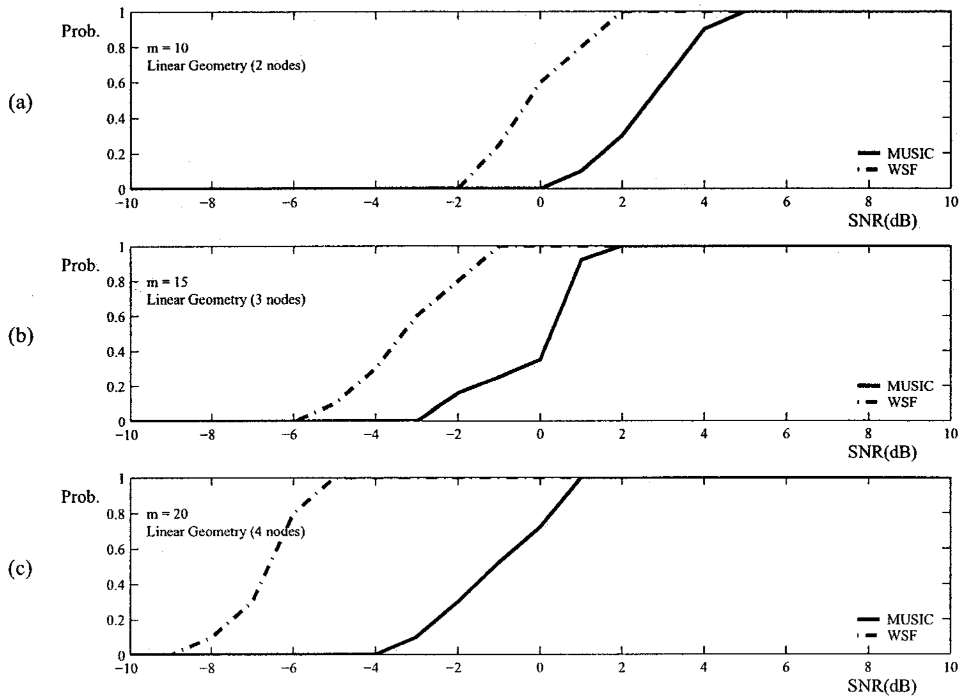

Figure 5.5: Resolution probability (Prob. in above figures) of the CSM algorithm (using the MUSIC and the WSF algorithms as narrowband estimators) versus the SNR for (a) $m = 10$, (b) $m = 15$ and (c) $m = 20$. The geometry of sensors is the linear cross shaped and the distance among the nodes is equal to 10 half-wavelength.

would intuitively expect. Indeed, the threshold SNR is higher for locating the closely spaced sources. Furthermore, as depicted in Fig. 5.7, the SNR threshold of the WSF for locating the sources is lower than that of the MUSIC algorithm. For this example the two source signals are coherent and for each simulation their locations are chosen according to Table 3.3. The geometry of array sensors is the linear cross shaped with $m = 10$ where the distance between the two cross shaped nodes is 10 half-wavelength.

The last experiment is conducted to compare the performance capabilities of using the diagonal focusing transformation matrix and the unitary focusing transformation matrix in the CSM algorithm (using the MUSIC and the WSF algorithms as narrowband estimators). As indicated in Chapter 2, for the CSM algorithm the best performance is

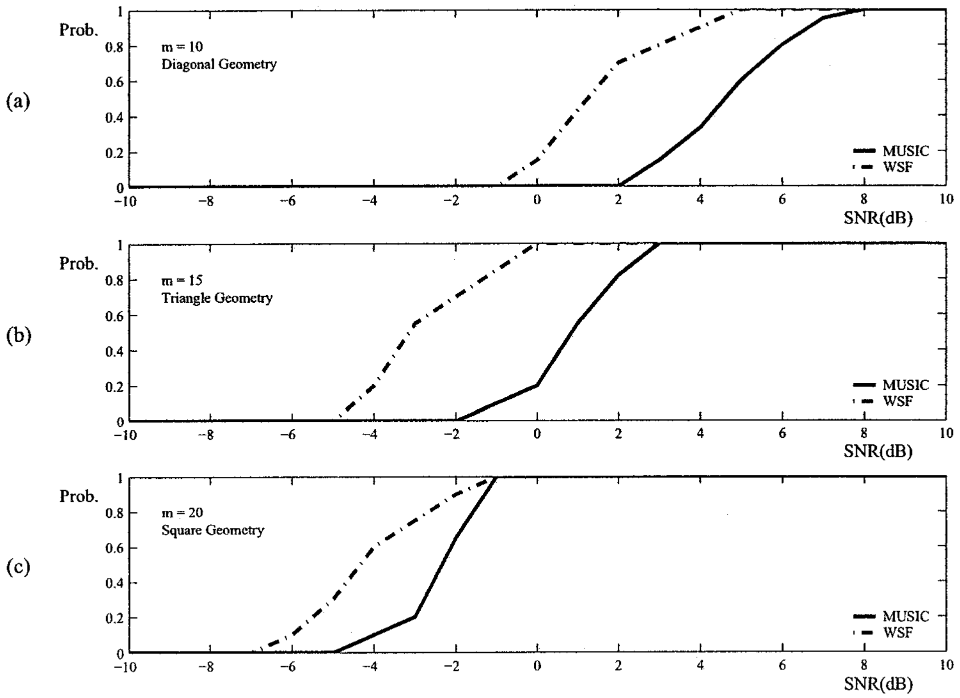

Figure 5.6: Resolution probability (Prob. in above figures) of the CSM algorithm (using the MUSIC and the WSF algorithms as narrowband estimators) versus the SNR for (a) Diagonal geometry, $m = 10$, (b) Triangular geometry, $m = 15$ and (c) Square geometry, $m = 20$. The distance among the nodes is equal to 10 half-wavelength.

achieved if the mapping of the subspaces is performed through a unitary transformation. In fact, using the unitary focusing transformation matrix to align the steering matrices can ensure minimization of the DOA estimate bias. To investigate this error, the norm of the bias vector as a function of the SNR for both the diagonal and the unitary focusing transformation matrices and for both the MUSIC and the WSF estimators are calculated and the results are shown in Fig. 5.8. As can be observed from this figure the estimator error using the unitary focusing transformation matrix is lower than that of the diagonal case and also in both cases the WSF estimator has a lower bias than that of the MUSIC algorithm.

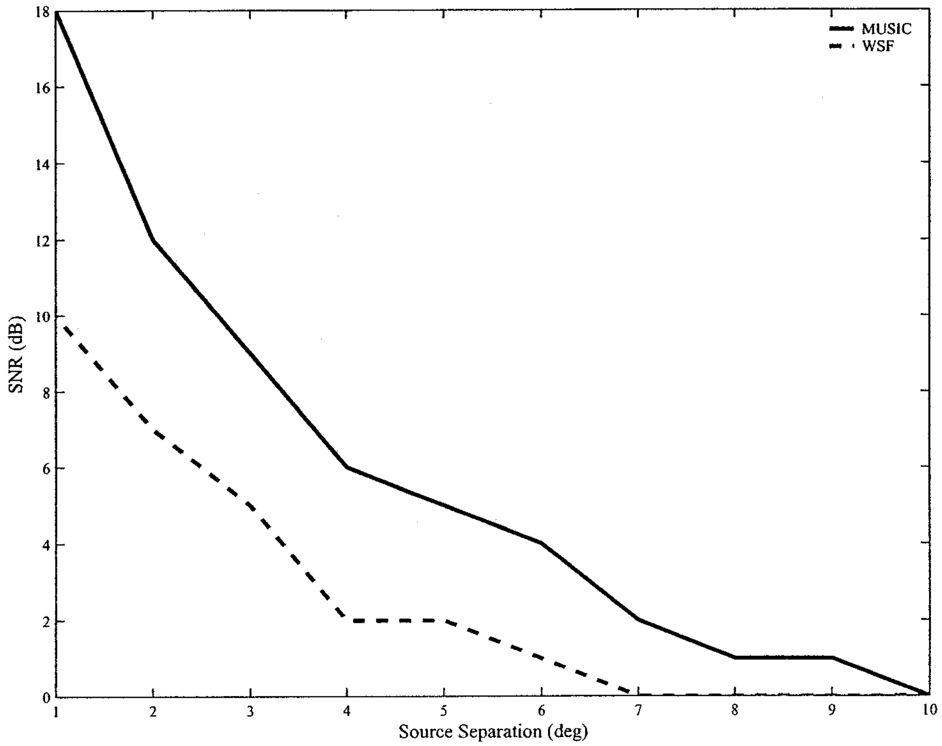

Figure 5.7: The minimum SNR required for the source separation in the CSM algorithm using the MUSIC and the WSF algorithms as narrowband estimators. The location of the sources are shown in Table 3.3 and the distance between the two cross shaped nodes is 10 half-wavelength.

5.4 Conclusion

The performance of the MUSIC and WSF estimators for both the narrowband and wideband sources using the four types of array geometries are compared. The main goal of this chapter was to compare the performance capabilities of the DOA estimators by changing the number of sensors, the node topology and the aperture of array geometry. As observed, the WSF algorithm had an excellent performance in most of the scenarios considered as compared to the MUSIC algorithm. It was concluded that the WSF estimator could resolve sources even in the presence of completely coherent signals while the MUSIC estimator fails to resolve coherent sources.

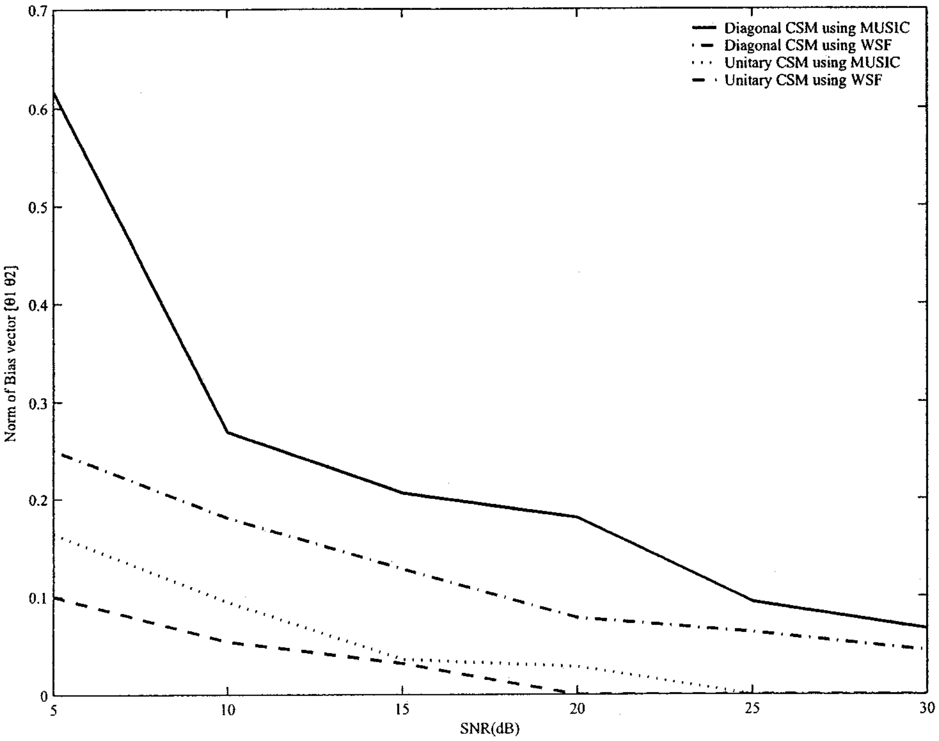

Figure 5.8: Performance of the CSM algorithm using the diagonal and the unitary focusing transformation matrices in the presence of two wideband coherent sources. The norm of the bias vector versus the SNR using the MUSIC and the WSF estimator ($m = 10$, $SNR = 10dB$, DOA = [45 50] and the distance between the two nodes = 10Δ).

It was also observed that by increasing the number of sensors and the distance among the nodes the probability of resolution has improved and the estimator bias decreases for both estimators and all the geometries. However, for all the cases considered the WSF estimator had a lower resolving threshold and a lower error. The simulation results demonstrated that in some situations the resolving threshold for the WSF estimator with fewer number of nodes was lower than the MUSIC estimator with more number of nodes. It should be noted that the improvement in resolving the threshold and the bias of estimators (as a result of increasing the distance among the nodes) extended only for a few decades of Δ such that the MUSIC estimator had a wider range of performance as compared to the WSF estimator. Although, the simulation results showed that a larger array aperture results in a lower resolving threshold and produces more accurate DOA estimates but it could also lead to the ambiguity in the DOA estimates for the MUSIC algorithm and more difficulty with initialization stage of the search methods for the WSF estimator. The resolution capabilities of both estimators were compared and it was observed that this criterion improved by increasing the angle among the sources. Indeed, the threshold SNR was higher for locating the closely spaced sources and as demonstrated the SNR threshold for the WSF estimator was lower than that of the MUSIC estimator. Finally, the performance results of the CSM algorithm using the diagonal focusing transformation matrix and the unitary focusing transformation matrix were considered. As was shown the estimator error using the unitary focusing transformation matrix was lower than that of the diagonal case, and also in both cases the WSF estimator had a lower bias than that of the MUSIC algorithm.

Chapter 6

Conclusion and Future Research Directions

6.1 Summary and Conclusion

In this thesis the fundamentals issues and problems for both the narrowband and the wideband array signal processing techniques were considered. For the narrowband case, the multiple signal classification (MUSIC) and the weighted subspace fitting (WSF) characterized by the eigen-decomposition of the covariance matrix were studied. For the challenging wideband scenario the incoherent signal subspace method (ISM) and the coherent signal subspace method (CSM) were considered. Extensions of the narrowband and the wideband methods to various specific sensor geometries known as linear, diagonal, triangular and square cross shaped array geometries were performed in Chapters 3 and 4. Use of the WSF algorithm in place of the MUSIC method in the CSM as a wideband technique was also investigated in Chapter 4. Finally, performance comparison of the narrowband and the wideband techniques using these algorithms were carried out in Chapter 5.

Four different types of array geometries as stated above, namely linear cross shaped array, diagonal cross shaped array, triangular cross shaped array and square cross shaped array were considered. As demonstrated in the computer simulations provided both the node topology and the aperture are important factors and the performance capabilities of both the narrowband and the wideband techniques are affected by changes in these parameters. The performance results of the MUSIC and the WSF estimators for both the narrowband and the wideband situations were compared and it was observed that the WSF algorithm has an excellent performance in most of the situations when compared to the MUSIC algorithm. As observed the WSF estimator could resolve sources even in the presence of completely coherent signals while the MUSIC estimator fails to resolve coherent sources.

It was also seen that by increasing the number of sensors and the distance among the nodes the performances achieved by both estimators have improved by reducing the bias and the resolution SNR thresholds for all the geometries. However, for all the cases the WSF estimator has a lower resolving threshold and a lower estimation error. According to the simulation results obtained in some situations the resolving threshold for the WSF estimator using fewer umber of nodes was lower than that of the MUSIC estimator with more number of nodes. As simulation results show the improvements in resolving the threshold and estimator bias (as a result of increasing the distance among the nodes) were sustained only for a few decades of Δ such that the MUSIC estimator had a wider range of performance as compared to the WSF estimator. Moreover, the resolution capability of both estimators was compared and as demonstrated this criterion improved by increasing the angle among the sources. In fact, the threshold SNR was higher for locating the closely spaced sources, and as shown, the SNR threshold for the WSF estimator was lower than that of the MUSIC estimator.

Although, the simulation results show that a larger array aperture can lead to lower resolving threshold and produces more accurate DOA estimates, it also results in ambiguous estimates of the DOAs for the MUSIC estimator and more difficulty in initialization of the search methods for the WSF estimator, whereas the AP algorithm needs to be performed more than once.

The subspace fitting error criterion was used in the CSM algorithm for selection of the optimum focusing frequency. Using this optimum focusing frequency it was observed that the bias of the estimator and the resolution threshold of the SNR were reduced.

Finally, the performance capabilities of the CSM algorithm using the diagonal focusing transformation matrix and the unitary focusing transformation matrix was also considered. As demonstrated the estimator error of estimator using the unitary focusing transformation matrix was lower than that of the diagonal case and also in both cases the WSF estimator had a lower bias than that of the MUSIC algorithm.

6.2 Suggestions for Future Work

Throughout this thesis, we assumed that the sources are in the far field i.e. the incident wavefield arises from a distant source so that the incident signals have planar wave fronts. Indeed, an isotropic point source (uniform propagation in all direction) gives rise to a spherical traveling wave whose amplitude is inversely proportional to the distance to the source so that all points lying on the surface of a sphere of same radius will then share a common phase. This indicates that the distance between the sources and the sensor arrays determines whether the sphericity of the wave should be taken into account. Therefore, an extension of the work in this thesis is to investigate the near field wave case where the conditions imply that the radius of propagation is not sufficiently large compared to the physical size of the array and the assumption of planar wave with constant phase is no longer valid.

In array processing (and consequently in this thesis) it is frequently assumed that the source signals are generated by point sources. This is a modeling constraint that is not always satisfied in reality. In the literature, distributed sources are treated as a combination of a large number of closely spaced point sources. This point source approximation of the distributed source can lead to erroneous results. Thus, much future work is warranted on finding an appropriate model for distributed sources.

Recent developments in integrated circuit technology and MEMS have allowed the construction of low cost small sensor nodes where advanced signal processing tasks and functions can enable one to form complex network of wireless sensor networks. Sensor network applications are widespread with uses varying from geographical monitoring to military operations. Therefore, the scope of developing a general sensor network for arbitrary array geometries for various DOA estimation techniques with reusable arbitrary nodes in array processing is of critical importance for future research. Application of the considered array geometries in this thesis to sensor networks is warranted and much future work on processing of wideband signals for detection, localization and tracking of these sources are of significant interest.

Bibliography

[1] Ottersten, Bjorn, "Array Processing for Wireless Communications", Proceedings of the Eighth IEEE Signal Processing Work-shop on Statistical Signal and Array Processing, 1996.

[2] Harry L. and Van Trees, Optimum Array Processing, Part IV of Detection, Estimation and Modulation Theory, John & Sons. Inc, New York, 2002.

[3] R. O. Schmidt, "A Signal Subspace Approach to Multiple Emitter Location and Spectral Estimation", Ph.D. dissertation, Stanford Univ., Stanford, CA, Nov. 1981.

[4] M. Viberg, B. Ottersten. and T. Kailath, "Detection and Estimation in Sensor Arrays Using Weighted Subspace Fitting". IEEE Trans. Acoust., Speech, Signal Processing, Vol. 39, Nov. 1991.

[5] M.Wax, T.Shan and T.Kailath, "Spatio-Temporal Spectral Analysis by Eigenstructure Methods", IEEE Trans. on ASSP, Vol. 32, pp. 817-827, Aug. 1984.

[6] H.Wang and M.Kaveh, "Coherent Signal-Subspace Processing for the Detection and Estimation of Angles of Arrival of Multiple Wide-Band Sources", IEEE Trans. on ASSP, Vol. 33, No. 4, pp. 823-831, Aug. 1985.

[7] S. Valaee and P. Kabal, "A Unitary Transformation Algorithm for Wideband Array Processing", Proc. Sixth IEEE SP Workshop on Statistical Signal and Array Processing (Victoria, BC), pp. 300-303, 1992.

[8] S. Valaee and P. Kabal, "Wideband Array Processing using A Two-sided Correlation Transformation", IEEE Transactions On Signal Processing, vol. 44, pp. 160-172, Jan. 1995.

[9] J. Capon, “High-resolution Frequency-wavenumber Spectrum Analysis”, Proc. IEEE, Vol. 57, pp. 1408-1418, Aug. 1969.

[10] K.M. Buckley and L.J. Griffiths, “An Adaptive Generalized Sidelobe Canceller with Derivative Constraints”, IEEE, Trans. on Antennas and Propagation, Vol. AP-34, No. 3, pp. 3111-319, 1986.

[11] O.L. frost, “An Algorithm for Linearly Constrained Adaptive Array Processing”, Proc. of the IEEE, Vol. 60, No. 8, pp. 926-935, Aug. 1972.

[12] B.D Van Veen and K.M. Buckley, “Beamforming: A Versatile Approach to Spatial Filtering”, IEEE ASSP Magazine, pp. 4-24, Apr. 1988.

[13] .S. Haykin, editor, Array Signal Processing, Prentice-Hall, Englewood Cliffs, NJ, 1985.

[14] S. U. Pillai, Array Signal Processing. Springer-Verlag, 1989.

[15] H.Krim and J.H Cozzens, “Detection and Parameter Estimation of Correlated Signals in Noise”, Ph.D. thesis, Northeastern Univ., Jun. 1991.

[16] M. Viberg and B. Ottersten, “Sensor Array Processing Based on Subspace Fitting”, IEEE Trans. Signal Processing, Vol. 39, No. 5, pp.1110-1121, May 1991.

[17] J. A. Cadzow, “Direction of Arrival Estimation Using Signal Subspace Modeling”, IEEE Trans. on Aerospace and Electronic Systems, Vol. 28, No. 1, Jan. 1992.

[18] G. Bienvenu and L. Kopp, “Optimality of High Resolution Array Processing using the Eigensystem Approach”, IEEE Trans. Acoust., Speech, Signal Processing, Vol. 31, pp. 1235-1248, 1983.

[19] R. O. Schmidt, “Multiple Emitter Location and Signal Parameter Estimation”, IEEE Trans. on Antenna and Prop., Vol. 34, pp. 276-280, Mar. 1986.

[20] J.A. Cadzow, “A High Resolution Direction of Arrival Algorithm for Narrowband Coherent and Incoherent Sources”, IEEE Trans. Acoust., Speech, Signal Processing, Vol. ASSP-36, pp. 965-979, Jul. 1988.

[21] T.J. Shan, M.Wax, and T. Kailath, "Detection and Estimation in Sensor Arrays Using Weighted Subspace Fitting", IEEE Trans. Acoust., Speech, Signal Processing, Vol. 33, pp. 806-811, Aug. 1985.

[22] I. Ziskind and M. Wax, "Maximum Likelihood Localization of Multiple Sources by Alternating Projection", IEEE Trans. Acoust., Speech, Signal Processing, Vol. 36, pp. 1553-1560, Oct. 1988.

[23] K. Sharman, "Maximum Likelihood Estimation by Simulated Annealing", In Proc. ICASSP 88 Conf., pp. 2741-2744 New York, Apr. 1988.

[24] K. Sharman and G.D. McClurkin, "Genetic Algorithms for Maximum Likelihood Parameter Estimation", In Proc. ICASSP 89 Conf., pp. 2716-2719, Glasgow, Scotland, May 1989.

[25] M. Feder and E. Weinstein, "Parameter Estimation of Superimposed Signals Using the EM Algorithm", IEEE Trans. Acoust., Speech, Signal Processing, Vol. 36, pp. 477-489, Apr. 1988.

[26] .M.I. Miller and D.R. Fuhrmann, "Maximum-Likelihood Narrow-Band Direction Finding and the EM Algorithm", IEEE Trans. Acoust., Speech, Signal Processing, Vol. 38, No. 9, pp. 1560-1577 Sept. 1990.

[27] Y. Bresler and A. Macovski, "Exact Maximum Likelihood Parameter Estimation of Superimposed Exponential Signals in Noise", IEEE Trans. Acoust., Speech, Signal Processing, Vol. 34, pp. 1081-1089, Oct. 1986.

[28] M. Wax and T. Kailath, "Optimal Localization of Multiple Sources by Passive Arrays", IEEE Trans. Acoust., Speech, Signal Processing, Vol. 31 pp. 1210-1218, Oct. 1983.

[29] J.F. Böhme and D. Kraus, "On Least Squares Methods for Direction of Arrival Estimation in the Presence of Unknown Noise Fields", In Proc. ICASSP 88, pp. 2833-2836, New York, N.Y., 1988.

[30] D.P. Bertsekas, "Nonlinear Programming", Athena Scientific, Belmont, Massachusetts, USA, 1995.

[31] L. Kaufman, "A Variable Projection Method for Solving Separable Nonlinear Least Squares Problems", BIT, Vol. 15, pp. 49-57, 1975.

[32] A. Ruhe and P.A. Wedin, "Algorithms for Separable Nonlinear Least Squares Problems", SIAM Rev., Vol. 22, pp. 318-32 7, Jul. 1980.

[33] G. Golub and V. Pereyra, "The Differentiation of Pseudoinverses and Nonlinear Least Squares Problems Whose Variables Separate", SIAM J. Numer. Anal., Vol. 10, pp. 413-432, 1973.

[34] P.E. Gill, W. Murray and M. H. Wright, "Practical Optimization", London: Academic, 1981.

[35] J.E. Dennis and R.B. Schnabel, "Numerical Methods for Unconstrained Optimization and Nonlinear Equations", Englewood Cliffs, NJ: Prentice-Hall, 1983.

[36] G. H. Golub and C. F. van Loan, "Matrix Computations", Baltimore, MD: Johns Hopkins University Press, 1983.

[37] G. Su and M. Morf, "The Signal Subspace Approach for Multiple Wideband Emitter Location", IEEE Trans. Acoust. Speech Signal Process., vol. 31, pp. 1502-1522, Dec. 1983.

[38] H. L. Van Trees, Detection, Estimation, and Modulation Theory, PartI. New York: Wiley, 1968.

[39] S. Valaee and P. Kabal, "Optimal focusing subspace for coherent signal subspace processing", IEEE Trans. Signal Processing, Vol. 44, No. 3, pp. 752-756, Mar. 1996.

[40] H. Hung and M. Kaveh, "Focusing Matrices for Coherent Signal Subspace Processing", IEEE Trans. Acoust., Speech, Signal Processing, Vol. 36, pp. 1272-1281, August 1988.

[41] D. R. Brillinger, Time Series: Data Analysis and Theory. New York: Holt, Rinehart and Wiston, 1975.

[42] M. A. Doron and A. J. Weiss, "On Focusing Matrices for Wideband Array Processing", IEEE Trans. Signal Processing, Vol. 40, pp. 1295-1302, Jun. 1992.

[43] M. A. Doron, E. Doron and A. J. Weiss, "Coherent Wideband Processing for Arbitrary Array Geometry", IEEE Trans. Signal Processing, Vol. 41, pp. 414-417, Jan. 1993.

[44] H. S. hung and C. Y. Mao, "Robust Coherent Signal Subspace Processing for Directions of Arrival Estimation of Wideband Sources", IEE Proc. Radar, Sonar Navig., Vol. 141, No. 5, Oct. 1994

[45] G. Bienvenu, P. Fueuxer, G. Vezzosi, L. Kopp and F. Florin, "Coherent Wideband High Resolution Processing for Linear Array", Proc. ICASSP Vol. 89, pp. 2799-2802, Apr. 1989.

[46] J. Krolick and D. Swingler, "Focused Wideband Array Processing by Spatial Resampling", IEEE Trans. Acoust., Speech, Signal Processing, Vol. 38, pp. 356-360, Feb. 1990.

[47] R. A. Horn and C. A. Johnson, Matrix Analysis. Cambridge, England: Cambridge University Press, 1985.

[48] S. Valaee, B. Champagne, and P. Kabal, "Localization of Wideband Signals using Least-squares and Total Least-squares Approaches", IEEE Transactions On Signal Processing, vol. 47, pp. 1213-1222, May 1999.